Transition Metal Oxides and Their Use as Hole Extraction Materials in Organic Photovoltaic Devices

Jonathan Griffin

Department of Physics and Astronomy

University of Sheffield

Thesis submitted for the degree of Doctor of Philosophy

January 2014

Publications

J. Griffin & A. R. Buckley. Reactive sputtering: A method for controlling the stoichiometry and energy level structure of amorphous molybdenum oxide films. *MRS proceedings*. **1443** (2012)

J. Griffin, D. C. Watters, H. Yi, A. Iraqi, D. G. Lidzey & A. R. Buckley. The influence of MoOx anode stoicheometry on the performance of bulk heterojunction polymer solar cells. *Advance Energy Materials*. **3** (2013) 903-908

E. Bovill, J. Griffin, T. Wang, J. Kingsley, H.Yi, A. Iraqi, A. R. Buckley and D. G. Lidzey. Air processed organic photovoltaic devices incorporating a MoOx anode buffer layer. *App. Phys. Lett*. **102** (2013) 183303

J. Griffin, A. J. Pearson, N. W. Scarratt, T. Wang, D. G. Lidzey & A. R. Buckley. Towards low temperature spray coating of polymer organic solar cells. *Under Review*

Conference Presentations

UK organic electronics. Oxford 2010. **Poster**. *Using ultraviolet photoelectron spectroscopy to study energy level alignment at interfaces.*

UK Society for information displays. Imperial college London 2011. **Poster**. *A method for varying the stoichiometry of molybdenum oxide films and its effect on charge injection properties into hole transporting polymers TFB, PFB and P3HT.*

Materials research society spring conference. San Francisco 2012. **Poster**. *Charge injection/extraction at the interface between molybdenum oxide and organic polymers in OLED's and OPV's.*

Materials research society spring conference. San Francisco 2012. **Oral**. *Reactive sputtering: A method of controlling the stoichiometry and energy level structure of amorphous Molybdenum oxide films.*

UK semiconductors. Sheffield 2012. **Poster**. *Charge injection/extraction at the interface between molybdenum oxide and organic polymers in OLED's and OPV's.*

Sheffield polymer physics. Sheffield 2012. **Poster**. *Solution processed metal oxides for large area production of organic photovoltaics.*

European optical societies annual meeting. Aberdeen 2012. **Oral**. *Surveying metal oxides for use in organic electronic devices.*

Materials research society spring conference. San Francisco 2013. **Oral**. *Deposition of Multiple Layers via Ultrasonic Spray Coating for Use in Organic Photovoltaic*

Devices

Commercialisation of Solar Research and Development. Loughborough University. **Oral**. *Indium Free Transparent Electrodes for Organic Solar Cells.*

UK Semiconductors. Sheffield 2013. **Oral**. *Deposition of Multiple Layers via Ultrasonic Spray Coating for Use in High Performance Organic Photovoltaic Devices*

International Symposium on Flexible Organic Electronics. Thessaloniki 2013. **Oral**. *Deposition of Multiple Layers via Ultrasonic Spray Coating for Use in High Performance Organic Photovoltaic Devices*

Abstract

One of the limiting factors in the efficiency of organic photovoltaic devices utilising new generations of donor polymers is the ability to obtain Ohmic contacts between the electrodes and the organic layers. This is due to the fact these new donor polymers often have deeper energy levels meaning that at the interfaces between the organic layer and the electrode contact barriers are formed. PEDOT:PSS is the current benchmark material that is used to reduce or remove these contact barriers however even this material has too shallower an energy level and has serious issues with long term stability. One possible class of materials that might overcome these limitations and give increased device performance and lifetimes are metal oxides. However these materials are currently deposited mainly through vacuum deposition and the difficulty of incorporating vacuum based depositions into roll-to-roll fabrication setups limits the commercial use of these materials.

Using a combination of spectroscopic techniques and device results this work shows that metal oxides can be used to effectively reduce these contact barriers and achieve high performance using deep energy level donor polymers. It has been shown that Vanadium (V) Oxide can be deposited from solution at room temperature without while maintaining high efficiencies. The work continues to look at spray coating, a roll-to-roll compatible deposition technique, and how it can be used to incorporate ultrathin film of solution processed Molybdenum (VI) Oxide for fabricating efficient devices. In addition I have shown that the processing of these materials is only limited by the possible introduction of metallic gap states that can occur due to high temperature processing.

Table of Contents

List of Figures

Chapter 1

Introduction

1.1 Organic Photovoltaics

Currently energy usage within many developed nations has still not reached a peak and in addition much growth in demand for energy is coming from developing nations due to more people demanding access to electricity.[1] It is expected that global energy consumption will double by 2050, and by 2100 it will have tripled.[2] In order to meet these demands new power plants have to be built. However there are several issues that have come to the attention of the public over the past decade that make the production of power stations reliant upon oil, coal, gas and nuclear less desirable. These issues include anthropogenic climate change being driven by the release of CO_2 in part from emissions from fuel burning power plants and fears about the safety of nuclear power after the Fukushima disaster which changed German and Japanese nuclear policy overnight.[3] In addition many areas of the developing world lack grid infrastructures for electricity to connect these large scale power plants to. This makes localised micro generation potenitally better suited to meet energy demands of developing nations. A combination of all these factors mean that many people are looking towards a clean, safe and renewable source of energy that can be deployed on both a small and large

scale to not only increase the total energy output but to eventually look towards reducing our reliance upon fossil and nuclear sources of energy.

According to the International Energy Agency the total electricity production for the world in 2009 was over 20 PWh with 19.8 percent of this being from what people would deem renewable sources with this increasing to 31% by 2035.[4,5] A breakdown of the renewable energy production reveals that over 83.3% of renewable generation is from hydroelectricity (including pumped storage).[4] These statistics show that renewable technologies that have had enough time to be developed and deployed upon a large scale, such as hydroelectricity can be used to great effect in producing large amounts of energy. However, one of the most promising forms of renewable energy is solar photovoltaics; the reason for this is the sheer amount of solar radiation that reaches the Earth and the ability to deploy on both large and small scales. The mean extraterrestrial solar irradiance at the distance Earth is from the sun is 1368W.m^{-2} this is known as the solar constant.[6] If the irradiance at a point on the surface is needed then atmospheric absorption has to be taken into account along with the angle that the ground makes to the Sun. It should be noted that the average solar irradiance at the Earth's surface is approximately 198 W.m^{-2}.[6] This means that the electricity consumption of the entire planet is equal to the amount of solar power that reaches an area of approximately 110,000Km^2. To put this into perspective, the amount of land that is currently covered by roads, buildings and pavements is approximately 580,000Km^2.[7]

It may seem like a simple matter of installing large swathes of photovoltaic panels over much of the land that has already been developed upon, but this scenario is not realistic. There are a few major issues that, at the moment, make this impractical; these issues include the fact that commercially available solar photovoltaic panels from

the world leading suppliers are currently at around 16% to 17% efficiency.[7,8] Photovoltaic panels also do not provide a constant source of energy, meaning that a method of storing power for when there is no sunlight is needed. The amount of energy that is required to produce inorganic photovoltaics is large due to the purification process of the Silicon substrates. Finally, the dollar-per-watt cost of power from solar photovoltaics is currently too high to make it economically viable to sell to many consumers.[8] Due to the almost negligible operating costs of solar photovoltaics, the only way to reduce the cost of the power that is generated is to reduce the initial cost of installation or to increase the output by increasing efficiency. However increases within the efficiency lead to increases in the cost of production; this is either because of the use of more expensive materials such as GaAs or the introduction of additional complexity in the architecture of the device in order to overcome the Shockley-Queisser limit.[10-12] There is a possibility however to reduce the cost of photovoltaics by the use of cheaper processing or materials such as organic semiconductors.[13-15]

Organic semiconductors are one of the possible ways of being able to produce cheap photovoltaic devices due to the simplicity of the fabrication process. Unlike most inorganic semiconductor devices they do not need to be fabricated onto a high-purity crystalline substrate, they, instead, can be deposited onto amorphous substrates such as glass, quartz and even flexible plastic materials.[14,16] This should lead to a large reduction in the cost of fabrication and to a reduction in the total amount of energy required to fabricate a device reducing the energy payback time for the device.[13,17,18] Organic semiconductors also have the advantage of not needing to be deposited in vacuum, they can be deposited using techniques that are already highly developed and see widespread use in multiple industries such as gravure printing, inkjet printing and

spray coating. These deposition methods can allow for an extremely high production volume, combined with the relatively low cost of materials the production of very cheap photovoltaic devices is possible.[13,19]

Even though devices based on organic semiconductors have several advantages over inorganic materials they fall short on two important factors: the efficiency of devices and the lifetime. Currently commercialisation of organic PV technology is being held back by these factors. In order to eventually realise full commercialisation, devices need to reach a minimum of 10% efficiency and to have a minimum lifetime comparable to inorganic photovoltaics of 10 years.[9] Currently in laboratory conditions it has been shown that in single-junction organic photovoltaic devices efficiencies as high as 9.2% have been reported, while double-junction have reported efficiencies as high as 12%.[21,22] The lifetime of organic photovoltaics are currently not as well reported as efficiencies of devices however recent work has shown promising results with lifetimes of devices ranging between 4 and 11 years.[10] It can currently be deduced that the efficiency and lifetime of laboratory based devices is approaching the speculated commercial breakthrough point for organic photovoltaics.

There are several pathways that have been used in order to improve the efficiencies and lifetimes of organic electronic photovoltaics. The most robust method of improving both of these is by the synthesis of new materials. Materials such as poly[N-9'-heptadecanyl-2,7-carbazole-alt-5,5-(4',7'-di-2-thienyl-2',1',3'-benzothiadiazole)] (PCDTBT), Poly [[4,8-bis[(2-ethylhexyl)oxy]benzo[1,2-b:4,5-b'] dithiophene-2,6-diyl] [3-fluoro-2-[(2-ethylhexyl)carbonyl] thieno[3,4-b]thiophenediyl]] (PTB7) and Poly(benzo[1,2-b:4,5-b′]dithiophene-*alt*-thieno[3,4-c]pyrrole-4,6-dione (PBDTTPD) are part of what is deemed the third generation of organic semiconducting

materials.[13,21,24-28] These types of materials are vastly more complicated in terms of the structure and synthesis than first, and even second generation materials, such as polyparaphenylene (PPV) and poly(3-hexylthiophene) (P3HT). These new materials offer more stable organic layers, higher mobility and increased ease of processing among other advantages.[23,24] However many of these third generation semiconductors have energy levels much deeper than the first and second generation, this means that benchmark materials such as poly(3,4-ethylene-dioxythiophene): poly(styrenesulfonate) (PEDOT:PSS) no longer allow for efficient charge transfer from the organic layer to the electrode due to inbuilt potential barriers.[29-31]

Energy barriers that form when there is no longer Ohmic contact between the layers lead to large reductions in the device performance from the theoretical maximum value for any given material, it can also lead to reductions in the lifetimes of devices.[32,33] Therefore obtaining Ohmic contacts between the organic layers and the electrodes is an important part of making a highly efficient and stable device. In order for an Ohmic contact to be formed at the interfaces between the organic layers and the electrodes a new class of materials is needed. Metal oxides have seen much interest over that past several years as possible candidates for helping form these contacts.[34,35] Oxides not only have deep energy levels they also have several other properties that make them desirable for use in organic electronic devices. They often have large band gaps leading to optically transparent films, some oxides can also act as charge blocking layers leading to further performance increases, different metals and different oxidation states allow for a large selection of possible materials to match energy levels with, they have higher stability than many other materials, can act to dope adjacent layers and can be deposited from solution.[34-42]

Much of the work that has been done on metal oxides has been focused on the use of vacuum evaporated Molybdenum (VI) Oxide as a replacement for PEDOT:PSS with increased interest recently in the solution processing of this material. However there is still little effort into studies of scaling of these material and few studies on the fundamentals of what is happening at the interfaces between these layers especially with regards to the effects of different processing conditions. In order to understand why improvements are often seen, detailed knowledge of the varying properties of these deposited layers are needed. Up until recently it was believed that the electronic structure for most metal oxides was known and was at a fixed value however much of this has changed with the revelation that not only is the electronic structures of these metal oxide films much deeper but that they can vary depending upon processing parameters.

1.2 Summary of This Thesis

The purpose of this work is to characterise the electronic structure of hole extracting metal oxides for the use in organic photovoltaic devices and to determine appropriate materials for the replacement of the commonly used hole extraction layer PEDOT:PSS. Upon finding suitable replacements, studies of solution processed versions of these metal oxides have been explored, and how different processing methods affect the performance of these materials investigated. Finally the ability to transfer these solution processable metal oxides from spin coating of the layers to spray coating of the layer is reported. In **Chapter 2** background knowledge of the theory of organic semiconductors, metal oxides and the interactions that occur at the interfaces of these materials is given.

Chapter 3 covers the fabrication techniques used in order to make the organic photovoltaic devices and thin film samples and discusses the measurement of these devices along with the origins of the parameters that affect their performance. In **Chapter 4** the methods for characterising thin films of the materials used and the theory behind these techniques are presented. These include ultra-violet photoelectron spectroscopy, x-ray photoelectron spectroscopy, spectroscopic ellipsometry and atomic force microscopy.

Chapter. 5 describes the characterisation of hole extracting metal oxides deposited via vacuum deposition and organic semiconductors that are used in the fabrication of organic bulk-heterojunction within organic photovoltaic devices. The results show that the hole extracting metal oxides that are studied exhibit similar characteristics with deep work functions and Fermi levels pinned close to the conduction band of the material leading to a p-type semiconducting material. In addition these materials often have wide band gaps allowing for low loss within the intensity of light entering the organic bulk-heterojunction. (reference your publication here – and similarly in the next chapters)

Chapter 6 reports the use of a solution processable version of Vanadium (V) Oxide called Vanadium (V) Isopropoxide and how different processing conditions affect the performance of these devices. Comparisons against vacuum deposited Vanadium (V) Oxide and PEDOT:PSS as hole extraction layers are made and it can be seen that the solution processable Vanadium (V) Oxide shows comparable performances to both PEDOT:PSS and vacuum deposited Vanadium (V) Oxide.

In **Chapter 7** the study of depositing a solution processed form of Molybdenum (VI) Oxide via an ultrasonic spray coating technique that can be placed within a roll-to-roll deposition setup. Ammonium Molybdate Tetrahydrate has been shown previously to exhibit high performances while allowing for low temperature solution processing in spin coated devices. Transferring this to the ultrasonic spray coating technique, the results showed a strong dependence upon the solvent used along with the thickness dependence. Once below a critical thickness the deposited layer allows for efficient extraction of holes and the control of this thickness is highly dependent upon the deposited solution.

The final experimental **Chapter 8** looks at the effects of changes in oxidation state of the metal oxide Molybdenum (VI) oxide has been studied as these can be introduced via the processing of both vacuum deposited and solution processed metal oxides. The results indicate that the presence of specific oxidation states can have a dramatic effect upon the performance of organic photovoltaic devices. Lower oxidation states of Molybdenum Oxide result in the reoccupation of lower binding energy orbitals causing a shift of the work function to lower binding energies introducing extraction barriers for holes.

The conclusion of this work is reported in Chapter 9. Overall it has been discovered that the metal oxides are effective materials for obtaining low resistance contacts for the interfaces between organic semiconductors and the electrodes. It is also possible to transition from the costly vacuum based processing that metal oxides have previously been deposited with, towards solution processing without losing device performance; in addition it is possible to deposit these solution based materials via roll-to-roll compatible techniques.

1.3 References

[1] J. Conti & P. Holtberg. International Energy Outlook. U. S Energy Information Administration. (2011)

[2] N. S. Lewis & D. G. Nocera. Powering the Planet: Chemical Challenges in Solar Energy Utilization. *PNAS*. **103**. (2006) 15729-15735

[3] F. Birol .World Energy Outlook. *International Energy Agency*. (2009)

[4] F. Birol. World Energy Outlook. *International Energy Agency*. (2012)

[5] P. V. Hobbs & J. M. Wallace. *Atmospheric Science: An Introductory Survey*. (Ch. 4), Burlington: Elsevier (2006)

[6] C. D. Elvidge, B. T. Tuttle, P. C. Sutton, K. E. Baugh, A. T. Howard, C. Milesi, B. L. Bhaduri & R. Nemani. Global Distribution and Density of Constructed. *Sensors*. **7**. (2007) 1962-1979

[7] Yingli Solar. *Panda 48 Cell 40mm SERIES Data Sheet*. 11/2012 http://www.yinglisolar.com/assets/uploads/products/downloads/PANDA_48_Cell_Series_EN.pdf 4/2013

[8] Yingli Solar. YGE 72 Cell NH SERIES Data Sheet. 11/2012. http://www.yinglisolar.com/assets/uploads/products/downloads/YGE_72_Cell_Series_EN.pdf 4/2013

[9] K. Zweibel. Should solar photovoltaics be deployed sooner because of long operating life, at low, predictable cost? *Energy Policy*. **38**. (2010) 7519-7530

[10] M. A. Green. Third generation photovoltaics: Ultra-high conversion efficiency at low cost. *Progress in Photovoltaics*. **9**. (2001) 123-135

[11] J. Nelson. *The Physics of Solar Cells*. London: Imperial College Press (2003)

[12] W. Shockley &. H. J. Queisser. Detailed Balance Limit of Efficiency of p-n Junction Solar Cells. *Journal of Applied Physics*. **32**. (1961) 510-519

[13] B. Azzopardi, C. J. M. Emmott, A. Urbina, F. C. Krebs, J. Mutale & J. Nelson. Economic assessment of solar electricity production from organic-based photovoltaic modules in a domestic environment. *Energy & Environmental Science*. **4**. (2011) 3741-3753

[14] B. Kippelen & J. L. Bredas. Organic Photovoltaics. *Energy & Environmental Science*. **2**. (2009) 241-332

[15] C. J. Brabec. Organic photovoltaics:technology and market. *Solar Energy Materials & Solar Science*. **83**. (2004) 273-292

[16] J. R. Sheats. Manufacturing and commercialization issues in organic electronics. *Journal of Materials Research*. **19**. (2004) 1974-1989

[17] C. J. Emmott, A. Urbina & J. Nelson. Environmental and economic assessment of ITO-free electrodes for organic solar cells. *Solar Energy Materials & Solar* Cells. **97**. (2012) 14-21

[18] N. Espinosa, R. Garcia.-Valderi, A. Urbina & F. C. Krebs. A life cycle analysis of polymer solar cell modules prepared using roll-to-roll methods under ambient conditions. *Solar Energy Materials & Solar Cells*. **95**. (2011) 1293-1302

[19] A. J. Moule. Power From Plastic. *Current Opinion in Solid State and Materials Science*. **14**. (2010) 123-130

[20] R. Søndergaard, M. Hösel, D. Angmo, T. T. Larsen-Olsen & F. C. Krebs. Roll-to-roll fabrication of polymer solar cells. *Materials Today*. **15**. (2012) 36-49

[21] Z. He, C. Zhong, S. Su, M. Xu, H. Wu & Y. Cao. Enhanced power-conversion efficiency in polymer solar cells using an inverted device structure. *Nature*

Photonics. **6**. (2012) 591-595

[22] Heliatek. *Helitaek consolidates its technology leadership by establishing a new world record for organic solar technology with a cell efficiency of 12%*. 1/2012 http://www.heliatek.com/wp-content/uploads/2013/01/130116_PR_Heliatek_achieves_record_cell_effiency_for_OPV.pdf 4/2013

[23] C. H. Peters, I. T. Sachs-Quintana, J. P. Kastrop, S. Beaupré, M. Lecrec & M. D. McGehee. High Efficiency Polymer Solar Cells with Long Operating Lifetimes. *Advanced Energy Materials*. **1**. (2011) 491-494

[24] A. J. Heeger. Semiconducting polymers: the Third Generation. *Chemical Society Reviews*. **39**. (2010) 2354-2371

[25] S. Wakim, S. Beaupré, N. Blouin, B. R. Aichi, S. Rodman, R. Gaudina, Y. Tao & M. Lacrec. Highly efficient organic solar cells based on a poly(2,7-carbazole) derivative. *Journal of Materials Chemistry*. **19**. (2009) 5351-5358

[26] M. S. Almeataq, H. Yi, S. Al-Faifi, A. A. B. Alghamdi, A. Iraqi, N. W. Scarratt, T. Wang & D. G. Lidzey. Anthracene-based donor–acceptor low band gap polymers for application in solar cells. *Chemical communications*. **49**. (2013) 2252-2254

[27] Y. Liang, Z. Xu, J. Xia, S. T. Tsai, Y. Wu, G. Li, C. Ray & L. Yu. For the Bright Future—Bulk Heterojunction Polymer Solar Cells with Power Conversion Efficiency of 7.4%. *Advanced Materials*. **22**. (2010) E135-E138

[28] Y. Zou, A. Najari, P. Berrouard, S. Beaupré, B. R. Aïch, Y. Tao & M. Leclerc. A Thieno[3,4-c]pyrrole-4,6-dione-Based Copolymer for Efficient Solar Cells. **132**. (2010) 5330-5331

[29] J. Hou, Z. Tan, Y. Yan, Y. He, C. Yang & Y. Li. Synthesis and Photovoltaic

Properties of Two-Dimensional Conjugated Polythiophenes with Bi(thienylenevinylene) Side Chains. *Journal of American Chemical Society*. **128**. (2006) 4911-4916

[30] G. Greczynski, T. Kugler, M. Keil, W. Osikowicz, M. Fahlman & W. R. Salaneck. Photoelectron spectroscopy of thin films of PEDOT–PSS conjugated polymer blend: a mini-review and some new results. *Journal of Electron Spectroscopy and Related Phenomena*. 121. (2001) 1-17

[31] E. L. Ratcliff, J. Meyer, K. X. Steirer, N. R. Armstrong, D. Olson & A. Kahn. Energy level alignment in PCDTBT:PC70BM solar cells: Solution processed NiOx for improved hole collection and efficiency. *Organic Electronics*. **13**. (2012) 744-749

[32] H. Ma, H. L. Yip, F. Huang & A. K. Y. Jen. Interface Engineering for Organic Electronics. *Advanced Functional Materials*. **20**. (2010) 1371-1388

[33] B. Zimmermann, U. Würfel & M. Niggemann. Longterm stability of efficient inverted P3HT:PCBM solar cells. *Solar Energy Materials and Solar Cells*. **93**. (2009) 491-496

[34] M. T. Greiner, M. G. Helander, W. M. Tang, Z. B. Wang, J. Qiu & Z. H. Lu. Universal energy-level alignment of molecules on metal oxides. N*ature Materials*. **11**. (2012) 76-81

[35] V. Shrotriya, G. Li, Y. Yao, C. W. Chu & Y. Yang. Transition metal oxides as the buffer layer for polymer photovoltaic cells. *Applied Physics Letters*. **88**. (2006) 073508

[36] J. Griffin, D. C. Watters, H. Yi, A. Iraqi, D. G. Lidzey & A. R. Bucklry. The Influence of MoOx Anode Stoicheometry on the Performance of Bulk

Heterojunction Polymer Solar Cells. *Advanced Energy Materials*. 2013. DOI: 10.1002/aenm.201200886

[37] S. Murase & Y. Yang. Solution Processed MoO3 Interfacial Layer for Organic Photovoltaics Prepared by a Facile Synthesis Method. *Advanced Materials*. **24**. (2012) 2459-2462

[38] M. Kröger, S. Hamwi, J. Meyer, T. Riedl, W. Kowalsky & A. Kahn. P-type doping of organic wide band gap materials by transition metal oxides: A case-study on Molybdenum trioxide. *Organic Electronics*. **10**. (2009) 932-938

[39] J. Bouclé, P. Ravirajan & J. Nelson. Hybrid polymer–metal oxide thin films for photovoltaic applications. *Journal of Materials Chemistry*. **17**. (2007) 3141-3153

[40] M. Tadatsugu. New n-Type transparent conductors. *MRS Bulletin*. **25**. (2000) 38-44

[41] J. Y. Kim, K. Lee, N. E. Coates, D. Moses, T. Q. Nguyen, M. Dante & A. J. Heeger. Efficient Tandem Polymer Solar Cells Fabricated by All-Solution Processing. *Science*. **317**. (2007) 222-225

[42] M. S. White, D. C. Olson, S. E. Shaheen, N. Kopidakis & D. S. Ginley. Inverted bulk-heterojunction organic photovoltaic device using a solution-derived ZnO underlayer. *Applied Physics Letters*. **89**. (2006) 143517

Chapter 2

Theory of devices

2.1 Introduction

In this chapter information on underlying theories behind organic semiconducting materials and metal oxides are discussed. This begins by looking at the origins of atomic and molecular orbitals and orbital hybridization as these are crucial in understanding the formation of the electronic structure of these materials. Afterwards the origins of the electronic properties of organic materials are discussed including band formation, charge transportation and charge carrier interactions. Similarly further insight into the atomic orbitals of transition metals is given and how this relates to band structure. Finally the theories behind interfacial mechanics are discussed with respect to the various interfaces that are encountered within organic photovoltaic devices.

2.2 Atomic and Molecular Orbitals

Electrons that are present within an atom are said to be within orbitals around their nucleus, these orbitals are not like the traditional view of an orbiting body but are rather a probability that an electron will be found within a specific location around an atom due to the uncertainty principle. [1] The shape and occupation of these orbitals are determined by the four quantum numbers: the principal quantum number n which is the potential energy of the electron; Azimuthal quantum number ℓ which is the magnitude of the angular momentum of the electron; the magnetic quantum number m_ℓ which is the direction of the angular momentum; and the spin quantum number m_s which is the direction of spin of the electron. [2]

The values that these numbers can take are all integers, except for the spin where the spin value for an electron is ½. All of these numbers are determined by a specific set of statement given by **Equations 2.1** to **Equation 2.4**. [3]

$$1 \leq n \qquad \textbf{Equation 2.1}$$

$$0 \leq l \leq n-1 \qquad \textbf{Equation 2.2}$$

$$-\ell \leq m_\ell \leq \ell \qquad \textbf{Equation 2.3}$$

$$-s \leq m_s \leq s \qquad \textbf{Equation 2.4}$$

By using these statements and obtaining values for each of the quantum numbers it is possible to determine the shape of the orbitals and also the amount of electrons that can occupy a specific orbital. **Table 2.1** shows the quantum numbers and the amount of electrons in the first couple of shells. In the first shell only two electrons are able to

occupy this region and they are within what is known as the 1s orbital. S-orbitals occur when the angular momentum quantum number is 0 this means that there are 2s, 3s, 4s orbitals each containing 2 electrons. In the second shell the angular momentum quantum number can also be equal to 1, any electron with an ℓ value equal to 1 are within a p-orbital. The axis about which the p-orbital is orientated is determined by the vector value m_ℓ therefore in the second shell the p-orbital become split into 3 different kinds the $2p_z$, $2p_y$ and $2p_x$ all with equal energy. In higher energy shells there are more orbitals present, these are the d and f orbitals and these occur when ℓ is equal to 2 and 3 respectively. These orbitals often have complex shapes and orientations and are not present within most organic materials however they are important in metal oxides and so will be discussed in **Chapter 2.7**

n	ℓ	m_ℓ	m_s	Total electrons
$n = 1$	$\ell = 0$	$m_\ell = 0$	$m_s = 1/2$	2
			$m_s = -1/2$	
$n = 2$	$\ell = 0$	$m_\ell = 0$	$m_s = 1/2$	8
			$m_s = -1/2$	
	$\ell = 1$	$m_\ell = -1$	$m_s = 1/2$	
			$m_s = -1/2$	
		$m_\ell = 0$	$m_s = 1/2$	
			$m_s = -1/2$	
		$m_\ell = 1$	$m_s = 1/2$	
			$m_s = -1/2$	

Table 2.1 Values for the various quantum numbers and the total possible amount of electrons that can occupy a given shell are shown. Only the first two shells are shown for simplicity.

In organic semiconductors all the atoms are part of molecules and in order to form a molecule covalent bonds between atoms need to be formed. When two atoms are brought close enough together molecular orbitals are created these are the combination of overlapping atomic orbitals. **Figure 2.1** shows how when bringing an atom with half filled s-orbitals close together the bonding and anti-bonding orbitals form and shows how the energy of these orbitals varies. Bonding orbitals form a single electron cloud between the two atoms that is occupied by the first two electrons. The energy of the bonding molecular orbitals is lower due to increased electron density between the atoms, electrons within this area have a larger Coulombic force between them and the nuclei resulting in a tighter bound electron. [4]If one or more atoms have a full shell the additional electrons cannot occupy the bonding orbital due to the Pauli Exclusion Principle therefore they must occupy the anti-bonding orbital. [5] Electrons in this orbital do not occupy the region between the nuclei, this reduces shielding of the atomic charge and leads to a higher energy orbital and a less stable molecule. [4]

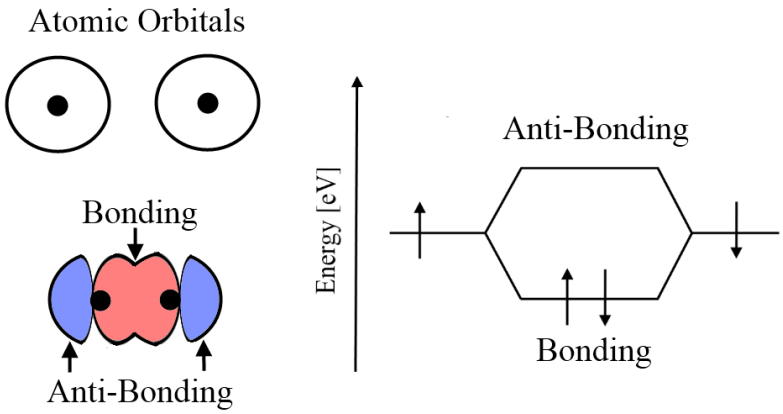

Figure 2.1 Shows how bringing atomic orbtials close enough to overlap leads to the formation of bonding and anti-bonding orbtials. In addition the energy of the molecular orbitals of hydrogen are shown.

In addition to whether a molecular orbital is bonding or anti-bonding it can also either be a σ or π bond. These two types of bonds depend upon the symmetry of the atomic orbitals with relation to the axis joining the two nuclei. When the atomic orbital is symmetrical around the axis that the atoms are adjoined through it is called a σ-bond. When the orbitals are asymmetrical around the axis through which the atoms are adjoined the bond is a π-bond. [4] **Figure 2.2** shows the individual atomic orbitals and the combined molecular orbitals, the σ-bond is situated directly between the two atoms and the electrons within these orbitals provide shielding of the nuclear charges. Similarly the π-bond provides shielding but the orbital formed due to π-bonding is skewed away from the adjoining axis either in the y-axis or z-axis. This skewing of the orbital leads to a lower electron density between the two nuclei this results in a lower attraction from the two nuclei reducing the strength of the Coulombic interactions. Therefore σ-bonds are stronger and more stable than π-bonds.

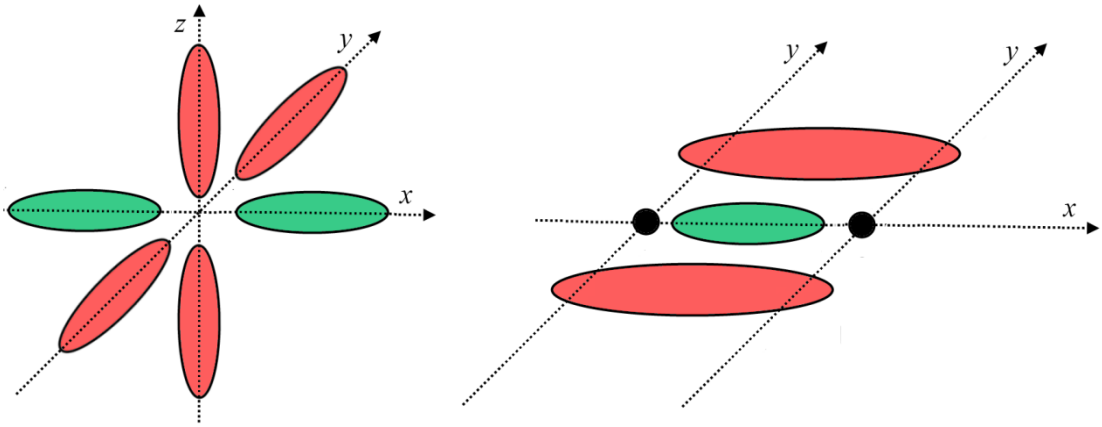

Figure 2.2 Shows a simplified diagram of the p-orbitals of an individual and two overlapping atoms, p-orbitals parallel to the adjoining axis (green orbitals) form σ-bonds and those perpendicular (red orbitals) form π-bonds.

2.2 Orbital Hybridization

Organic molecules consist mainly of carbon, hydrogen and oxygen so it is important to see what kind of molecular orbitals are formed in carbon based molecules, **Figure 2.3** shows one of the simplest organic materials around - methane. It consists of one carbon atom surrounded by four hydrogen atoms. In any atom the electron shells are filled in a specific order and for low atomic number atoms the electrons fill up in the order $1s^2$, $2s^2$, $2p^2$, $3s^2$ and $3p^6$. For carbon six electrons are present and the orbitals fill up $1s^2$, $2s^2$, $2p^2$ this means that only two electrons within the p-orbtials are available to form stable molecular orbitals. Accordingly, that would mean that it is not possible to form methane and that the maximum amount of hydrogen atoms that could bind to carbon would be two. This, however, isn't true due to a process called orbital hybridization, in almost all organic materials orbital hybridization of carbon occurs allowing for carbon to fill its 2p level resulting in an electronic configuration of $1s^2$, $2s^1$, $2p^3$.[4, 6, 7]

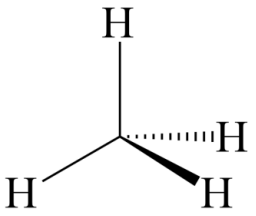

Methane

Figure 2.3 Methane is one of the simplest organic materials consisting of a central carbon atom covalently bonded to four hydrogen atoms to give a full shell of outer electrons.

This happens is a two step process in which an electron is excited from the 2s orbital into the 2p orbital. In the case of methane when a hydrogen atom is brought close to the carbon the hydrogen imparts an attractive force due to electromagnetism, this excites one of the electrons in the 2s orbital to the 2p orbital. When this is done the electronic configuration then becomes $1s^2$, $2s^1$, $2p_x^1$, $2p_y^1$, $2p_z^1$ giving us four half filled atomic orbtials that can form molecular orbtials. Afterwards the second step, which is called hybridization, occurs; this is the formation of a new kind of orbital called an sp orbital. [4] This sp orbital is a mixture, or hybrid, of the individual s and p atomic orbitals leading to the formation of new degenerate atomic orbitals. The amount of sp orbitals within an atom depends upon the degree of hybridization. There are three degrees of hybridization: sp^3, sp^2 and sp. **Figure 2.4** shows the different degrees of hybridization, in sp^3 hybridization three p-orbitals are mixed with the s-orbital forming four new non-overlapping sp orbitals. For sp^2 and sp^1 hybridization, 3sp and 2sp orbitals are formed respectively.

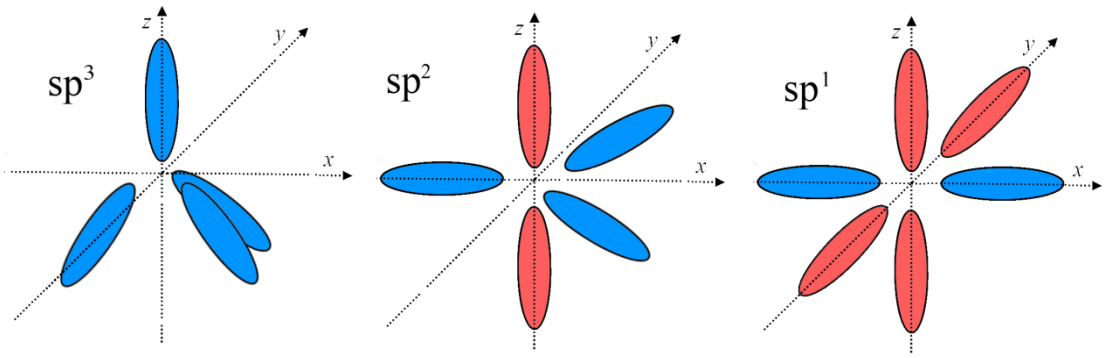

Figure 2.4 sp^3, sp^2 and sp hybridized with the sp hybrid orbitals in blue and the p-orbitals in red.

2.3 Conjugation and Band Formation

The theory of atomic orbitals, molecular orbitals and orbital hybridization although being informative, does not directly give the reason behind why some organic materials can exhibit electronic properties similar to semiconductors and metals. The reason behind these various properties is due to the presence of alternating single-double or single-triple covalent bonds along a molecule or monomer, this alternation of bonds is called conjugation. Benzene is a commonly used example of conjugation; **Figure 2.5** shows a molecule of benzene one of the most common components in many organic semiconducting materials, it is a ring of six sp^2 hybridized carbon atoms surrounded by 6 hydrogen atoms with alternating single double bonds. [4] If we look at the position that the double bonds can take around the molecule they can either be in positions shown in benzene one or benzene two. The positioning of these double bonds makes no difference to the molecule overall and the two types of benzene are, in essence, indistinguishable. It is this indistinguishable nature that allows the π-bonds to be in both positions at once making them delocalised across the entire chain of conjugation.[4, 7] This dissociation of the π-bonds means that these molecular orbitals become spread across the entire length of conjugation, this leads to a probability that the electrons within the π-bonds of benzene will be found anywhere around the ring.

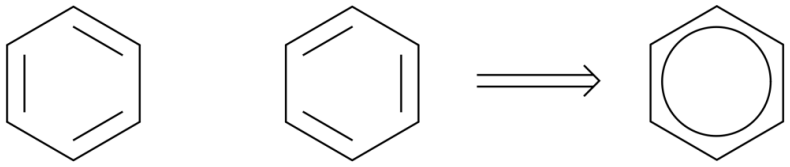

Benzene 1 Benzene 2 Benzene 3

Figure 2.5 Benzene 1 and 2 show the different π-bond locations that are possible. Due to both molecules being indistinguishable it can be said that the bonds are delocalised across the entire benzene ring as shown in benzene 3.

This delocalised orbital, due to being a π-bond, is the weakest bound molecular orbital and hence has the highest energy, it is therefore called the highest occupied molecular orbital (HOMO). This HOMO level in organic semiconductors is often classed as being analogous to the valence band in inorganic semiconductors and likewise organic materials have something similar to the conduction band and this is called the lowest unoccupied molecular orbital (LUMO) which is the π-antibonding orbital, similarly organic materials have a bandgap and this is the difference in energy between the HOMO and the LUMO.

Molecular orbital energies are not just affected by the individual atoms that are involved they are also influenced by the surrounding environment. Within films of a material changes within the environment lead to slightly shifted molecular orbital energies. These shifts affect both the HOMO and the LUMO levels and the amount the HOMO and LUMO vary within a material is known as the energetic disorder.[8-10] Within ordered materials such as molecular crystals the surrounding environment is a repeating structure, this leads to little variation in the energy level of the HOMO.

However for poly-crystalline or amorphous materials there is little order, leading to small perturbations in the energy levels of the HOMO giving a wide band for these disordered materials. **Figure 2.6** shows the difference in HOMO and LUMO level structure for ordered and disordered materials. Variation in the energy levels is important with regards to both charge transport and also charge transfer between materials.

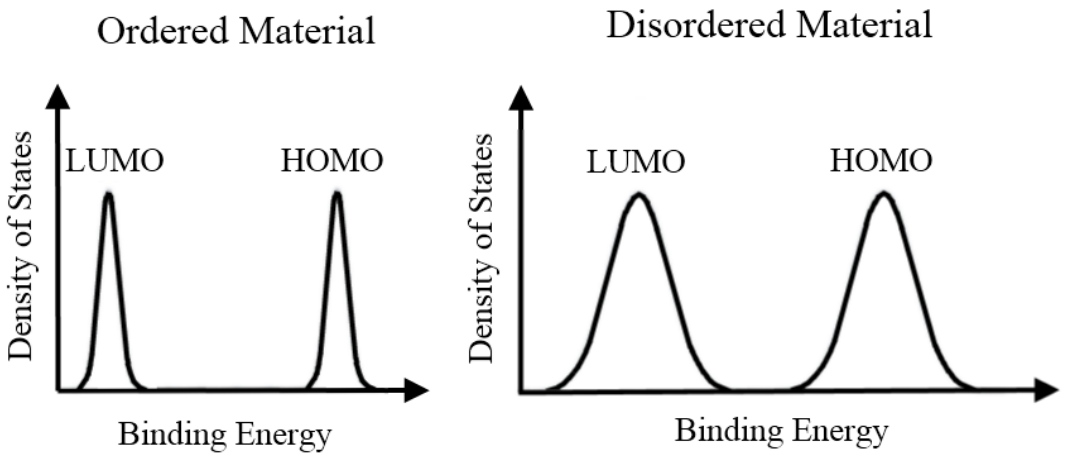

Figure 2.6 Shows how the densities of different energy states vary for materials that are energetically ordered and for those that are energetically disordered.

2.4 Charge Transport

The delocalisation of the HOMO and LUMO across a molecule or monomer through conjugation of the carbon bonds leads to the delocalisation of electrons along the conjugation length allowing for charge transport. Delocalisation, however, can only occur between states of equal energy, in materials with disorder the energy levels vary

due to localised effects. These variations in energy levels lead to the formation of localised states and it is transport between these localised states that determine the mobility of charge carriers in the organic semiconducting materials used in this work.[8, 11] There is currently no universally accepted way of completely describing transport of charge carriers through localised states within a material; though it is agreed that transport is due to a hopping process that is dependent upon both the energetic disorder of the localised sites and the positional disorder.[11, 12] Hopping is a process in which the electron tunnels from one localized state to the next; if the binding energy of the two sites is not equal the tunnelling process is also associated with a phonon.[11, 13, 14] The probability of hopping is dependent upon the difference in energy of the localised states and also the physical separation of these localised states. In order to increase charge transportation both of these need to be reduced, this can be done by the control of the chemical structure and the processing conditions. Physical distance between charge transport sites can be reduced intramolecularly by reducing the distance between charge transport sites on monomers or by increasing the conjugation length.[15, 16] In addition the intermolecular distance can be reduced by lowering the stacking distance between polymer chains by crystallizing the polymers.[17, 18] These effects not only lead to a reduction in the distance between localized states but also have the additional effect of reducing the energetic disorder.

2.5 Charge Carrier Interactions

The HOMO and LUMO have been treated as either fully occupied or empty however when looking at charge transport or injection of charge carriers at an interface this is not

true. In organic materials charges carriers are either classed as a hole within the HOMO level or an electron within the LUMO level. The presence of these charge carriers means that there are changes in the occupation of certain orbitals. In the case of an excited electron in the LUMO the electron occupies the π-anti-bonding orbital; these orbitals are unstable though due to the presence of σ-bonding molecular orbitals the molecules stay intact. Deformations within the area surrounding the occupied π-anti-bonding orbital occurs leading to a relaxation of the surrounding bonds reducing the overall energy of the molecule and the LUMO and increasing the stability of the π-anti-bonding orbital.[7, 8] This interaction between the excited electron and the surrounding environment can be seen as a quaziparticle known as an electron polaron. Similarly the presence of a hole within the HOMO causes changes within the surrounding bonds that cause the reduction of the energy of the whole molecule to reduce leading to an increase in the energy of the HOMO. This combined effect of lattice distortion and hole is called a hole polaron. **Figure 2.7** shows the shifts in energy levels for the hole and electron polarons in comparison to the ground state.

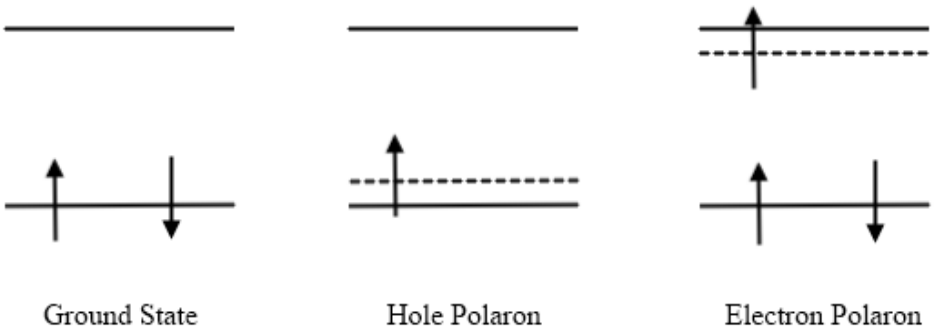

Figure 2.7 Interactions between charge carriers and their surroundings cause shifts in the energy of the orbitals resulting in a shallower HOMO level and a deeper LUMO.

When a photon is absorbed by the organic material promotion of an electron from the HOMO to the LUMO leads to the formation of an electron/hole polaron pair and due to close proximity the Coulombic attraction leads to them forming a bound pair. The strength of this attraction is much higher in organic semiconductors due to the low dielectric constant leading to a lower shielding of the Coulombic force. This results in a tightly bound exciton known as a Frenkel exciton that cannot be dissociated thermally.[19] In organic photovoltaics exciton dissociation can achieved at an interface between the absorbing material and a second semiconductor known as the acceptor which has a deeper LUMO level. The difference in the LUMO's of the materials has to be higher than the potential required to split the exciton; this is typically given as around 0.3V.[19-21]

Excitons are short lived and in organic materials, they typically have a lifetime on the order of nanoseconds giving a diffusion length of 10nm.[22-23] If an exciton is formed further from an interface than this length or is unable to dissociate at the interface the exciton undergoes geminate recombination. In organic photovoltaics this path length limitations are overcome by using a mixed phase of two materials known as the electron donor and electron acceptor materials are used. By depositing both of these materials from solution a diffuse interface throughout the device is formed known as a bulk-heterojunction.[24,25] Upon arriving at the interface dissociation of the excitons can occur in which the hole polaron remains within the donor layer and the electron polaron is transferred to the acceptor via charge transfer states. In addition excitons pairs can also recombine at the interface due to trap states. If the exciton is able dissociation other recombination mechanisms can occur these are classed as non-geminate recombination as the electrons and holes do not originate from the same exciton. Defect states can act

as charge recombination sites where a charge carrier can become trapped in an energy state that is within the band gap of the material. Recombination can also occur at the charge extraction interface due to interfacial states or defect states that are present.

2.6 Electronic Structure of Transition Metal Oxides

The filling of orbitals is dependent upon their binding energy with the highest binding energy orbitals being occupied first. An electron with a principle quantum number *n* can occupy one of several orbitals as mentioned in **Section 2.2**, these orbitals are designated as s, p, d or f depending upon their Azimuthal quantum number *l* which is 0, 1, 2 or 3 respectively for these orbitals. [2] With increased angular momentum the orbit of the electron is spread over a larger area and further away from the nucleus of the atom on average. [26] In multi-electron atoms this leads to the breakdown in the degeneracy of electrons with the same quantum number but varying angular momentums. This is due to variations in the effective shielding of full sub shells; **Figure 2.8** shows the probability of finding an electron at a specific distance away from the nucleus for the different orbitals of an atom. It can be seen that for the 2s-orbital there is a significant chance of finding the electron within the 1s-orbital, this penetration into the full sub-shells circumvents a portion of the electron density of the 1s-orbital that shields the electron that would occupy this orbital. This increases the Coulombic attraction between the nucleus and an electron within the 2s-orbital in comparison to the 2p-orbital effectively reducing the energy of the orbital and increasing the electrons binding energy.

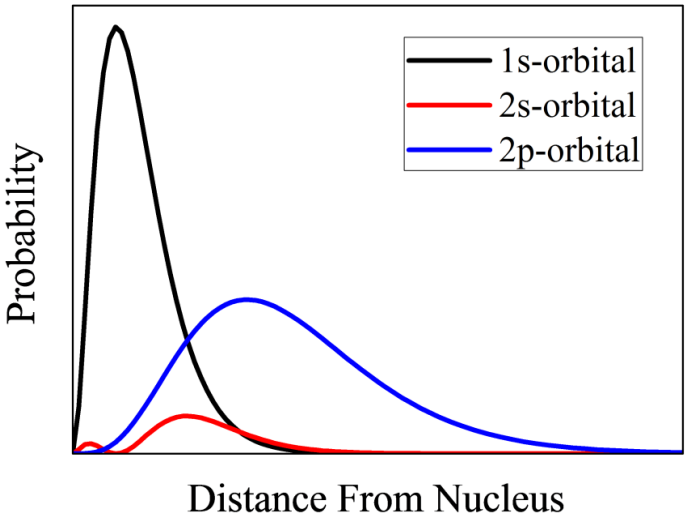

Figure 2.8 The probability of finding an electron in the 1s, 2s and 2p shell of an atom as a function of the radial distance away from the nucleus.

This leads to the filling of atomic orbitals in a specific order, for the first two periods of transition metals the filling order of the atomic orbitals is 1s, 2s, 2p, 3s, 3p, 4s, 3d, 4p, 5s and then 4d. The filling order deviates from this due to spin-orbit coupling that occurs between the spin of an electron and the orbital angular momentum. This has no bearing on s-orbitals as they have zero angular momentum but for p-orbitals and d-orbitals spin-orbit coupling leads to the splitting of the energy levels due to either constructive or destructive interference between the generated magnetic fields. [26] Energy levels in transition metal oxides can therefore closely overlap; examples of this are the 4s and 3d levels and the 5s and 4d levels. This close overlap can cause variations in the filling of orbitals when spin-spin interaction is taken into account. Orbit-orbit interactions occur when filling an orbital with electrons of opposite spin, as these two electrons do not violate the Pauli exclusion principle they can occupy the same position,

this leads to an increase in the energy of the orbital due to Coulombic repulsion between the electrons. An example of this is Molybdenum is [Kr] $5s^1$ $4d^5$ where the 5s orbital is lower in energy than the $4d^{3/2}$ orbital only when occupied by a single electron. This leads to the half filling of the 5s orbital and then the 4d orbital begins to fill. **Figure 2.9** shows the effects on the orbital energy levels for the spin-orbit and spin-spin interactions.

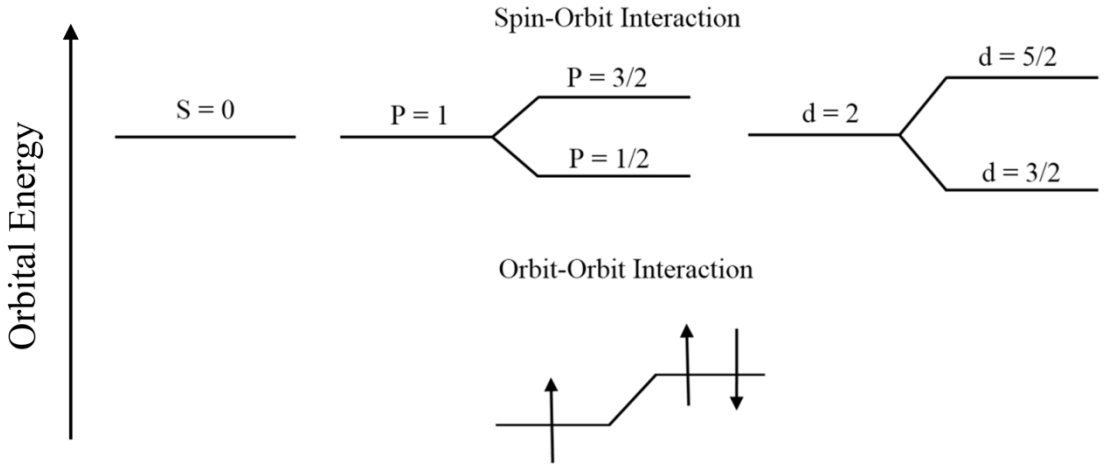

Figure 2.9 Spin-Orbit interactions cause shifts in the energies of orbitals with angular momentum due to the constructive or destructive interference of the electron spin with the angular momentum component. Orbit-Orbit interactions cause an increase in the orbital energy due to Coulombic repulsion of electrons within the same orbital.

By knowing the electron configuration of a metal oxide it is possible to determine the electron configuration of the metal atoms and the oxygen atom within a metal oxide. Due to the high electronegativity of the oxygen atom, the electron density within the

orbitals of the metal oxide is stripped from the higher d-orbitals and s-orbitals essentially forming a highly ionic bond. This electron density goes towards filling the partially occupied 2p orbital within oxygen.[27, 28] This leads to several classes of metal oxides that depend on the amount of electrons left within the d and s orbitals. High oxidation state metal oxides such as MoO_3, WO_3 and V_2O_5 have all electrons removed from the d-orbitals and s-orbtials. This results in the lowest occupied atomic orbital being the O2p-orbital; this then becomes the valence band of the metal oxide with the now empty s-orbitals and d-orbitals becoming the conduction band.[28, 29] These metal oxides are what will be studied within this body of work.

2.7 Energy Level Alignment and Interfacial Mechanics

Electronic structures of materials that are used in organic photovoltaic devices have been described and for both organic materials and metal oxides they have been shown to be semiconductors. Both material types have a conduction band and valence band with the Fermi level for these materials within the gap between these bands. In devices it is often useful to compare the energy level structures of two materials to determine how effective they will be within a device. When referencing two materials against each other vacuum alignment conditions are used in which all energies are relative to the vacuum level this is where the electron is not affected by the potential of the material.[30, 31] This alignment condition holds true between two materials as long as they are not in electrical contact with one another; when materials are brought into contact to form an interface transfer of charges can occur. When this occurs under specific conditions

Fermi level alignment can occur where the Fermi levels of the two materials equalise with the formation of an interfacial dipole. [31]

Figure 2.10 shows the energy level structure for vacuum level aligned and Fermi level aligned interfaces for different materials. The simplest interface is the metal-metal interface that occurs at the Calcium Aluminium cathode within devices. When in contact electrons flow from the shallow Fermi level material to the deeper material, this rearrangement of charge leads to the formation of the interfacial dipole. For metal-organic contacts they can either align to the LUMO level or HOMO level, this occurs if the work function of the metal is shallower than the upper critical Fermi level (Φ_P) of the organic layer for LUMO level alignment or deeper than the lower critical Fermi level (Φ_N) for HOMO level alignment. If the work function of the metal is between these values Fermi level alignment is not satisfied and the interface will remain vacuum level aligned. [32]The method by which a dipole forms for metal-organic interfaces is not just due to the transfer of electrons from an energy level on one material to the next. Additional effects such as chemical reactions, the formation of additional interfacial states, or permanent dipoles within the organic layer can affect the interfacial dipole.[30, 33, 34] This makes being able to determine the dipole between these two interfaces from knowledge of the individual materials is difficult as these effects are difficult to take into account when aligned against vacuum. HOMO level alignment at the interfaces between organic materials and metal oxides have recently been shown to follow a similar trend to that of metal-organic interfaces in which the work function of the metal oxide must be below a critical value.[28, 29] Work functions at, or below this value, cause Fermi level alignment; however, the method through which the interfacial dipole is formed is still yet not fully known. It is likely due to charge transfer from the

HOMO of the organic layer to unoccupied states within the empty s, d or p orbitals of the metal.

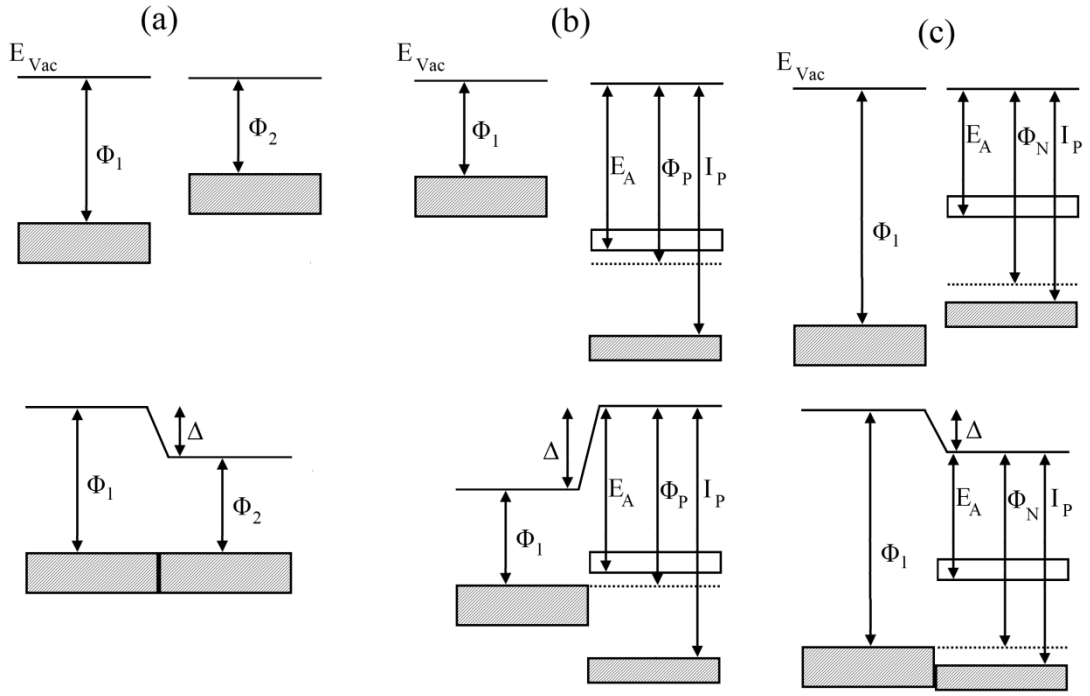

Figure 2.10 Vacuum level alignment and Fermi level alignment for (a) metal-metal (b) metal-organic (LUMO), and (c) metal-organic (HOMO) interfaces. Φ is the work function/Fermi level, Φ_P upper critical Fermi level, Φ_N lower critical Fermi level, E_a electron affinity, I_P ionization potential and Δ interfacial dipole.

Alignment of energy levels is crucial within organic photovoltaic devices to reduce losses that can occur when transferring charge carriers from one material type to another. Differences in the energy levels between the charge transport states of the two materials result in barriers for the extraction of charges.[35-37] These losses manifest itself as an increase within the series resistance of the device. Two forms of contact can be formed at an interface and these are known as Ohmic and Schottky-Mott contacts.

The formation of an Ohmic contact occurs when there is effectively no barrier between the charge transport states, this form of contact occurs for metal-metal contacts, they can also occur in metal-organic and organic-metal oxide contacts.[31, 38] For an Ohmic contact to form at an organic interface, Fermi level alignment must be satisfied; in addition dipoles that occur from possible chemical reactions or permanent dipoles may induce differences in the charge transport state leading to the formation of barriers. If there is a significant barrier for charge transfer between the two materials a Schottky-Mott contact will form, for Vacuum level alignment the formation of a Schottky-Mott contact is highly likely. [38]

Plotting the Substrate work function against the work function of the polymer/substrate interface the alignment conditions can easily be observed. **Figure 2.11** shows such a plot where a 'Mark of Zorro' dependence is observed.[32] For substrate work functions less than Φ_P Fermi alignment with LUMO occurs and the work function of the polymer/substrate interface become pinned to the LUMO. When the work function of the substrate is between these critical values vacuum alignment occurs as Fermi alignment conditions are not satisfied and a metal-insulator-metal behaviour is observed. Once the work function of the substrate goes beyond Φ_N Fermi level alignment occurs and the work function of the polymer/substrate interface become pinned to the HOMO level.

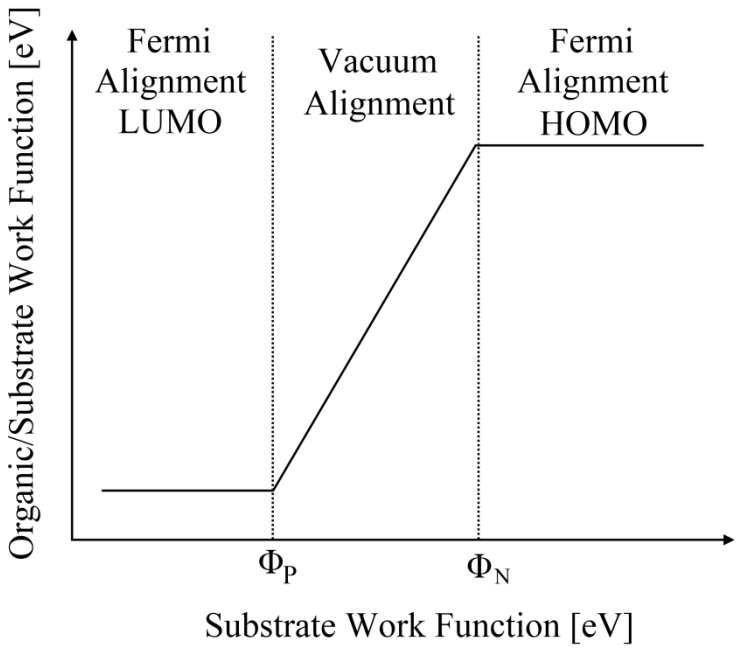

Figure 2.11 A 'mark of Zorro' dependence observed when measuring the substrate work function against the work function of the polymer/substrate interface. This is due to the different alignment conditions observed at the interface.

2.8 References

[1] W. Heisesnberg. Ueber den anschaulichen Inhalt der quantentheoretischen Kinematik and Mechanik. *Zeitschrift für Physik.***43** (1927) 172-198 (Translation from A. Wheeler & H. Zurek. *Quantum Theory and Measurement*. Princeton: Princeton Unviresity; 1983

[2] R. Eisberg & R Resnick. *Quantum Physics of Atoms, Molecules, Solids, Nuclei and Particles*. 2nd Edition. New York: John Wiley and Sons; 1985

[3] H. D. Young & R. A. Freedman. *University Physics*. 9th Edition. Reading: Addison-Wesley; 1996

[4] J. Clayden, N. Greeves, S. Warren & P. Wothers. *Organic Chemistry*. 1st Edition. Oxford: Oxford University Press; 2001

[5] Pauli Exclusion Principle

[6] D. I. Bower. *An Introduction to Polymer Physics*. 1st Edition. Cambridge: Cambridge University Press; 2008

[7] W. Brutting. *Physics of Organic Semiconductors*. 2nd Edition. Weinheim: Wiley-VCH; 2012

[8] V. Coropceanu, J. Cornil, D. A. D. S. Filho, Y. Olivier, R. Silbey & J. L. Bredas. Charge Transport in Organic Semiconductors. *Chemical Reviews*. **107** (2007) 926-952

[9] W. R. Salaneck, R. H. Friend & J. L. Bredas. Electronic Structure of Polymers. *Physical Reports*. **319** (1999) 231-251

[10] A. J. Heeger, S. Kivelson, J. R. Schrieffer & W. P. Su. Solitons in Conducting Polymers. *Reviews of Modern Physics*. **60** (1988) 781-851

[11] N. Tessler, Y. Preezant, N. Rappaport & Y. Roichman. Charge Transport in Disordered Organic Materials and its Relevance to Thin-Film Devices: A Tutorial Review. *Advanced Materials*. **21** (2009) 2741-2761

[12] H. Bassler. Charge Transport in Disordered Organic Photoconductors. *Physica Status Solidi (b)*. **175** (1993) 15-56

[13] A. Miller & E. Abrahams. Impurity Conduction at Low Concentrations. *Physical Review*. **120** (1960) 745-755

[14] N. F. Mott & W. D. Twose. The Theory of Impurity Conduction. *Advances in Physics*. **10** (1961) 107-163

[15] R. J. Kline, M. D. McGehee, E. N. Kadnikova, J. Liu & J. M. J. Frechet. Controlling the Field-Effect Mobility of Regioregular Polythiophene by Changing the Molecular Weight. *Advanced Materials*. **15** (2003) 1519-1522

[16] H. Yan, Z. Chen, Y. Zheng, C. Newman, J. R. Quinn, F. Dotz, M. Kastler & A. Facchetti. A High-Mobility Electron-Transporting Polymer for Printed Transistors. *Nature*. **457** (2009) 679-686

[17] W. Ma, C. Yang, X. Gong, K. Lee & A. J. Heeger. Thermally Stable, Efficient Polymer Solar Cells with Nanoscale Control of the Interpenetrating Network Morphology. *Advanced Functional Materials*. **15** (2005) 1617-1622

[18] Y. K. Lan & C. I. Huang. A Theoretical Study of the Charge Transfer Behaviour of the Highly Regioregular Poly-3-Hexylthiophene in the Ordered State. *Journal of Physical Chemistry B*. **112** (2008) 14857-14862

[19] S. S. Sun & N. S. Saricftci. *Organic Photovoltaic Mechanisms, Materials and Devices*. 1st Edition. Boca Raton: CRC Press; 2005

[20] J. L. Bredas, D. Beljonne, V. Coropceanu & J. Cornil. Charge Transfer and

Energy-Transfer Processes in Pi-Conjugated Oligomers and Polymers: A Molecular Picture. *Chemical Reviews*. **104** (2004) 4971-5003

[21] M. C. Scharber, D. Muhlbacher, M. Koppe, P. Denk, C. Waladauf, A. J. Heeger & C. J. Brabec. Design Rules for Donors in Bulk Heterojunction Solar Cells - Towards 10% Energy-Conversion Efficiency. *Advanced Materials*. **18** (2006) 789-794

[22] B. Kippelen & J. L. Bredas. Organic Photovoltaics. *Energy and Environmental Science*. **2** (2009) 251-261

[23] H. Ohkita, S. Cook, Y. Astuti, W. Duffy, S. Tierney, W. Zhang, M. Heeney, I. McCulloch, J. Nelson, D. D. C. Bradley & J. R. Durrant. Charge Carrier Formation in Polythiophene/Fullerene Blend Films Studied by Transient Absorption Spectroscopy. *Journal of the American Chemical Society*. **130** (2008) 3030-3042

[24] G. Dennler, M. C. Schraber & C. J. Brabec. Polymer-Fullerene Bulk-Heterojunction Solar Cells," *Advanced Materials*. *Advanced Materials*. **21** (2009) 1321-1338

[25] G. Yu, J. Gao, C. Hummelen, F. Wudl & A. J. Heeger. Polymer Photovoltaic Cells: Enhanced Efficiencies via a Network of Internal Donor-Acceptor Heterojunctions. *Science*. **270** (1995) 1789-1791

[26] P. Atkins & J. D. Paula. *Physical Chemistry*. 8th Edition. Oxford: Oxford University Press; 2006

[27] P. Atkins, T. Overton, J. Rourke, M. Weller & F. Armstrong. *Shriver & Atkins Inorganic Chemistry*. 4th Edition. Oxford: Oxford University Press; 2006

[28] L. Ley, Y. Smets, C. I. Pakes & J. Ristein. Calculating the Universal Energy

Level Alignment of Organic Molecules on Metal Oxides. *Advanced Functional Materials*. **23** (2013) 794-805

[29] M. T. Greiner, M. G. Helander, W. M. Tang, Z. B. Wang, J. Qiu & Z. H. Lu. Universal Energy Level Alignment of Molecules on Metal Oxides. *Nature Materials*. **11** (2012) 76-81

[30] H. Ishii. K. Sugiyama, E. Ito & K. Seki. Energy Level Alignment and Interfacial Electronic Structures at Organic/Metal and Organic/Organic Interfaces. *Advanced Materials*. **11** (1999) 605-625

[31] M. N. Rudden & J. Wilson. *Elements of Solid State Physics*. 2nd Edition. Chicester: John Wiley and Sons; 1999

[32] S. Braun, W. R. Salaneck & M. Fahlman. Energy-Level Alignment at Organic/Metal and Organic/Organic Interfaces. *Advanced Materials*. **21** (2009) 1450-1472

[33] H. Ishii & K. Seki. Energy Level Alignment at Organic/Metal Interfaces Studied by UV Photoemission: Breakdown of Traditional Assumptions of a Common Vacuum Level at the Interfaces. *IEEE Transactions on Electronic Devices*. **44** (1997) 1295-1301

[34] W. R. Salaneck, M. Logdlund, M. Fahlman, G. Greczynski & T. Kugler. The Electronic Properties of Polymer-Metal Interfaces Studied by Ultraviolet Photoelectron Spectroscopy. *Materials Science and Engineering: R: Reports*. **34** (2001) 121-146

[35] C. S. Solanki. *Solar Photovoltaics: Fundamentals, Technologies and Applications*.2nd Edition. Delhi: PHI Learning; 2011

[36] V. D. Mihailetchi, P. W. M. Blom, J. C. Hummelen & M. T. Rispens. Cathode

Dependence on the Open-Circuit Voltage of Polymer:Fullerene Bulk Heterojunction Solar Cells. *Journal of Applied Physics*. **94** (2003) 6849-6854

[37] D. Rauh, A. Wagenpfahl, C. Deibel & V. Dyakonov. Relation of Open-Circuit Voltage to Charge Carrier Density in Organic Bulk Heterojunction Solar Cells. *Applied Physics Letters*. **98** (2011) 133301

[38] Y. Shen, A. R. Hosseini, M. H. Wong & G. G. Malliaras. How to Make Ohmic Contacts in Organic Semiconductors. *ChemPhysChem*. **5** (2004) 16-25

Chapter 3

Device Fabrication and Measurement

3.1 Introduction

Organic electronic devices have the advantage of using materials that have a large variety of different processing methods that are capable of depositing thin films. [1] The ability to process from solution is one of the defining points behind the ease of processing of organic electronics. Deposition from solution allows for the possibility of large scale printing via roll-to-roll processing. However, within laboratory based devices that obtain the highest performance, many of the layers still have to be deposited through vacuum based deposition techniques that are difficult and costly to incorporate into roll-to-roll processing setups.[2,3] Throughout the experimental chapters both solution based deposition techniques and vacuum processing techniques are used with **Chapter 6** and **Chapter 7** focusing largely on transitioning from the vacuum deposition of metal oxide layers to the solution processing of these layers. The following chapter discusses the fabrication of organic photovoltaic (OPV) devices along with the various deposition techniques used with the theory of these techniques discussed; information on the materials used is also given. Finally the method for measuring OPV devices is discussed along with the relationship between measured parameters and the physics of devices.

3.2 Device Structure

For all OPV devices fabricated throughout this body of work the standard sandwich architecture is used, this is shown in **Figure 3.1**. It consists of an organic active layer that is placed between two electrodes, the metallic top contact and the Indium Tin Oxide (ITO) coated substrate. Between the electrode and the organic layers charge extraction layers are placed to reduce the potential barriers that exist at these interfaces reducing the losses that can occur. The direction in which these devices are fabricated are the standard direction rather than an inverted device. In the standard architecture holes are extracted at the ITO interface while electrons are extracted at the reflective metallic interface.

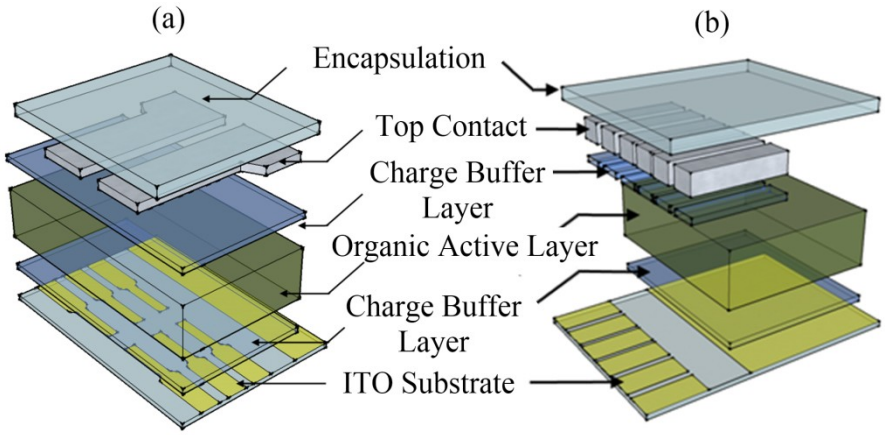

Figure 3.1 An organic electronic device fabricated using a sandwich architecture. (a) shows the device structure with pixels defined by the ITO and (b) shows the device structure with pixels defined by the metallic top contact.

Another important structural consideration in the device is with the active layer, this layer typically consists of two different materials, a donor material and an acceptor material. Due to it consisting of two different materials there is internal structure to this layer, this can either be a bi-layer structure in which the two materials are subsequently deposited one on top of the other or a bulk heterojunction where the two materials are deposited simultaneously in order to form a large interface between the two materials. [4] This large interface allows for the reduction in distances that excitons need to travel in order to reach an interface between the acceptor and donor material and aids in the splitting of excitons increasing the quantum efficiency of the device.[5,6] Within all devices fabricated a bulk heterojunction structure is used as this gives the highest performance for semiconducting polymers due to the short exciton lifetime. [7]

3.3 Device Fabrication

Devices are fabricated on 20mm x 15mm glass substrates coated with 100nm thick pre-patterned layer of fully oxidized ITO purchased from Ossila Ltd. [8] The substrate can either have the ITO patterned such that there are six individual pixel, the dimensions of these pixels are 3mm x 1.5mm (4.5mm^2) acting as the anodes and a single strip of ITO that acts as the cathode as shown in **Figure 3.1**a. Alternatively the metallic cathodes can be used to define the pixel, where the overlapping of the individual metallic top contact and the single ITO square define the pixel size as shown in **Figure 3.1**b. The sizes of the pixels for these substrates are 2mm x 2mm (4mm^2). This alternative substrate design is used to reduce losses associated with the resistance of the ITO layer of the devices.

Initially the substrates are cleaned in order to remove any dust or contaminants that are present on the surface; this is done by sonicating them in various solvents and cleaning agents at high temperatures (typically between 60^{o}C and 70^{o}C). Initially the substrates are sonicated in a 10% concentration NaOH solution for 5 minutes, they are then rinsed in deionised (DI) water. Once rinsed they are then place within a 5% Hellmanex solution and sonicated for a further 5 minutes and then rinsed with DI water again. This is followed by sonicating for 5 more minutes in DI water to remove any Hellmanex that may be present on the substrates, finally they are then transferred to iso-propan-2-ol (IPA) and sonicated for another 5 minutes. Substrates are then removed from the solution and dried using a nitrogen source. In some cases the substrate are transferred to a barrel asher where an oxygen plasma is used to clean and treat the surface of the ITO in order to improve the wettability of solution onto the substrate. After the substrates are dry the deposition of the bottom charge extraction layer can be done.

Deposition of the bottom charge extraction layer has no limitations on the method that can be used due to the robustness of both the glass substrate and the ITO film. Typically the bottom contact buffer layer is either deposited from solution by spin coating or spray coating in air, or is deposited in vacuum by evaporation or sputtering within vacuum deposition systems housed inside a nitrogen filled glovebox. The nitrogen glovebox has a controlled atmosphere such that the moisture and the oxygen levels stay below 0.1ppm. For each individual experiment information on the deposition techniques will be given within the experimental chapters. Discussion on the materials used and the preparation of solution processable bottom contacts will be given in section **3.4. Solution Processed Materials**.

The organic active layer is spin coated within the nitrogen glovebox for all experimental chapters except for **Chapter 7** where the active layer is spray coated within air. Once this layer has been deposited the cathodes are cleaned of any organic material to allow for the deposition of the top contacts into the device while allowing for a direction contact with the ITO used for the cathode. Limitations on the deposition of this layer are set by the wettability of a particular solvent upon the substrate with spray coating being highly sensitive to this property. The preparation technique for organic solutions will be given in **3.4. Solution Processed Materials**.

Deposition of the top contacts in OPV's is severely limited by the underlying organic layer. Sputtering is ruled out as a method for depositing top contacts this is because the energy to dissociate a carbon-carbon bond is much lower than the energy of the sputtering ions.[9-11] For semiconducting polymers this can either cause breaking of polymer chains, or disruption to the structure of the monomer, leading to changes in the electronic properties. [12] In addition the solution processing of top contacts are limited by post deposition processing that may need to be performed. For many solution processed metals and metal oxides high temperatures are required to allow for sintering or oxidation.[13,14] This can either cause the breaking down of the underlying organic material or alterations to the morphology of the donor acceptor blend.[15] Therefore layers deposited after the organic active layer are often done by subsequent vacuum evaporation of the charge extraction layer and the electrode without breaking vacuum.

After deposition of the top contacts the device is complete, in order to stop any further ingress of water and oxygen into the deposited layers the devices are encapsulated. This is done by placing a glass cover slide on top of the deposited layers and sealing it onto the surface using an inert UV setting epoxy. After curing the epoxy

under a UV light for 30 minutes the device are taken out of the glovebox ready to be measured.

3.4. Solution Processed Materials

Solutions are prepared within a clean room environment; the material is weighed out within an amber glass vial that has been blown with a dry nitrogen source to remove any large dust particles, and then cleaned using IPA and the solvent that the material is to be dissolved in. Once weighed out the materials are then transferred to the glovebox where the solvent is added, the material is then dissolved with the aid of a heater and magnetic stir bar. For the organic semiconductors the donor material is dissolved in chlorobenzene on its own at a concentration of $4mg.ml^{-1}$, it is then added to 16mg of dry $PC_{70}BM$ material giving a blend ratio of 1:4 with a total concentration of $20mg.ml^{-1}$. Once the acceptor and donor materials are fully dissolved, the blend is filtered through a 0.45μm Polytetrafluoroethylene (PTFE) filter into a pre-cleaned amber vial. For spray coating the solution is diluted to an overall concentration of $4mg.ml^{-1}$ to obtain the optimum film thickness.

The structures of each of organic semiconductors that are used throughout this thesis are shown in **Figure 3.2** shows PCDTBT, PCDTBT-8 and $PC_{70}BM$, the properties of these organic semiconductors as detailed within literatures are given in detail in **Table 3.1**.

PCDTBT

Poly[[9-(1-octylnonyl)-9H-carbazole-2,7-diyl]
-2,5-thiophenediyl-2,1,3-benzothiadiazole-4,7-diyl-2,5-thiophenediyl]

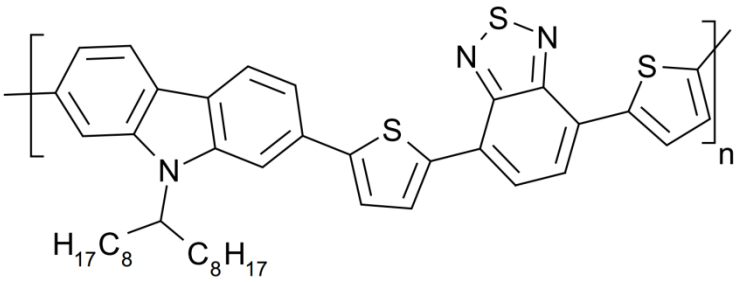

PCDTBT-8

Poly[9-(heptadecan-9-yl)-9H-carbazole-2,7-diyl-alt-
(5,6-bis(octyloxy)-4,7-di(thiophen-2-yl)benzo[c][1,2,5]thiadiazole)-5,5-diyl]

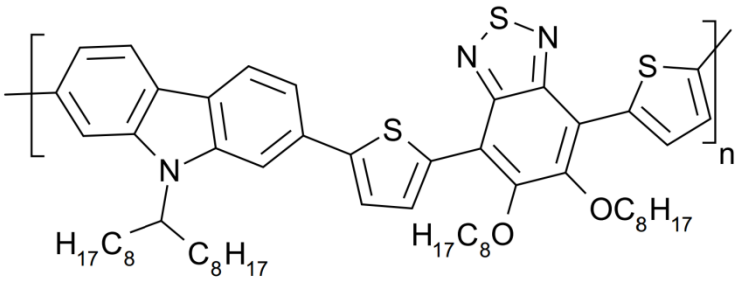

$PC_{70}BM$

[6,6]-Phenyl-C71-butyric acid methyl ester

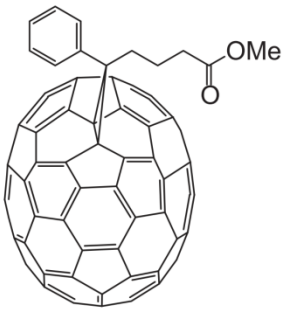

Figure 3.2 The structures of organic semiconducting materials PCDTBT, PCDTBT-8 and $PC_{70}BM$ that are used in OPV's.

	PCDTBT	PCDTBT-8	$PC_{70}BM$
HOMO (eV)	**-5.35** to **-5.5**[16-18]	**-5.40**[16-19]	**-6.1**[20,21]
LUMO (eV)	**-3.42** to **-3.6**[16-18]	**-3.27**[16]	**-4.3**[20,21]
Band Gap (eV)	**1.88** to **1.9**[16-18]	**1.98**[16]	**1.8**[20,21]
Peak Absorption (nm)	**570**[16]	**536**[16]	**N/A**

Table 3.1 Information on the different organic semiconducting materials that are used throughout the experimental chapters that have been taken from literature.

Preparation of PEDOT:PSS is done from a premade water based dispersion purchased at a weight volume of 6% through Ossila Ltd. PEDOT:PSS. The dispersion is filtered through a 0.45μm Polyvinylidene fluoride (PVDF) filter into a pre-cleaned vial. Vanadium (V) Isopropoxide is prepared by diluting the liquid with IPA to its desired concentration the solution is then filtered through a 0.45μm PTFE filter into a pre-cleaned vial. Ammonium molybdate tetrahydrate is prepared by dissolving within water to its desired concentration; the solution is then filtered through a 0.45μm PVDF filter into a pre-cleaned vial. The solution is then mixed with the organic solvent acetonitrile at a ratio of 1:1.5 water: acetonitrile to decrease the viscosity and aid in wettability.

3.5 Spin Coating

Spin coating has the advantage of being able to deposit extremely flat films with thicknesses that can be finely controlled by the spin speed; However, there are several disadvantages that come with spin coating, including only being able to deposit onto

one substrate at a time; and the thickness of the films does not remain constant over distance, making coating large areas difficult.[22] In spin coating the substrates are held in place on a chuck using a vacuum, they are then accelerated to the desired rotational velocity and solution is dispensed onto the surface by a micropipette. Centrifugal force causes the material to move outwards from the axis of rotation spreading the material over the entire surface, the thickness of the material that remains depends upon the rotational velocity and the viscosity of the fluid. While this happens the solvent will evaporate eventually leaving the solute on the surface of the substrate, the rate of evaporation can cause issues with uniformity of the film over large areas due to increasing concentration and hence viscosity leading to thicker films.[22] In order to reduce the chances of none uniformity of the film higher boiling point solvents are desired, however with a higher boiling point the film will take a longer time to dry.[23] Consequently spin coating is an extremely wasteful process as most of the solution is flung off the edge of the substrate rather than used to coat the substrate.

3.6 Ultrasonic Spray Coating

Spray coating is a technique designed for coating large areas rapidly while maintaining a uniform film across these large areas. The spray coater that has been used is a Prism ultra-sonic spray coater purchased from Ultrasonic Systems Inc (USI). Ultrasonic spray coating differs from standard spray coating due to the nozzle head from which the solution is dispensed vibrating at a high frequency (~35KHz). This high frequency vibration causes the solution to atomise into small droplets, these fine droplets are then planarized into a thin jet of solution with a wide spray angle by using an air flow.[24]

This fine jet of solution is passed over the substrate in order to coat the surface with a thin layer of solution. Both the height and the speed at which the nozzle head moves can be changed in order to vary the amount of solution that is deposited onto the substrate. Ideally the solution spreads across the surface rather than forming individual droplets, the film then dries evenly across the entire surface leaving behind a thin film of material with the thickness being highly dependent upon the concentration of the dispensed solution. In order for this to occur the solvent must be wettable on the surface and have a low contact angle, if this does not occur the solution will not dry evenly and will congregate into small droplets leaving behind large uncoated areas. **Figure 3.3** shows the schematic of the ultrasonic spray coater.

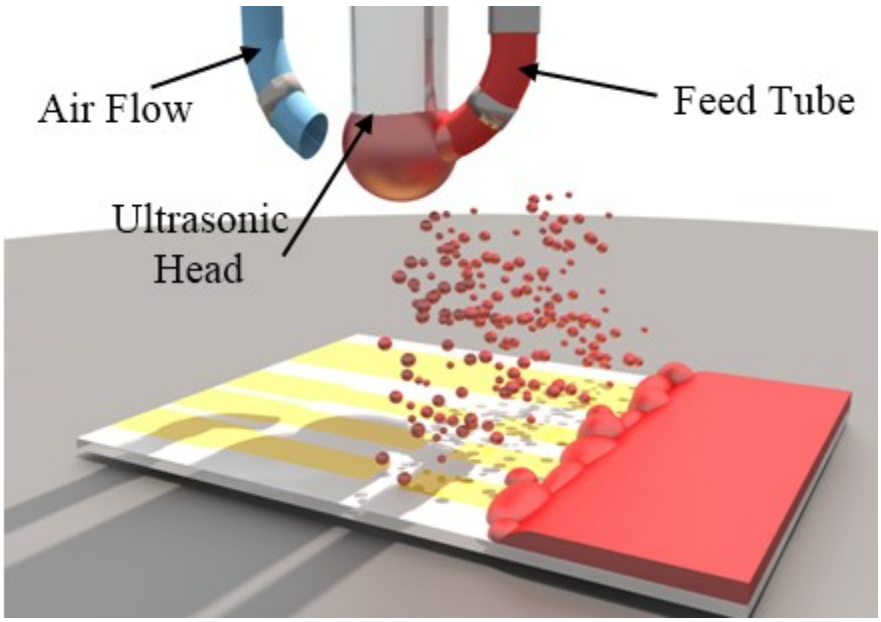

Figure 3.3 Schematics of the ultrasonic spray coating setup, a substrate holder and hot plate are used in order to be able to replicate the position of the samples and the temperatures

Choosing a solvent is a compromise between solubility, boiling point, vapour pressure and surface tension and viscosity.[24-27] Solubility and wetting can be controlled together by using a blend of miscible solvents. Typically one of these solvents will be able to dissolve a large amount of the solute while the other will be a solvent that is known to wet the surface of the substrate well. Examples of such a solvent system are seen in **Chapter 7** where a mixture of water and acetonitrile are used to spray coat ammonium molybdate tetrahydrate. An alternative way to control wetting is by modifying the surface energy of the substrate this is done either through cleaning with different solvents or via the use of oxygen plasma treatment of the surface of the substrate.

3.7 Vacuum Evaporation

Vacuum based deposition is reserved for layers that cannot be solution processed; these are typically the metals or metal oxides used for the top contact. All the chambers that are used have multiple sources available so can do subsequent evaporations without exposing the deposited layers to atmospheric conditions. In addition the vacuum deposition systems are housed within nitrogen filled glove boxes to allow for subsequent encapsulation or storage without further exposing the samples or devices to air. In vacuum deposition the samples are loaded into a chamber using a stainless steel evaporation mask that allows for deposition of material over a desired area of the substrate. The chamber is then pumped down to a low base pressure typically in the region of 10^{-7}mbar to 10^{-6}mbar in order to remove as much trace gasses that could react with the deposited layers or source material as possible. The source material that is

being used for deposition is then gradually heated by passing current through a resistive tungsten coil; the material is allowed to evaporate for a period of time behind a shutter that stops deposition of material onto the substrates. This is done in order to evaporate any contaminants that are present on the surface of the source material so as to not contaminate the devices or substrates. Just before deposition the substrates are set to rotate and then the shutter is opened, this rotation allows for an even coverage across the surface of the substrates. Deposition rate and thickness are both monitored using a quartz crystal gauge set up that has been calibrated for each of the different source positions. The deposition rate for Aluminium is kept at around $1Å.s^{-1}$ while the deposition rates for Calcium and Molybdenum Oxide are kept between $0.1Å.s^{-1}$ and $0.3Å.s^{-1}$. During deposition the maximum pressure the system is allowed to reach is $1x10^{-5}$mbar, if the system exceeds this pressure the deposition shutter is closed and the pressure is allowed to reduce by lowering the temperature of the source material. Before the chamber is opened and substrates removed the entire setup is allowed to cool down for 5 to 10 minutes. The temperature of the substrate at any point during the deposition procedure is below $80^{o}C$ as estimated using temperature sensitive stickers.

3.8 Sputter Deposition

Sputter deposition is a plasma assisted deposition technique that uses high energy ions that are accelerated towards a target material in order to ablate atoms, these ablated atoms then become deposited onto any surrounding surface. In this work a reactive magnetron sputtering system with a 13.5MHz radio frequency (R.F) source and impedance matching circuit in order to generate the plasma, this system is housed

within a nitrogen filled glovebox. By using this system, it is possible to sputter from a range of targets including pure metals, metal oxides, semiconducting materials and resistive materials.[28-30] Substrates are loaded into the vacuum chamber at a fixed distance of 150mm from the deposition target and the chamber is then pumped down to a base pressure of approximately 10^{-6}mbar. Argon is introduced as an inert sputtering gas, the rate at which Argon is bled into the chamber is varied using an Edwards mass flow controller between 0 and 10sccm. In addition, Oxygen is bled into the chamber at a rate between 0 and 10sccm. The overall flow rate into the chamber is kept fixed at 10sccm; the pressure of the chamber reaches a maximum value of between $1x10^{-2}$mbar and $2x10^{-2}$mbar.

Figure 3.4 shows a simplified schematic of the sputter target, a plasma is formed by applying a large bias between the surface of the target and the chamber walls /target shield. The formation of a plasma is described as a glow discharge, where at low electric fields a current flows through the gas. Upon increasing the potential between the anode and cathode the free electrons that are present gain sufficient enough energy to ionize gas molecules within the chamber. Once the plasma is struck ionized gas is accelerated towards the target and hits the surface, through the transfer of momentum from the impinging ion and the target material is ablated from the surface. During this process electrons are also emitted from the targets surface, these can recombine with the ions to give the characteristic 'glow' of the discharge or can go on to produce further ionisation. Once ionization due to electrons emitted from the surface begins a self sustaining plasma can be formed and sputter deposition can be said to begin.[31, 32]

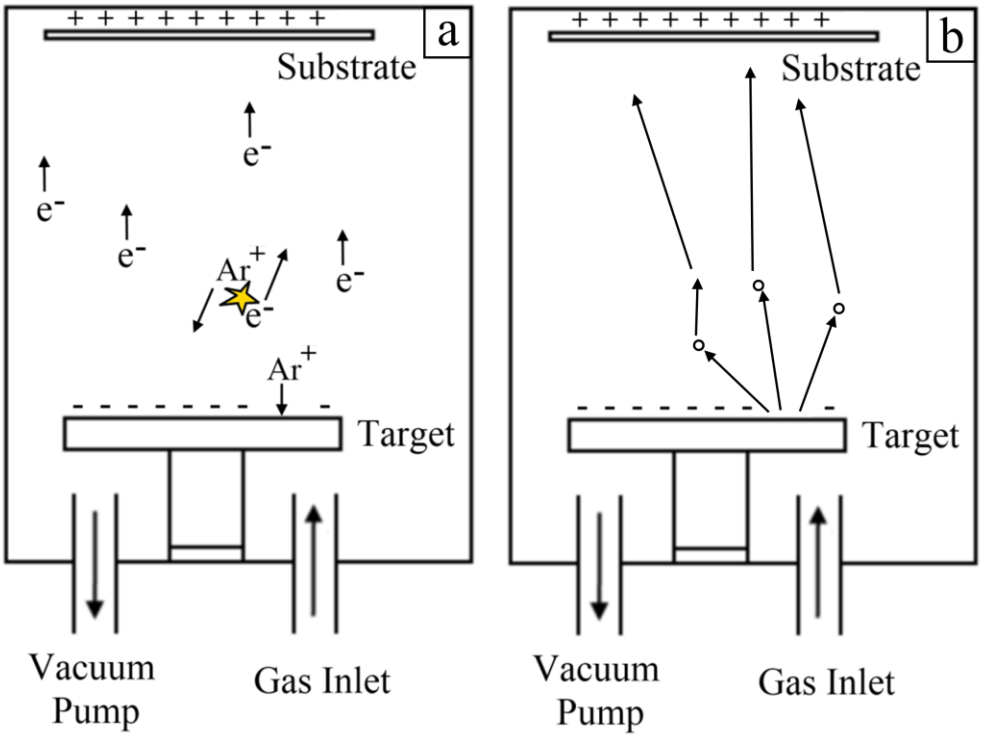

Figure 3.4 A simplified diagram of the sputtering setup and the process of sputtering. (a) shows the ionization of argon gas and the acceleration towards the target, (b) shows the sputtering of material upon impact of the ion and scattering of sputtered material.

For magnetron sputtering in addition to the setup described a strong magnet is placed underneath the target this is to aid in the generation of ions within the chamber. This is done by increasing the path length that the electrons have to travel once emitted from the target's surface. For lower energy electrons they become trapped by the magnetic field in a close loop near the target's surface; in addition, higher energy electrons are deflected reducing the chance of bombardment of the substrate. Trapped electrons help to generate a dense plasma for the low pressure of gas that is within the deposition system allowing for higher sputtering yields.[33, 34]

In reactive sputtering with oxygen the reactive gas causes the target to become oxidized and the target begins to be covered with an insulating material. As more oxygen is added to the chamber or deposition occurs for longer the surface coverage of the oxide increases diffuses into the target causing a thicker insulating layer.[33] This insulating layer reduces the rate that electrons get replenished at the surface of the target reducing the bias at the surface and the amount of electrons available for further ionization. A combination of the reduced amount of electrons and bias cause the amount of gas being ionized to drop and eventually the plasma cannot be sustained and will die. In order to overcome this, R.F biases are used rather than constant fixed bias, by having a rapidly oscillating alternating bias the electrons that are emitted from the surface do not get a chance to accelerate far from the surface of the target before the polarity of the bias is switched. This reversing of polarity of the applied bias causes electrons to become trapped close to the surface of the target leading to a very dense plasma close to the surface allowing for sputtering of insulating targets.[29] When operating using an R.F bias the impedance of the source needs to match the impedance of the sputter system this is due to the possibility of reflections of the transmitted power when it is coupled into a load. When reflections occur the amount of power that is delivered to the plasma can vary, furthermore the reflected power can cause an overload on transmission lines and in the power source. In the sputtering setup an impedance matching system is used in order to correctly match the source impedance to the sputtering system impedance in order to remove any reflected power losses.

With sputtering there are several different parameters that can be varied in order to obtain films with desired properties. Among these the main processing parameters are the overall pressure, the partial pressure of reactive gasses, the power coupled into the

plasma and the distance between the target and the substrate. In **Chapter 8** the overall pressure, partial pressure of reactive gasses and power coupled into the plasma are varied. Changes in the power coupled into the plasma is done by increasing the bias applied to the target, with a stronger electric field the energy gained by ions accelerated towards the targets surface increases. Ions that impact upon the surface with higher energy will cause more material to be ablated from the surface and for the kinetic energy of the emitted material to be higher. Overall pressure in a sputtering system has multiple effects on the deposition process. By increasing the amount of gas within the chamber the probability of an ionisation event occurring rises, with more ions present the amount of material that is ablated from the surface rises too. This causes an increase in the deposition rate; however, this with more gas in the chamber this increase is offset by scattering of the ablated material due to collisions with the gas present. The highest deposition rate achievable is therefore determined by a trade-off between the increase in the amount of material ablated and the amount of scattering that occurs.

Partial pressure of the different gasses is important with regards to the introduction of reactive gasses into the sputtering chamber. With the introduction of oxygen the surface layer of the target begins to oxidise and become insulating. With a mixture of an inert sputtering gas and reactive gas two processes occur simultaneously, the first is the reaction of oxygen with the surface and the second is the ablation of the surface by ions. At low partial pressures the ablation rate will exceed the oxidation rate of the surface. The deposited layer will therefore be a mixture of oxidised and metallic materials. As the partial pressure of the reactive gas increases with respect to the inert gas the rate of oxidation of the surface will increase until it exceeds the ablation rate. The amount of reactive gas needed for this to occur will depend upon the material being

ablated with easily oxidised materials requiring a low partial pressure of oxygen for rapid oxidation of the surface to occur. Over time, the oxide layer will increase in thickness as oxygen diffuses into the target, with further increased partial pressure of the reactive gas the rate at which the oxide layer grows will increase. This process is called target poisoning, when the reactive gas is removed from the chamber a poisoned target will not immediately return to depositing metal instead a layer of oxide will have to be removed. Due to the low deposition rates of oxidised targets the removal of the oxide layer can take a considerable amount of time.

3.9 Measurement of Organic Photovoltaic Devices

With organic photovoltaic devices the characterisation of performance is done by measuring the devices ability to convert energy in sunlight directly to electric power. This is called the power conversion efficiency (PCE) of a solar cell and is the product of the absorption, recombination mechanisms and resistive losses that occur within a device. By reducing the recombination of charge carriers and resistive losses, and increasing the amount of light that is absorbed the efficiency can be increased. The PCE is characterised by taking current-voltage (I-V) measurements of a device under constant illumination from a solar simulator. The emission of the solar simulator is designed to match the irradiance of the sun across the near ultraviolet, visible and infrared wavelength. The emitted spectra matches the spectral response after it has passed through a given length of atmosphere this distance is known as the air mass coefficient. An AM1.5 standard is used for all measurements; this matches the suns spectrum after passing through 1.5 earth atmospheres. The solar simulator used is a

Newport 92251A-1000 with a constant irradiance of 100mW.cm^{-2} **Figure 3.5** shows an AM1.5 spectrum.

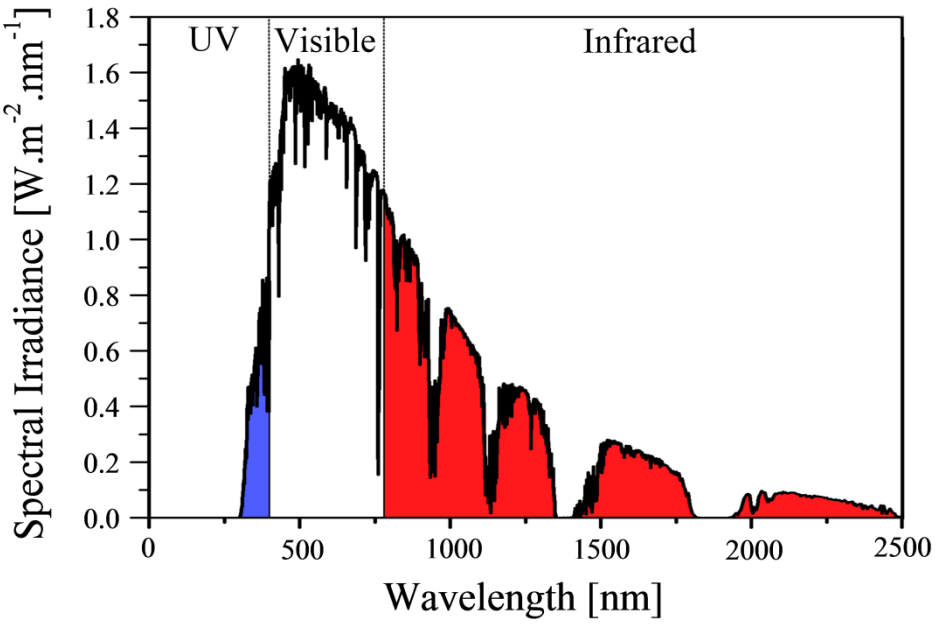

Figure 3.5 AM1.5 spectra showing the ultraviolet, visible and infrared regions of the solar spectrum.

While under constant illumination I-V sweeps are taken of the device, the current voltage response for an organic photovoltaic device is that of a diode. The Shockley diode equation is given in **Equation 3.1** this equation is for an ideal photodiode. Where J_0 is the dark saturation current density of the device, K is Boltzmann's constant, T the temperature and J_{sc} is the short circuit current. The first term is related to the diode like response while the short circuit current is due to the harvesting of light within the

photodiode. **Equation 3.2** shows the modified Shockley photodiode equation where the losses within the device architecture are taken into account. The additional terms in this equation are the series resistance R_s, the shunt resistance R_{sh} and the ideality factor n. R_s arise from losses from transport through resistive layers, and losses at interfaces due to extraction barriers while R_{sh} is due to defects within the device that allows for alternate paths for photo-generated current to leave the cell. The ideality factor describes the different recombination mechanics that can occur within the device, for an ideal diode the ideality factor is set as 1 while in an organic photovoltaic device this ranges between 1.5 and 2 depending upon the materials used.[35] Information on the various forms of recombination that can occur within an organic photovoltaic device is given in **Chapter 2.5**.

$$J(V) = J_0\left[\exp\left(\frac{eV}{KT}\right) - 1\right] - J_{sc} \qquad \textbf{Equation 3.1}$$

$$J(V) = J_0\left[\exp\left(\frac{e(V - JR_s)}{nKT}\right) - 1\right] + \frac{V - JR_s}{R_{sh}} - J_{sc} \qquad \textbf{Equation 3.2}$$

When measuring the devices the current is converted to current density to normalise the performance to the size of the solar cells active area resulting in a current density-voltage (J-V) plot. **Figure 3.6** shows a typical J-V curve for a device under illumination. The parameters that can be extracted from the graph are the open circuit voltage V_{oc}, short circuit current density J_{sc}, maximum power point voltage V_{mpp} and maximum power point current density J_{mpp}. The V_{oc} is the voltage required to reduce the current

generated by the solar cell to zero, J_{sc} is the amount of current generated by the solar cell with zero applied voltage. J_{mpp} and V_{mpp} are the current density and voltage for the maximum power output of the device. The shunt resistance is proportional to the gradient of the line in the negative bias negative current region of the curve and the shunt resistance is proportional to the inverse of the gradient of the line in the positive current positive bias region of the curve.

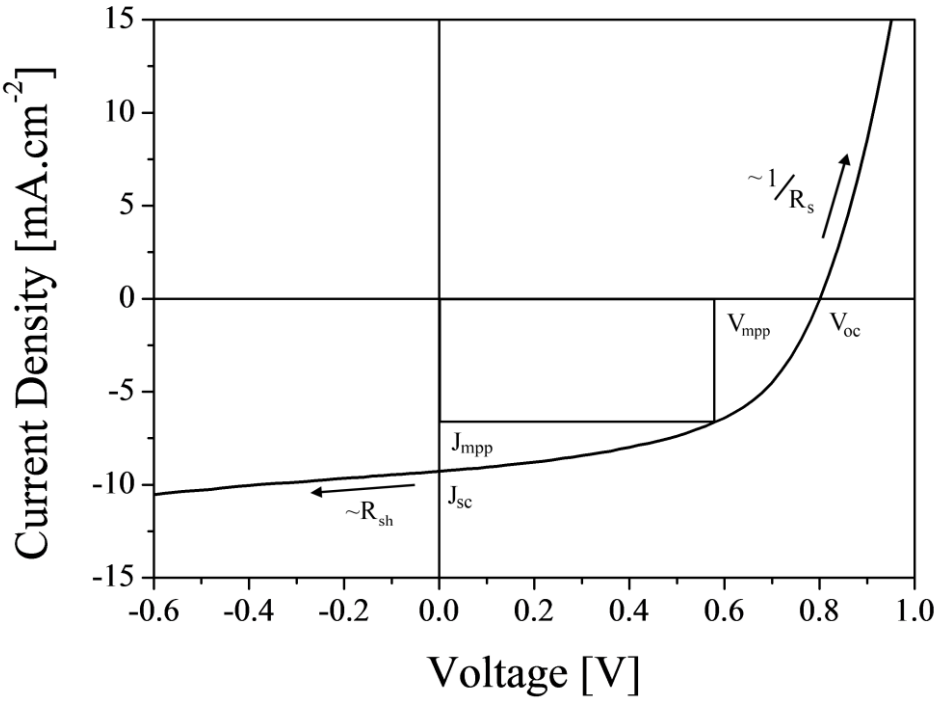

Figure 3.6 Current density-voltage characteristics for an organic solar cell showing parameters V_{oc}, J_{sc}, V_{mpp} and J_{mpp} that can be measured.

Equation 3.3 shows how the efficiency of the device can be calculated using these parameters, the fill factor *FF* is shown in **Equation 3.4** and is the ratio of the products

of V_{mpp} and J_{mpp}, and V_{oc} and J_{sc}. These parameters are closely linked to the materials and the structure of the organic photovoltaic device. The theoretical maximum V_{oc} of the device is determined by the acceptor strength of a material, this is the difference between the HOMO of the donor and the LUMO of the acceptor material.[36, 37] In addition disorder as described in **Chapter 2.3** within organic materials leads to the HOMO and LUMO levels having a Gaussian spread in the energy states. This spread means that charge carriers generated by photo excitation are not at the centre of the Gaussian distribution.[38, 39] Another factor that can reduce the V_{oc} is recombination of charge carriers, increased recombination leads to an increase in the dark saturation current. This increase in the dark saturation current increases the amount of current contributed from the diode response of the Shockley photodiode equation.[40] A final factor that influences the V_{oc} is the contact at the electrodes of a device, as mentioned in **Chapter 2.7** two major types of contact can be formed these are Ohmic and Schottky-Mott contacts. In Schottky-Mott contacts the open circuit voltage will no longer depend on the difference on the acceptor strength but on the difference in work function of the metallic contacts as seen in metal-insulator-metal devices.[38,41] In addition the presence of barriers for charge transfer at the interfaces will lead to losses in the V_{oc} due to the need to overcome these internal barriers.

J_{sc} is the maximum current that can be drawn from a solar cell under illumination; therefore it is dependent upon several factors. These include the total amount of light that is absorbed, which in turn is related to the band gap of the absorbing material. With a lower band gap, more excitons are generated due to a larger amount of photons with energy greater than the band gap; however, reduction in the bandgap leads to a reduction in V_{oc}; therefore in a single junction device there is a limit

to how low the bandgap can be. J_{sc} is also dependent upon losses that occur within a device; these include recombination of charge carriers that lead to an increase in the dark saturation current that opposes photogenerated current. In addition both high series resistance and low shunt resistance lead to reduction in the maximum obtainable J_{sc}.

The Fill Factor depends upon several properties of a device; however the simplest way of describing the Fill Factor is how well a device behaves like an ideal diode. Therefore the factors that lead to a reduction in the Fill Factor are low shunt resistance, high series resistance, and ideality factors that are greater than 1. In order to increase the overall performance of a device there are a few crucial things that need to be improved upon these are reduction in combination, reduction in the current that can pass through device shorts and losses due to series resistance. With metal oxides the most important factor is the reduction in the series resistance due to contact resistances at the interfaces between the organic semiconducting materials and the electrodes.

$$PCE = \frac{V_{oc}J_{sc}FF}{P_{in}} \qquad \textbf{Equation 3.3}$$

$$FF = \frac{V_{mpp}J_{mpp}}{V_{oc}J_{sc}} \qquad \textbf{Equation 3.4}$$

3.10 References

[1] C. J. Brabec, U. Scherf, V. Dyakanov. *Organic Photovoltaics: Materials, Device Physics, and Manufacturing*. 1st .Weinheim: Wiley-VCH; 2008

[2] Heliatek Consolidates its Technology Leadership by Establishing Worl Record for Organic Solar Technology With a Cell Efficiency of 12%. [online] http://www.heliatek.com/newscenter/latest_news/neuer-weltrekord-fur-organische-solarzellen-heliatek-behauptet-sich-mit-12-zelleffizienz-als-technologiefuhrer/?lang=en#.

[3] Z. He, C. Zhong, S. Su, M. Xu, H. Wu & Y. Cao. Enhanced Power Conversion Efficiencys in Organic Solar Cells Using an Inverted Architecture. *Nature Photonics*. **6** (2012) 591-595

[4] G. Yu, J. Gao, J. C. Hummelen, F. Wudl & A. J. Heeger. Polymer Photovoltaic Cells: Enhanced Efficiencies Via a Network of Internal Donor-Acceptor Heterojunctions. *Science*. **270** (1995) 1789-1791

[5] P. Peumans, A. Yakimov & S. R. Forrest. Small Molecular Weight Organic Thin-Film Solar Cells. *Journal of Applied Physics*. **93** (2003) 3693-3723

[6] N. S. Sariciftci, D. Braun, V. I. Srdanov, A. J. Heeger, G. Stucky & F. Wudl. Semiconducting Polymer Buckminsterfullerene Heterojunctions: Diodes, Photodiodes, and Photovoltaic Cells. *Applied Physics Letters*. **62** (1993) 585-587

[7] B. Kippelen & J. L. Bredas. Organic Photovoltaics. *Energy and Environmental Science*. **2** (2009) 251-261

[8] Ossila – Organic Photovoltaics, OLEDs, PLEDs & OFETs. [online] http://www.ossila.com/

[9] D. R. Lide. *Handbook of Chemistry and Physics*. 79th edition. Boca Raton: CRC Press; 1998

[10] N. Laegreid & G. K. Wehner. Sputtering Yields of Metals for Ar+ and Ne+ Ions With Energied From 50 to 600eV. *Journal of Applied Physics*. **32** (1961) 365-369

[11] R. V. Stuart & G. K. Wehner. Sputtering Yields at Very Low Bombarding Energies. *Journal of Applied Physics.* **33** (1962) 2345-2352

[12] J. Meyer, S. Hamwi, M. Kroger, W. Kowalsky, T. Riedl & A. Kahn. Transition Metal Oxides for Organic Electronics: Energetics, Device Physics & Applications. *Advnaced Materials*. **24** (2012) 5408-5427

[13] A. K. K. Kyaw, X. W. Sun, C. Y. Jiang, G. Q. Lo, D. W. Zhao & D. L. Kwong. An Inverted Organic Solar Cell Employing a Sol-Gel Derived ZnO Electron Selective Layer and Thermal Evaporated MoO3 Hole Selective Layer. *Applied Physics Letters*. **93** (2008) 221107

[14] H. Oh, J. Krantz, I. Litzov, T. Stubah, L. Pinna & C. J. Brabec. Comparison of Various Sol-Gel Derived Metal Oxide Layers for Inverted Organic Solar Cells. *Solar Energy Materials and Solar Cells*. **95** (2011) 2194-2199

[15] T. Wang. A. J. Pearson, A. D. F. Dunbar, P. A. Staniec, D. C. Watters, H. Yi, A. J. Ryan, R. A. L. Jones, A. Iraqi & D. G. Lidzey. Correlating Structure With Function in Thermally Annealed PCDTBT:PC70BM Photovoltaic Blends. *Advanced Functional Materials*. **22** (2012) 1399-1408

[16] A. A. B. Alghamdi, D. C. Watters, H. Yi, S. Al-Faifi, M. S. Almeataq, D. Coles, J. Kingsley, D. G. Lidzey & A. Iraqi. Selonophene Vs Thiophene in Benzothiadiazole Based Low Energy Gap Donor-Acceptor Polymers for Photovoltaic Applications. *Journal of Material Chemistry*. **1** (2013) 5165-5171

[17] N. Blouin, A. Michaud, D. Gendron, S. Wakim, E. Blair, R. Neagu-Plesu, M. Belletete, G. Durocher, Y. Tao & M. Leclerc. Towards a Rational Design of Poly(2,7-Carbazole) Derivatives for Solar Cells. *Journal of the American Chemical Society*. **130** (2008) 732-742

[18] N. Blouin, A. Michaud & M. Leclerc. A Low-Bandgap Poly (2,7-Carbazole) Derivative for Use in High-Performance Solar Cells. *Advanced Materials*. **19** (2007) 2295-2300

[19] J. Griffin, D. C. Watters, H. Yi, A. Iraqi, D. G. Lidzey & A. R. Buckley. The Influence of MoOx Anode Stoicheometry on the Performance of Bulk Heterojunction Polymer Solar Cells. *Advnaced Energy Materials*. DOI: 10.1002/aenm.201200886

[20] Y. Sun, C. J. Takacs, S. R. Cowan, J. H. Seo, X. Gong, A. Roy & A. J. Heeger. Efficient Air-Stable Bulk Heterojunction Polymer Solar Cells Using MoOx as the Anode Interfacial Layer. **23** (2011) 2226-2230

[21] Y. He & Y. Li. Fullerene Derivative Acceptors for High Performance Polymer Solar Cells. *Physical Chemisty Chemical Physics*. **13** (2011) 1970-1983

[22] W. W. Flack, D. S. Soong, A. T. Bell & D. W. Hess. A Mathematical Model for Spin Coating of Polymer Resists. *Journal of Applied Phsics*. **56** (1984) 1199-1206

[23] K. Norrman, A. Ghanbari-Siahkali & N. B. Larsen. 6 Studies of Spin-Coated Polymer Films. *Annual Reports Section "C" (Physical Chemistry)*. **101** (2005) 174-201

[24] K. X. Steirer, M. O. Reese, B. L. Rupert, N. Kopidakis, D. C. Olson, R. T. Collins & D. S Ginley. Ultasonic Spray Deposition for Production of Organic

Solar Cells. *Solar Energy Materials and Solar Cells*. **93** (2009) 447-453

[25] C. N. Hoth, S. A. Choulis, P. Schilinsky & C. J. Brabec. High Photovoltaic Performance of Inkjet Printed Polymer:Fullerene Blends. *Advanced Materials*. **19** (2007) 3973-3978

[26] S. E. Shaheen, C. J. Brabec, N. S. Sariciftci, F. Padinger, T. Fromherz & J. C. Hummelen. 2.5% Efficient Organic Plastic Solar Cells. *Applied Physics Letters*. **78** (2001) 841-843

[27] R. Green, A. Morfa, A. J. Ferguson, N. Kopidakis. G. Rumbles & S. E. Shaheen. *Applied Physics Letters*. **92** (2008) 033301

[28] J. Heller. Reactive Sputtering of Metals in Oxidizing Atmospheres. *Thin Solid Films*. **17** (1973) 163-176

[29] P. D. Davies & L. I. Maissel. Dielectric Thin Films Through RF Sputtering. *Journal of Applied Physics*. **37** (1966) 574-579

[30] T. Minami. Transparent Conducting Oxide Semiconductors for Transparent Electrodes. *Semiconducting Science Technology*. **20** (2005) S35-S44

[31] B. Chapman. *Glow Discharge Processes: Sputtering and Plasma Etching*. 1st edition. New York: Wiley; 1980

[32] R. V. Stuart. *Vacuum Technology, Thin Films and Sputtering: an Introduction*. 1st edition. New York: Academic Press; 1983

[33] P. J. Kelly & R. D. Arnell. Magnetron Sputtering: a Review of Recent Developments and Applications. *Vacuum*. **56** (2000) 159-172

[34] W. D. Sproul, P. J. Rudnik, M. E. Graham & S. L. Rohde. High Rate Reactive Sputtering in an Opposed Cathode Closed-Field Unbalanced Magnetron Sputtering System. *Surface and Coating Technologies*. **43-44** (1990) 270-278

[35] C. J. Brabec. Organic Photovoltaics: Technology and Market. *Solar Energy Material*. **83** (2004) 273-292

[36] C. J. Brabec, A. Cravino, D. Meissner, N. S. Sariciftci, T. Fromherz, M. T. Rispens, L. Sanchez & J. C. Hummelen. Origin of Open Circuit Voltage of Plastic Solar Cells. *Advanced Functional Materials*. **11** (2001) 374-380

[37] K. Vandewal, K. Tvingstedt, A. Gadisa, O. Inganas & J. V. Manca. On the Origin of the Open-Circuit Voltage of Polymer Fullerene Solar Cells. *Nature Materials*. **8** (2009) 904-909

[38] V. D. Mihailetchi. P. W. M. Blom, J. C. Hummelen & M. T. Rispens. Cathode Dependence of the Open-Circuit Voltage of Polymer:Fullerene Bulk Heterojunction Solar Cells. *Journal of Applied Physics*. **94** (2003) 6849-6854

[39] H. Bassler. Charge Transport in Disordered Organic Photoconductors a Monte Carlo Simulation Study. *Physica Status Solidi B.***175** (1993) 15-56

[40] C. S. Solanki. *Solar Photovoltaics: Fundamentals, Technologies and Applications*. 1st edition. New Dehli: Eastern Economy Edition; 2009

[41] D. Rauh, A. Wagenpfahl, C. Deibel & V. Dyakonov. Relation of Open Circuit Voltage to Charge Carrier Density in Organic Bulk Heterojunction Solar Cells. *Applied Physics Letters*. **98** (2011) 133301

[42] V. Dyakonov. Mechanisms of Controlling the Efficiency of Polymer Solar Cells. *Applied Physics A*. **79** (2004) 21-25

Chapter 4

Thin Film Characterisation

4.1 Introduction

The following chapter focuses upon the measurement techniques that are used to study thin films throughout the various experimental chapters. The different techniques used are absorbance spectroscopy, ultraviolet photoelectron spectroscopy, x-ray photoelectron spectroscopy, spectroscopic ellipsometry and atomic force microscopy. Using these measurement techniques it is possible to extract information about the chemical state, electrical properties, optical properties, thickness and surface profile of a thin film. Information on the theory behind these measurement techniques is given and also how to analyse data obtained from them.

4.1. Absorbance Spectroscopy

Absorbance spectroscopy is used to see how the transmission of light through a sample can vary across the spectrum ranging from the near ultraviolet at 250nm across the visible spectrum to 850nm. **Figure 4.1** shows the structure of the Jobin Yvon Horiba Fluoromax-4 that is used throughout this thesis to take absorbance spectra. A Xenon arc lamp is used as the light source with emission starting at 240nm, the light is focused using an elliptical mirror into a Czerny-Turner monochromator. [1] The light entering is focused onto an entrance slit; this slit is used to control the intensity of light. Light is then collimated using a mirror and is then incident upon a blazed diffraction grating, upon diffraction the light is reflected by a second mirror that refocuses the beam onto a secondary slit. The wavelength of light that passes through the secondary slit is dependent upon the angle the blazed grating makes with respect to the second mirror. In addition the width of the secondary slit can be used to vary the resolution of the spectra, with a smaller slit size giving higher resolution. When the light exits the monochromator a reference beam is generated by focusing the light through a beam splitter onto the sample. The reference beam is then measured by a photodiode and is equal to the amount of light incident upon the sample. By measuring the amount of light transmitted through a sample using a second photodiode it is possible to calculate the transmittance of a sample and hence its absorbance.

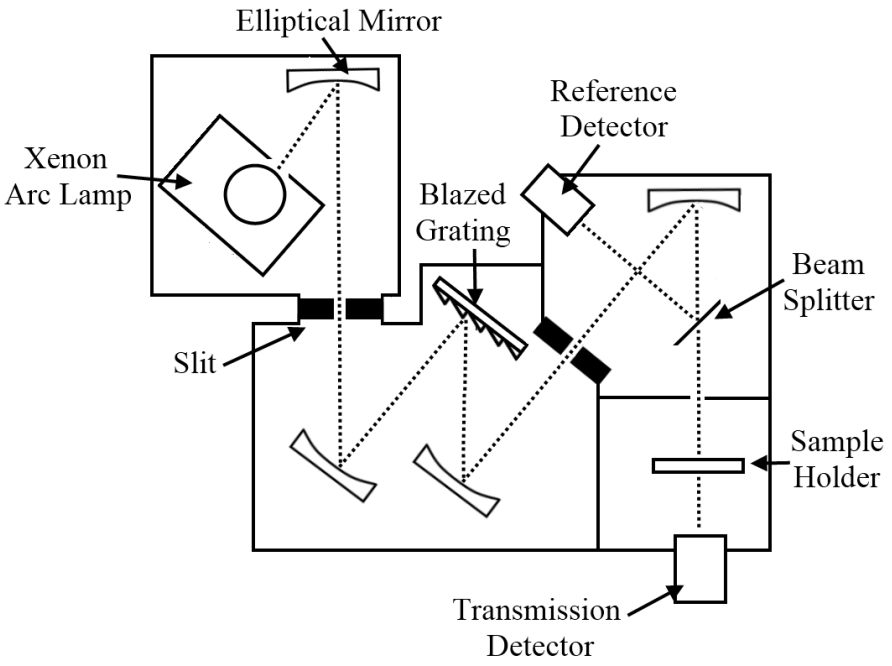

Figure 4.1 A Jobin Yvon Horiba Fluoromax-4 schematic, the instrument is broken up into four separate chambers which are the light source, monochromator, reference beam detection and sample chamber.

The transmittance of a sample is calculated from the Beer-Lambert law given in **Equation 4.1** where T is the fraction of light transmitted through the sample, I is the amount of light transmitted and I_0 is the amount of light incident upon the sample. [2] These values are ratios of the total amount of light present before and after passing through the sample, this includes not just the absorption of light within the sample itself but also dispersion of light and reflections that occur at the interfaces.

$$T(\lambda) = \frac{I(\lambda)}{I_o(\lambda)} \qquad \textbf{Equation 4.1}$$

Transmittance spectra of blank reference slides are taken before measuring a sample in order to determine the losses due to the substrate. Transmittance spectra are most useful for determining absorption peaks of a material and can also be used to determine the complex part of the refractive index (extinction coefficient) of a material. This is shown in **Equation 4.2** however this method of determining the extinction coefficient leads itself to possible errors if scattering or light occurs within the film leading to extinction coefficients that are incorrect. [2]

$$I(\lambda) = I_o(\lambda).e^{-\alpha x} \qquad \textbf{Equation 4.2a}$$

$$k = \frac{\alpha\lambda}{4\pi} \qquad \textbf{Equation 4.2b}$$

4.2. Ultraviolet Photoelectron Spectroscopy

Photoelectron spectroscopy is the study of the energy spectrum of electrons that have been emitted from the surface of a material after it has been illuminated with photons of a specific known energy. By measuring the kinetic energy spectrum of the emitted electrons and by knowing the exact energy of the illuminating photon it is possible to determine the binding energy of electrons within the film through the photoelectric relationship given in **Equation 4.3**. [3]

$$E_{B.E} = h.f - E_{K.E}$$ **Equation 4.3**a

$$E_{B.E} = E_{Photon} - E_{K.E}$$ **Equation 4.3**b

Where $E_{B.E}$ is the binding energy of the electron, h is Planck's constant, f is the frequency of light and $E_{K.E}$ is the kinetic energy of the electron. This can be simplified due to the fact that the product of h and f is the energy of the photon E_{Photon}. In UPS the source of the photons are from a gas discharge, most often the gas used is Helium. The energy of the emitted light is dependent not only upon the type of gas but also the ionization state of a gas, for neutral Helium the emission line is He (I) at 21.2eV or for singly ionized Helium the emission line is He (II) at 40.8eV.[4,5]

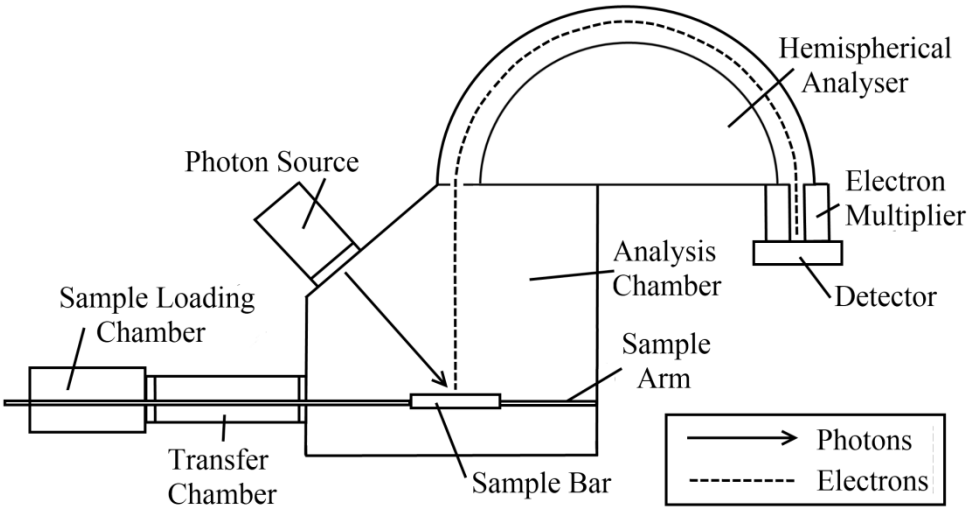

Figure 4.2 Schematic diagram of the Kratos Axis Ultra photoelectron spectroscopy chamber used for XPS and UPS analysis of samples.

Figure 4.2 shows a simplified structure of the Kratos Axis Ultra photoelectron spectroscopy chamber. The photon source, in the case of UPS, is a gas discharge chamber with a window that is highly transparent across the UV region of the spectrum; this is used to separate the analysis chamber from the discharge chamber in order to maintain the ultra-high vacuum required for photoelectron spectroscopy. In addition to the analysis chamber and the gas discharge chamber there are the sample loading chamber and the transfer chamber. These additional chambers are used so that the analysis chamber can be kept at an ultra-high vacuum at all times when introducing samples for analysis. The samples for analysis are transferred through the chambers by the use of a sample bar attached to an arm that can be moved forward and backwards, in addition this arm can also be rotated to allow for angle resolved studies of samples.

In order to measure the spectra of the electrons kinetic energy the emitted electrons need to pass through a hemispherical analyser. The hemispherical analyser takes advantage of the Lorentz force that states that a charged particle passing through a magnetic field will experience a force upon it determined by the cross product of the magnetic field and the product of the charge and velocity of the particle. The equation for the Lorentz force acting upon an electron is given in **Equation 4.4**a where *F* is the force, *e* is the charge of an electron, *v* is the velocity of the electron and *B* is the magnetic field.[5,6]

$$\overline{\boldsymbol{F}} = e\overline{\boldsymbol{v}} \times \overline{\boldsymbol{B}} \qquad \textbf{Equation 4.4}\text{a}$$

$$F = \frac{m_e v^2}{r}$$ **Equation 4.4**b

$$E_{K.E} = \frac{m_e v^2}{2}$$ **Equation 4.4**c

$$\sqrt{E_{K.E}} = \frac{re}{\sqrt{2m_e}} B$$ **Equation 4.4**d

The hemispherical analyser has fixed radius that electrons can pass through in order to enter the electron multiplier. This makes it possible to determine the kinetic energy of an electron that passes through the hemispherical analyser from the applied magnetic field alone. This is done by using the equation for centripetal force given by **Equation 4.4**b where m_e is the mass of an electron and r is the radius of circle the electron will travel through; and also the kinetic energy equation given by **Equation 4.4**c where $E_{K.E}$ is the kinetic energy. **Equation 4.4**d then gives the final equation that relates the kinetic energy of an emitted electron to the magnetic field applied within the hemispherical analyser. Once the electrons at a particular kinetic energy pass through the analyser the signal is amplified by an electron multiplier tube and these electrons are then measured by a detector. By amplifying the amount electrons emitted from the sample it is possible to measure small fluctuations in the amount of electrons emitted at a specific kinetic energy.

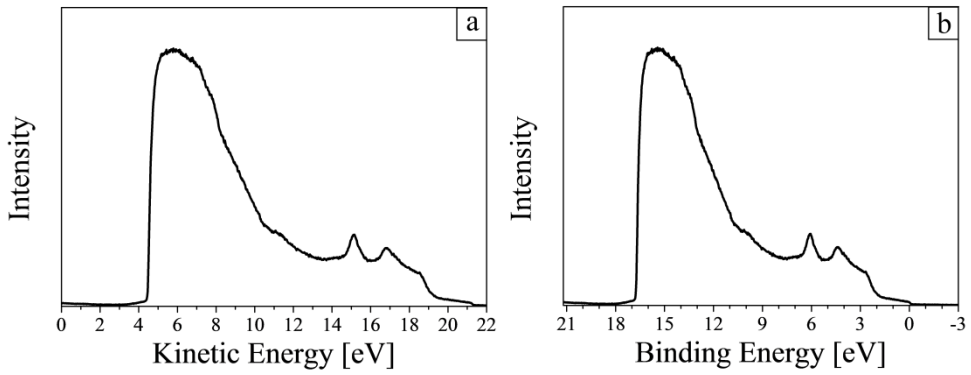

Figure 4.3 Shows the conversion of, (a) the kinetic energy spectrum to, (b) the binding energy spectrum for a metallic sample.

Figure 4.3 shows a typical kinetic energy spectrum for a material measured by UPS; in this case the sample is a metal. The kinetic energy of electrons is often converted into a binding energy spectrum with the Fermi level calibrated to zero binding energy. This is to make the information about the material independent of the energy of the exciting photon. The binding energy spectrum consists of two separate spectrums superimposed upon one another; these are the spectra for the primary and secondary electron emission. Two spectra are present due to the fact that the emission of electrons is often a multistep process; initially photons cause the excitation of an electron from its ground state into an excited state. These excited electrons are then free to move within the material and those that travel towards the surface have a chance of emission from the sample. Once the electron reaches the surface of the sample if the energy of the electron exceeds the work function of the material the electron will be emitted. However during electron transport to the surface of the sample scattering can occur leading to energy loss for the electron, the distance that an electron can travel

before being scattered is called its inelastic mean free path (IMFP) and determines the maximum depth that an electron can escape from a sample, for UPS this is typically less than 5nm.[7,8] Primary emission electrons are electrons that are emitted from the sample without any of these scattering events occurring. Secondary electrons are emitted electrons that have undergone these scattering events, this means that typically primary emission electrons only originate close to the surface of the sample. The intensity of secondary electron emission can be estimated by using a Tourgaard background calculation; this models the distribution of energy of electrons that undergo an energy loss process due to inelastic scattering. [9] **Figure 4.4** gives a simplified diagram of the electron emission from the sample and in addition shows the contribution to the UPS spectra of the primary electrons and secondary electrons as calculated using a Tougaard background function.

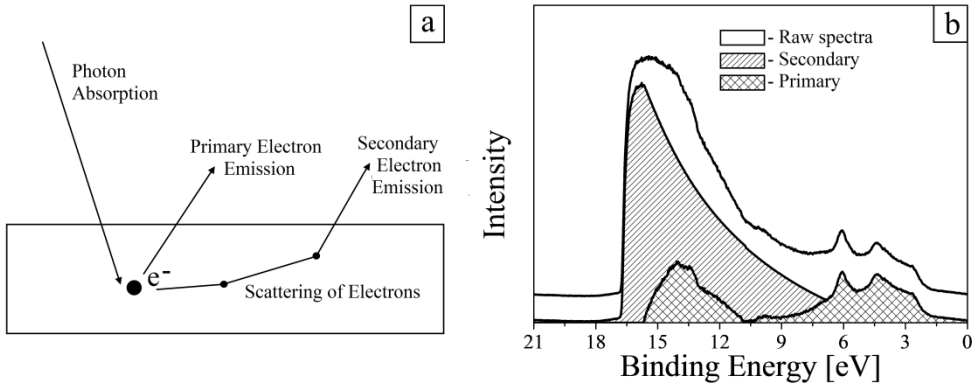

Figure 4.4 Primary and secondary electron emissions make up the UPS spectra, (a) shows a simplified version of the origins of primary and secondary electrons and (b) shows the contribution of primary and secondary electrons in UPS spectra.

Due to the low photon and electron energies that are associated with UPS the technique lends itself to studying in detail the energy level states close to the Fermi level. These states are important within organic electronic devices as the energy of these states often determmine the transfer of charge carriers from one material to another. UPS can be used to measure the work function of a material, the Fermi level, the valence band position and HOMO, and density of occupied states close to the Fermi level allowing for a better understanding of how charge carriers will behave at an interface. Workfunctions of a material can be determined by observing the position of the cut-off for the secondary electron emission. This is the steep drop off that occurs at high binding energies in the secondary electron contribution to the spectrum. The physical origin behind this is due to the fact that the binding energies measured for secondary electrons are not just the energy needed to remove the electron from their bound orbital but also the energy lossed during scattering collisions. If the energy of the electron drops below the workfunction of the material then it is unable to escape from the surface and be measured by the instrument. Therefore a maximum limit to the amount of energy an electron can lose and hence the maximum binding energy an electron can have within a sample depends upon the workfunction of the sample and the energy of the exciting photon given by **Equation 4.5**. Φ is the workfunction of the material and $E_{Cut\text{-}Off}$ is the maximum binding energy value that the UPS spectra measures.

$$\Phi = E_{Photon} - E_{Cut-Off} \qquad \textbf{Equation 4.5}$$

In order for this to be true the Fermi level of the material has to be at zero binding energy, this normally occurs within the analysis chamber however if charging of the

sample occurs due to the high amount of electrons lost during measurement the Fermi level can shift. Finding the Fermi level position within a material can vary in difficulty depending on the material that is being measured. Metals have high density of occupied states that extend all the way to the Fermi level at binding energies lower than the Fermi level the signal rapidly drops to zero. **Figure 4.5**a shows the Fermi edge for the metallic sample shown previously, determination of the position is fairly simple and can be done by eye. For semiconducting materials such as metal oxides and organic polymers the determination of the position of the Fermi level is difficult, this is due to these materials having very low density of states between the valence band and the Fermi level. **Figure 4.5**b shows the same region but for a semiconducting material. By changing the scaling and smoothing the spectra using an average adjacent filter it is possible to see clearly the position of the Fermi level. **Figure 4.5**c shows the same semiconductor spectra after smoothing and rescaling of the spectra.

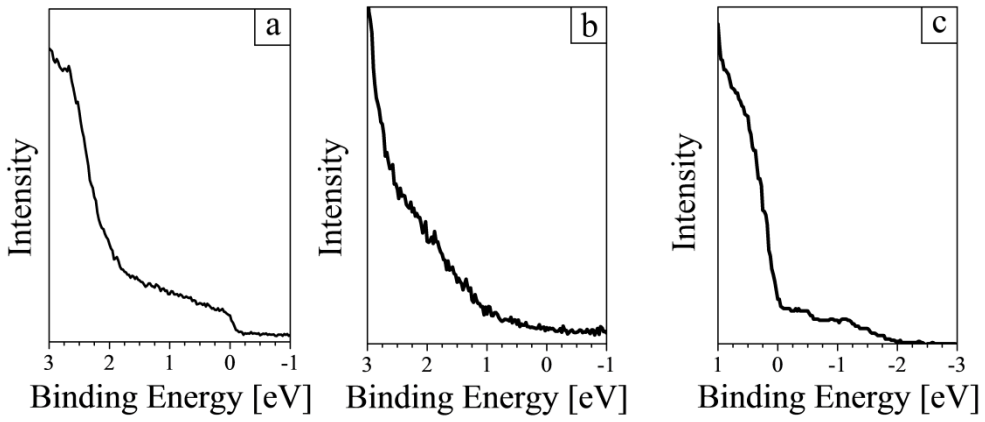

Figure 4.5 Locating the Fermi level for different materials in order to determine charging of the sample, (a) shows a metallic sample, (b) shows a semiconducting sample and (c) shows the same semiconducting sample after smoothing and rescaling of the spectra.

Valence band onset, HOMOs and defect states are easy to determine via UPS, these features are due to primary electron emission from occupied orbitals. **Figure 4.6** shows the valence region of three different samples. A metal oxide sample is shown in **Figure 4.6**a, determination of the valence band onset is done by observing the background emission of defect states at lower energies and the emergence of the highest occupied orbital, in the case of this metal oxide it is the O2p orbital. When exposed to any form of atmospheric conditions a thin layer of material from the surrounding environment will stick to the surface, these are often organic materials Defect states that are observed in **Figure 4.6**a are due to these organic molecules and the subsequent charging of them. In addition defect states in metal oxides can be formed due to the reduction in the oxidation state, **Figure 4.6**b shows a sample in which the material has decomposed from a stoichiometric metal oxide to a mixture of several oxidation states. This reduction leads to the reoccupation of the orbitals that electrons were previously donated from via π-backbonding to fill the O2p orbital. These orbitals are at lower binding energies than the O2p orbital leading to emission of electrons at lower binding energies. For organic materials the HOMO onset can be determined, **Figure 4.6**c shows an organic sample. The UPS emission of organic samples consists of several low intensity peaks closely packed with the peak at the lowest binding energy being the highest occupied orbital. The onset of this emission is the edge of the HOMO and can this be determined in a similar way to the valence band of metal oxides by observing the intercept of the emission peak and the background emission.

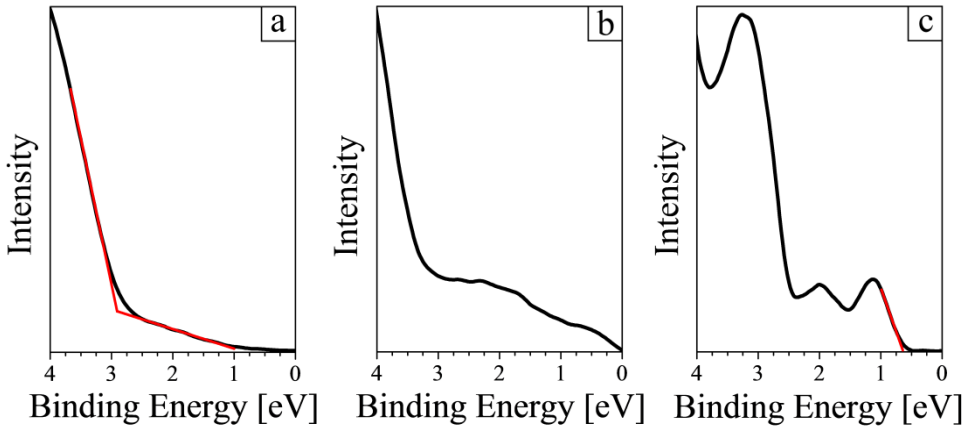

Figure 4.6 Valence region of samples studied by UPS showing (a) the valence band onset for a metal oxide, (b) defect and/or metallic states (c) the HOMO onset of an organic semiconductor.

UPS spectra are taken using the He(I) emission line, full scans are done between 21.2eV and -3eV and a higher intensity scan is taken between 5eV and -3eV. For the full spectrum scans the pass energy is set at 10eV, the energy step of the scan is set at 0.025eV, the aperture size used is 110μm and the dwell time was 250ms. For the higher intensity scans at lower binding energies the slot aperture was used, this is the largest aperture size available in the instrument. Initial analysis of the UPS spectra has been done using CasaXPS software package, data has then been exported to Origin graphing software to create plots and perform smoothing of the spectra.

4.3. X-Ray Photoelectron Spectroscopy

XPS like UPS involves the study of the kinetic energy of electrons emitted from the surface of a sample via the photoelectric effect. However with XPS higher energy X-

rays are used as the incident photons allowing for the study of electrons bound within higher energy orbitals. XPS uses photons with an energy of 1486.6eV, the source of these monochromatic x-rays is from the bombarding an aluminium target with high energy electrons. These high energy electrons can remove electrons from high binding energy shells such as the 1s shell. When this occurs, electrons occupying higher energy levels decay through radiative emission giving characteristic emission lines. [10] In the case of aluminium the 2p to 1s transition leads to the strong emission of x-rays, this transition is called the Al-kα transition. On top of this Bremsstrahlung emission occurs due to the rapid deceleration of electrons, the Bremsstrahlung spectrum and in addition lower intensity Al-Kβ transitions are filtered out using a quartz crystal as a diffraction grating to scatter the x-rays.[4,5,11-13]

Measuring the emission of electrons from higher binding energy orbtials can reveal information about the chemical structure and abundance of elements within a material. [5] Chemical structures can be inferred by observing shifts in the binding energy of the orbitals for an element. In order to observe these shifts high resolution scans of an orbital need to been taken, however there are constraints on choosing an orbital to observe. A maximum binding energy is set by the energy of the exciting photon of 1486.6eV and high resolution scans of lower energy binding energies below 100eV are not taken due to the low intensity of emission due to reduced primary electron emission and increased absorption by contaminant layers. [8] In addition if a sample has multiple elements within it, as is often the case, some orbitals will have binding energies that overlap. Most samples due to exposure to air have contamination from Carbon, Nitrogen and Oxygen each of these elements have electrons occupying the 1s, 2s and 2p orbitals. Binding energies of the 2s and 2p orbitals of these elements

are in the low intensity region of the XPS spectra therefore the only orbitals for Carbon, Nitrogen and Oxygen that are practically observable via XPS are the 1s-orbitals. The binding energy of these emissions are 284.2eV, 409.9eV and 543.1eV, there are several orbitals for d-block metals that overlap these include the $Mo3p_{1/2}$ peak at 411.6eV, $Sc2p_{1/2}$ at 403.6eV, $Cd3d_{3/2}$ at 411.9eV and Hf4s at 538eV. [14] In addition there are more that due to chemical shifts during bonding may mean the oxides of the d-block metals orbital emissions may overlap the commonly seen carbon, nitrogen and oxygen peaks.

In order to determine what chemical state a material is in when observing a high resolution scan of a specified orbital the peak must be broken down into several individual Gaussian peaks offset by different energies. In order to do this a background correction is needed, this is to allow for the analysis of the electrons emitted directly from orbital and to remove as much of the secondary electrons as possible. There are several different background corrections that can be used including linear, Tougaard, or Shirley. **Figure 4.7** shows these different background spectra used on a high resolution scan of the Mo3d peak for a fully oxidized MoO_3 sample. **Figure 4.7**a shows the simplest background, this is a linear background; this background substitution takes the intensity at two different points ($E_1$and E_2) within the spectrum and creates a signal that increases linearly across this region. Linear approximations can be used with high accuracy if the intensity before and after the peak is of a similar value. [15]

A Tougaard background is shown in **Figure 4.7**b this spectrum is formulated using an energy loss cross-section where electrons undergo energy loss via inelastic scattering before being emitted from the surface of a sample.[9,16] Electrons that are emitted from an orbital with binding energy of E will contribute towards the measured

intensity at higher binding energy levels. The amount of energy that is lost depends upon the depth of absorption and the inelastic mean free path of the electron (IMFP). The IMFP in addition is dependent upon the energy of the electron with maximum inelastic scattering occurring for electrons with kinetic energies in the region of 20eV to 100eV. Tougaard backgrounds are useful for estimating the background intensity over large regions such as chemically shifted p-orbitals, d-orbitals and f-orbitals, and for regions with high energy loss due to scattering, this typically occurs for scans where the emitted electrons have low kinetic energy.[15,17]

The Shirley background is the most commonly used background correction and is shown in **Figure 4.7**c this background correction uses an algorithm to relate the area of the measured spectra against itself. It does this by taking two points E_1 and E_2 where these points represent electrons with kinetic energy below the emission peak and above the emission peak respectively. By using an iterative process the Shirley background calculates the area for electrons with kinetic energies higher and lower than the peak energy after an initial background correction. The areas of the electrons with energies above and below the peak must match a specified ratio and once this is achieved background intensity is determined. The Shirley background is a very powerful background determination however its uses can be limited when it comes to the calculating the background for chemically shifted orbitals this is due to the background calculated often subtracting from the real spectra of these chemically shifted materials.[17,18]

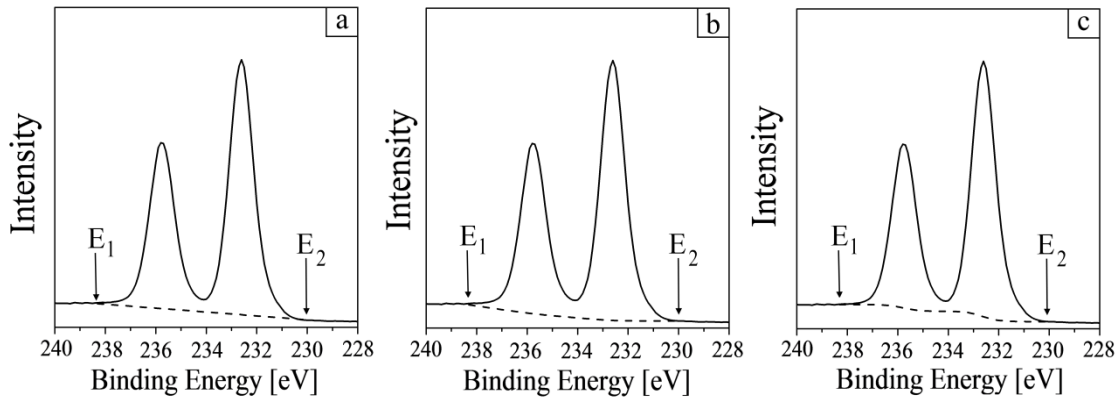

Figure 4.7 High resolution scan of the Mo3d orbital showing the intensity of calculated background between points E_1 and E_2 using three different models, (a) Linear, (b) Tougaard, and (c) Shirley.

Once the background corrections are made to a peak it is possible to determine the chemical state of a material. **Figure 4.8** shows a simple s-orbital spectra, **Figure 4.8**a has the spectra before correction along with the background intensity, in this example a Shirley background correction is used. **Figure 4.8**b shows the spectra after correction with several peaks fitted corresponding to different chemical states that that the element is within. Shifts in the binding energy occur due to changes within the oxidation state of an atom (Atomic effects) and the surrounding environment (extra-atomic effects). With increased oxidation state of an atom the binding energy of an electron will increase due to an increase in the electromagnetic force exhibited between the core and the remaining outer electrons. In addition surrounding atoms indirectly bound to the element being observed can cause similar shifts due to the electronegativity of surrounding atoms and their ability to cause perturbations in the electron density surrounding the observed atom.[7,19,20]

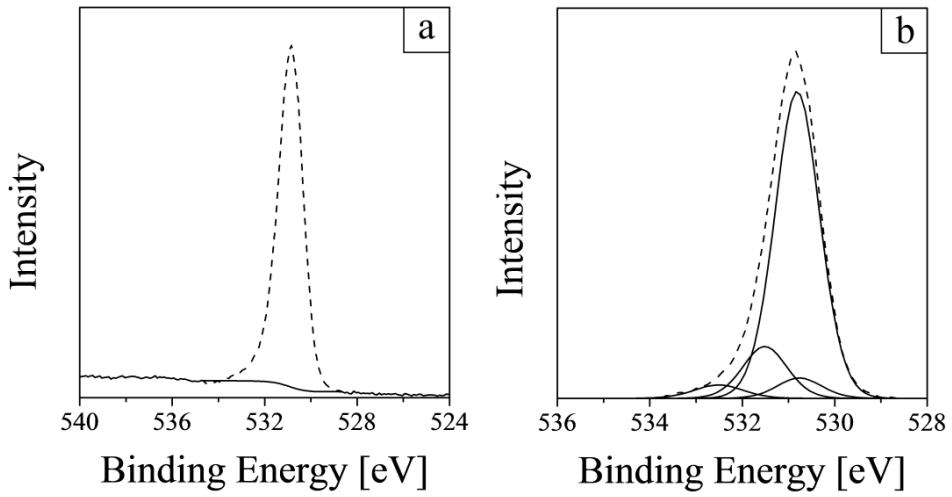

Figure 4.8 A sample s-orbital spectra showing (a) the measured spectra with a Shirley background, and (b) spectra corrected for background emission with fitted peaks.

Spectra from d-orbitals and p-orbitals are more complex than s-orbitals, this is due to the addition of the splitting of orbitals due to spin-orbit coupling. When an electron has an orbital angular momentum that is not zero the magnetic fields established by the spin of the electron and the orbit of the electron can interact. This interaction is either constructive or destructive leading to either an increase in the binding energy of an electron or a decrease. **Figure 4.9** shows a high resolution d-orbital spectra and it can be seen that two peaks are observed. For each element the splitting of a particular orbital has a fixed energy gap that is dependent upon the strength of the spin-orbit coupling as. In addition the relative areas of the two doublet peaks depends upon the orbital that the electron has been emitted from.

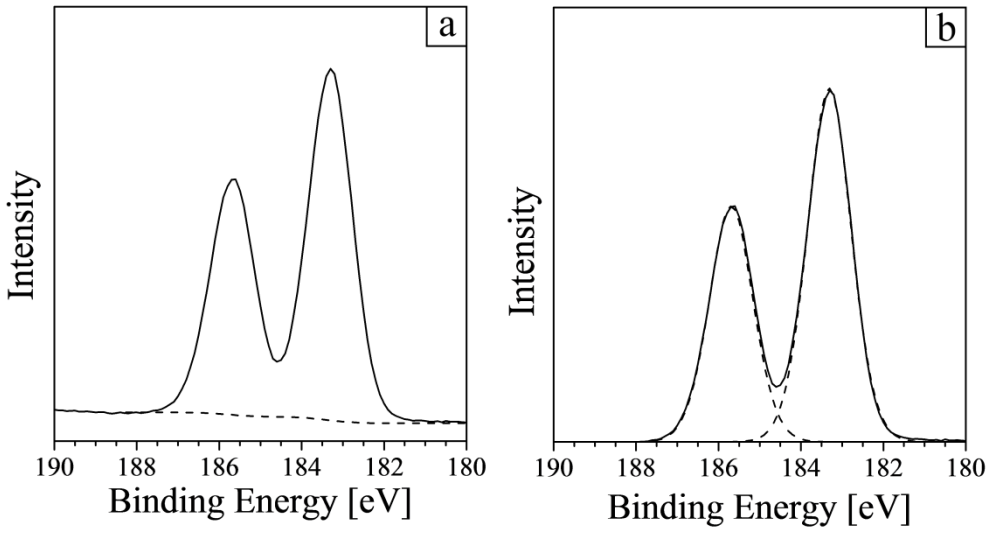

Figure 4.9 A sample d-orbital spectra showing (a) the measured spectra with a Shirley background, and (b) d-orbital spectra with a single chemical state with split orbitals.

The ratio of areas for the peaks can be calculated for different orbitals by using **Equation 4.6** where *l* is the Azimuthal quantum number and *s* is the spin of an electron. For the p-orbital, d-orbital and f-orbitals the ratio of emission from the peaks is 1:2, 2:3 and 3:4 respectively.

$$2(l-s)+1 : 2(l+s)+1 \qquad \textbf{Equation 4.6}$$

Initial analysis of the UPS spectra has been done using CasaXPS software package, data has then been exported to Origin graphing software to create plots and perform smoothing of the spectra. For the wide scan spectrum the pass energy is set at 10eV, the energy step of the scan is set at 0.025eV, the aperture is a slot apeture and the dwell time was 250ms. For the higher resolution scans at lower binding energies the slot aperture was used, this is the largest aperture size available in the instrument.

4.4 Spectroscopic Ellipsometry

Spectroscopic ellipsometry is a powerful technique that can be used to calculate several properties of a material including the thickness, refractive index and extinction coefficient. [21] It is done by measuring the change in phase and intensity of polarization of light as it is reflected from a surface of a substrate coated in a layer of the material being studied. **Figure 4.10** shows the schematics of a spectroscopic ellipsometer, at point one in the figure light has been generated from a discharge lamp and is made up of multiple wavelengths spanning from the near UV to the near IR. Light is then passed through a monochromator and at point two the light consists of randomly polarized light at a single wavelength. This light is then passed through a polarizing filter that can be rotated to polarize light to a specified polarization. At point 3 polarized monochromatic light is transmitted through the film and reflected off of the silicon substrate, the intensity and phase of the light will vary due to this transmission and reflection. At point 4 the light passes through a second polarizing filter known as the analyzer, where the intensity is then measured by a CCD camera.[22-24]

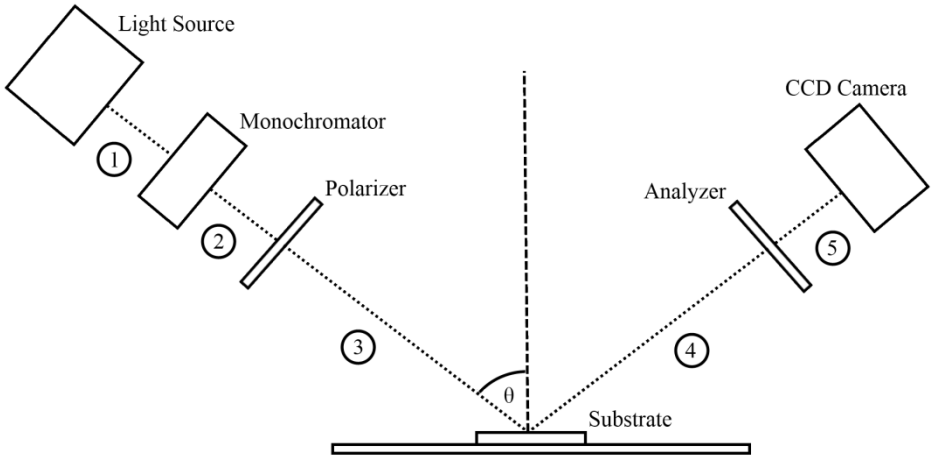

Figure 4.10 Schematic of a spectroscopic ellipsometer, the dotted line traces the path of light through the equipment; the angle θ is typically set at 30^{o} to avoid high loss due to reflections at the interface.

By varying the angle of the analyzer the exact polarization and intensity of the light can be measured. From the change in phase (Δ) and the change in intensity of polarization (Ψ) the ratio of the reflectance of light in the s-plane and p-plane can be determined. **Equation 4.7** shows the relationship between Δ, Ψ, the reflectance ratio (ρ), and the reflectance of light in the p-plane (r_p) and s-plane (r_s) at an interface. [23]

$$\rho = \frac{r_p}{r_s} = \tan(\Psi)e^{i\Delta} \qquad \textbf{Equation 4.7}$$

The reflectance values here can be calculated using the Fresnel equations (**Equation 4.8a** and **Equation 4.58**), Δ and Ψ can then be related to the complex refractive index of the incident material (n_a) and the transmitting material (n_b). [2] For samples with multiple layers the Fresnel equations are applied at all the interfaces and the resulting interactions between the reflected fractions of light are solved in order to determine the final value of Δ and Ψ.

$$r_s = \frac{(n_a \cos\theta_i - n_b \cos\theta_t)}{(n_a \cos\theta_i + n_b \cos\theta_t)} \qquad \textbf{Equation 4.8a}$$

$$r_p = \frac{(n_b \cos\theta_i - n_a \cos\theta_t)}{(n_a \cos\theta_t + n_b \cos\theta_i)} \qquad \textbf{Equation 4.8b}$$

Ellipsometry is not able to directly measure the thickness or optical properties of a material; instead a model is used that approximates the structure of the sample being measured. Properties such as the thickness of these layers and the complex refractive index can then be varied and the values used within the Fresnel Equations to determine values for Δ and Ψ. These calculated values can then be compared against the values measured experimentally, in order to obtain the most accurate value. An iterative process of changing the values is used to obtain the minimum least-square error when matching the simulated data against the experimentally measured data. In order to model the system a set of layers of different materials need to be defined, for every model the first layer is the underlying substrate and is modelled as an infinitely thick layer of silicon. On top of this a thermal oxide layer of SiO_2 is placed, determination of the thickness of this layer can be done by using a blank substrate and measuring Δ and

Ψ, using reference data for the optical properties of the Si and SiO_2 layer the thickness of the thermal oxide can be determined. By calculating the thickness and having reference values for the optical constants of the native oxide layer the amount of layers that need to be fitted when modelling the sample will be reduced, increasing the accuracy of the fit.

Once the oxide layer has been characterised the sample with the material is then measured, the model is then altered to account for the fact an additional layer is present. In the model this layer typically consists of two regions the bulk and the surface with the surface layer being used to model both the roughness of a material along with the effect of exposing the bulk material to the environment. Examples of this effect include oxidation and adsorption of material onto the surface. In addition to modelling the structure of the sample a model is needed for the material in order to generate the optical constants by iterative fitting of the data. The choice of model is dependent upon the material type and the region of the spectrum that the material is being fitted over.

Analysis of deposited materials begins with obtaining a value for the thickness of the material being studied, for materials with a band gap this process is done by modelling across the transparent region of the spectra in order to remove the complex part of the refractive index. A simple transparent Cauchy model can be used to model the refractive index and get an estimate of the thickness of the material [25]. The Cauchy equations for the refractive index are shown in **Equation 4.9**, the terms A to C are variables for fitting and λ is the wavelength. [22]

$$n(\lambda) = \frac{A}{\lambda^0} + \frac{B}{\lambda^2} + \frac{C}{\lambda^4} \ldots \qquad \textbf{Equation 4.9}$$

Afterwards this rough estimate of the thickness is added to the model in order to reduce the amount of fitting parameters. The model is once more fitted against the data across a wider region of the spectrum including the absorbing region. The material model needs to take account of absorption and hence the addition of the complex part of the refractive index. An absorbing version of the Cauchy model can be used in which a additional Lorentzian oscillator is used to model the complex part of the refractive index in order to account for absorption within the material. [26] **Equation 4.10** shows the equation for the Lorentzian oscillator as a function of photon energy (E). [22]Where the amplification factor (A), the broadening of the oscillator peak (B), the energy of the oscillator peak (E_c), and the offset for the real part of the dielectric constant ($\varepsilon_{1.offset}$) are terms to be fit.

$$\tilde{\varepsilon}(E) = \varepsilon_{1.offset} + \frac{AE_c}{E_c^2 - E^2 - iBE} \qquad \textbf{Equation 4.10}$$

For metals the optical response can be modelled using Drude-Lorentz model in which the Lorentzianz oscillator is modified to take account of high concentration of free charge carriers that exist in metals. [27] The restoring force that is the cause behind the centralisation energy does not exist for free charge carriers and so is eliminated. The Lorentz equation then becomes **Equation 4.11** for metallic films where the Plasmon energy (E_p) is related to plasma frequency of a material. [22]

$$\tilde{\varepsilon}(E) = A\left(\varepsilon_{1.offset} - \frac{E_p^2}{E^2 - iBE}\right) \qquad \textbf{Equation 4.11}$$

4.5 Atomic Force Microscopy

Atomic Force Microscopy (AFM) is a technique that is capable of measuring the structure of a samples surface in the scale of nanometres. AFM works by scanning a probe across the surface of a sample, this probe consists of a cantilever with a tip on the underside that is only a few nm in size. By measuring the deflection of the cantilever as the tip scans the surfaces it is possible to determine the relative height of the surface that the tip is in contact with.[28,29] **Figure 4.11** shows an atomic force microscope, the deflection of the cantilever is measured by reflecting a laser from the surface of the cantilever and measuring the position of the laser spot using a quadrant photodiode. Scanning of the surface of the sample is achieved by using a piezoelectric controlled X, Y stage to move the sample relative to the probe.

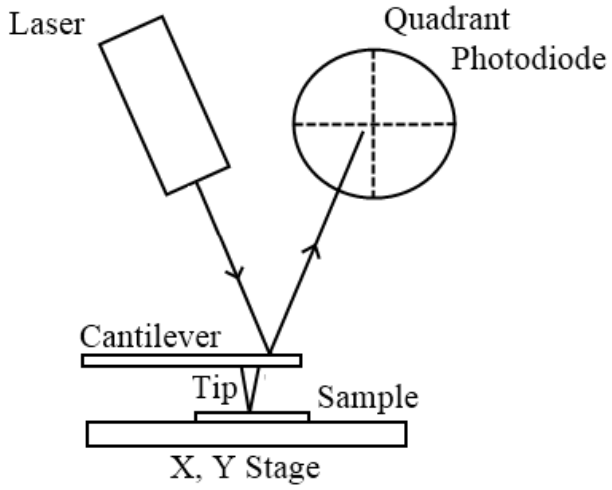

Figure 4.11 Simplified schematic of the Veeco Dimension 3100 atomic force microscope

With AFM the surface can be scanned in different modes, this can either be in contact mode where the tip is in physical contact with the surface and the deflection of the tip directly relates to the height; non-contact mode where the cantilever is oscillated at low amplitude above the surface and the change in amplitude and frequency of the oscillation is used to determine the height from the surface; or tapping mode where the cantilever is oscillated with a high amplitude and the tip comes in intermittent contact with the surface. In this work the samples have all be scanned using tapping mode in order to reduce any damage to the sample due to the tip.[29-31] The cantilever is driven close to its resonant frequency by a piezoelectric motor, when the tip gets closer to the surface it begins to make contact and lift away from the surface. This contact with the surface causes loss of energy and a reduction in the amplitude of oscillation and the amount the amplitude is changed by is directly related to the distance between the surface and the tips resting position. By using a feedback loop to vary the height in

order to maintain constant oscillation amplitude it is possible to determine features upon the surface of a sample and measure their dimensions. Measurements of samples have been performed using a Veeco dimension 3100 instrument, the Gwyddion software package was used to analyse the data that had been obtained and to create figures. The AFM tips used were purchased from Budget Sensors (300G-Al) with a resonance at 300 kHz and a spring constant of 40 N m–1.

4.6 References

[1] C. Palmer. *Diffraction Grating Handbook*. 6th Edition. New York: Newport Corporation; 2005

[2] E. Hecht. *Optics*. 4th Edition. San Francisco: Addison Wesley; 2002

[3] A. Einstein. Über einen die Erzeugung und Verwandlung des Lichtes betreffenden heuristischen Gesichtspunkt. *Annalen Der Physik*. **16** (1905) 132-148 (English Translation by D. T. Haar. *The Old Quantum Theory*. Oxford: Pergamon Press; 1967)

[4] K. Siegbahn. Electron Spectroscopy and Molecular Structure. *Pure and Applied Chemistry*. **48** (1976) 77-97

[5] K. Siegbahn. Electron Spectroscopy for Atoms, Molecules and Condensed Matter. *Reviews of Modern Physics.* **54** (1982) 709-728

[6] I. Newton. *Philisophiæ Naturalis Principia Mathematica*. London: Royal Society; 1687 (English Translation by D. Motte (1729))

[7] S. Hüfner. *Photoelectron Spectroscopy: Principles and Applications*. 3rd Edition. Berlin: Springer. 2003

[8] D. R. Penn. Quantitative Chemical Analysis by ESCA. *Journal of Electron Spectroscopy and Related Phenomena*. **9** (1976) 29-40

[9] S. Tougaard. Quantitative Analysis of Inelastic Background in Surface Electron Spectroscopy. *Surface and Interface Analysis*. **11** (1988) 453-472

[10] P. K. Ghosh. *Introduction to Photoelectron Spectroscopy*. 1st Edition. New York: John Wiley & Sons; 1983

[11] J. C. Vickerman & I. S. Gilmore. *Surface Analysis- The Principle Techniques*. 2nd

Edition. Chichester: John Wiley & Sons; 2009

[12] U. Gelius, E. Basilier, S. Svensson, T. Bergmark & K. Siegbahn. A High Resolution ESCA Instrument with X-Ray Monochromator for Gases and Solids. *Journal of Electron Spectroscopy and Related Phenomena*. **2** (1974) 405-434

[13] J. H. Hubbel. Photon Mass Attenuation and Energy-Absorption Coefficients. *The International Journal of Applied Radiation and Isotopes*. **33** (1982) 1269-1290

[14] D. R. Lide. *Handbook of Chemistry and Physics*. 79th Edition. Boca Raton: CRC Press; 1998

[15] A. Proctor & D. M. Hercules. Inelastic Background and Peak Area Determination in X-Ray Photoelectron Spectroscopy (ESCA). *Applied Spectroscopy*. **38**. (1984) 505-518

[16] S. Tougaard & P. Sigmund. Influence of Elastic and Inelastic Scattering on Energy Spectra of Electrons Emitted from Solids. *Physical Review B*. **25** (1982) 4452-4466

[17] H. Tokutaka, N. Ishihara, K. Nishimori, S. Kishida & K. Isomoto. Background Removal in X-Ray Photoelectron Spectroscopy. *Surface and Interface Analysis*. **18** (1992) 697-704

[18] D. A. Shirley. High-Resolution X-Ray Photoemission Spectrum of the Valence Bands of Gold. *Physical Review B.* **5**. (1972) 4709-4714

[19] I. I. Sobel'man, L. A. Vainshtein & E. A. Yukov. *Excitation of Atoms and Broadening of Spectral Lines*. 2nd Edition. Berlin: Springer-Verlag; 1995

[20] R Jenkins. *An Introduction to X-Ray Spectrometry*. 1st Edition. London: Hayden & Sons Ltd; 1976

[21] A. Rothen. The Ellipsometer, an Apparatus to Measure Thicknesses of Thin

Surface Films. *Review of Scientific Instruments*. **16** (1945) 5

[22] H. G. Thomas & E. A. Irene. *Handbook of Ellipsometry*. 1st Edition. Norwich: Springer; 2005

[23] R. M. A. Azzam & N. M. Bashara. *Ellipsometry and Polarized Light*. Amsterdam: North-Holland Publishing Company; 1977

[24] M. Bass. *Handbook of Optics (Volume I): Geometric and Physical Optics, Polarized Light, Components and Instruments*.3rd Edition. New York: McGraw-Hill; 2005

[25] H. Kumagai & K. Toyoda. In Situ Ellipsometric Diagnosis for Controlled Growth of Metal Oxides with Surface Chemical Reactions. *Applied Surface Science*. **82-83** (1994) 481-486

[26] D. J. Santjojo, T. Aizawa & S. Muraishi. Ellipsometric Characterization on Multi-Layered Thin Film Systems During Hydrogenation. *Materials Transactions*. **48** (2007) 1380-1386

[27] A. D. Rakic, A. B. Djurišic, J. M. Elazar & M. L. Majewski. Optical Properties of Metallic Films for Vertical-Cavity Optoelectronic Devices. *Applied Optics*. **37**. (1998) 5271-5283

[28] G. Binnig, C. F. Quate & C. Gerber. Atomic Force Microscopy. *Physical Review Letters*. **56** (1986) 930-933

[29] E. Meyer. Atomic Force Microscopy. *Progress in Surface Science*. **41** (1992) 3-49

[30] S. N. Magonov, V. Elings & M. H. Whangbo. Phase Imaging and Stiffness in Tapping-Mode Atomic Force Microscopy. *Surface Science*. **375** (1997) L385-L391

[31] S. Morita, R. Weisendanger & E. Meyer. *Noncontact Atomic Force Microscopy Volume 1*. 1st Edition. Berlin: Springer-Verlag; 2002

Chapter 5

Characterisation of Materials via Spectroscopy

5.1 Introduction

Characterisation of materials is important in developing an understanding of the properties of individual layers and how they may behave when introduced into a device. There are many ways that materials can be characterised these include X-ray photoelectron spectroscopy (XPS), Ultraviolet photoelectron spectroscopy (UPS), and spectroscopic ellipsometry. Using these different techniques it is possible to determine chemical structure, electronic structure and the optical properties of a deposited material from these it should be possible to gauge how well they will perform on organic photovoltaic devices. These techniques have been applied to two commonly used vacuum evaporated hole extracting metal oxides, Vanadium (V) Oxide and Molybdenum (VI) Oxide, in addition to the two versions of PCDTBT used within the experimental chapters.

5.2 Metal Oxide: Molybdenum Oxide

Molybdenum Oxide has been used successfully in organic photovoltaic devices as a hole extraction material for various donor polymers including the commonly used poly(3-hexylthiophene-2,5-diyl) (P3HT) and Poly[N-9'-heptadecanyl-2,7-carbazole-alt-5,5-(4',7'-di-2-thienyl-2',1',3'-benzothiadiazole)] (PCDTBT).[1-3] **Figure 5.1** shows photoelectron spectroscopy studies of films of molybdenum oxide deposited by vacuum evaporation. Three different species are observed within the O1s scan, these have been attributed to H_2O absorbed into the film at 532.5eV, hydroxide species adsorbed onto the surface at 531.1eV and Molybdenum-Oxygen bonds at 530.4eV. The percentage of bonds within the film that are associated with water is only 3.7% this scans indicates that absorption of water is limited into vacuum evaporated molybdenum oxide films. Within the Mo3d high resolution scan two different Molybdenum species are seen, these are attributed to Mo^{6+} at 235.8eV/232.6eV and the reduced oxide state Mo^{5+} at 234.6eV/231.4eV. The reduction from stoichiometric Molybdenum (VI) Oxide is due to the high temperature low pressure deposition of the material leading to the leeching of oxygen from the surface of the source material. UPS data shows that the Fermi level of the vacuum deposited molybdenum oxide layer is -5.2eV as calculated from the secondary electron cut-off. The valence band is located 2.8eV below Fermi level, giving a valence band position of -8eV. These values are in agreement with previously reported literature values for molybdenum oxide deposited via vacuum evaporation. In addition literature reports that the band gap of Molybdenum Oxide is between 2.8eV and 3.2eV this would place the Fermi level just below the vacant Molybdenum 4d orbital.

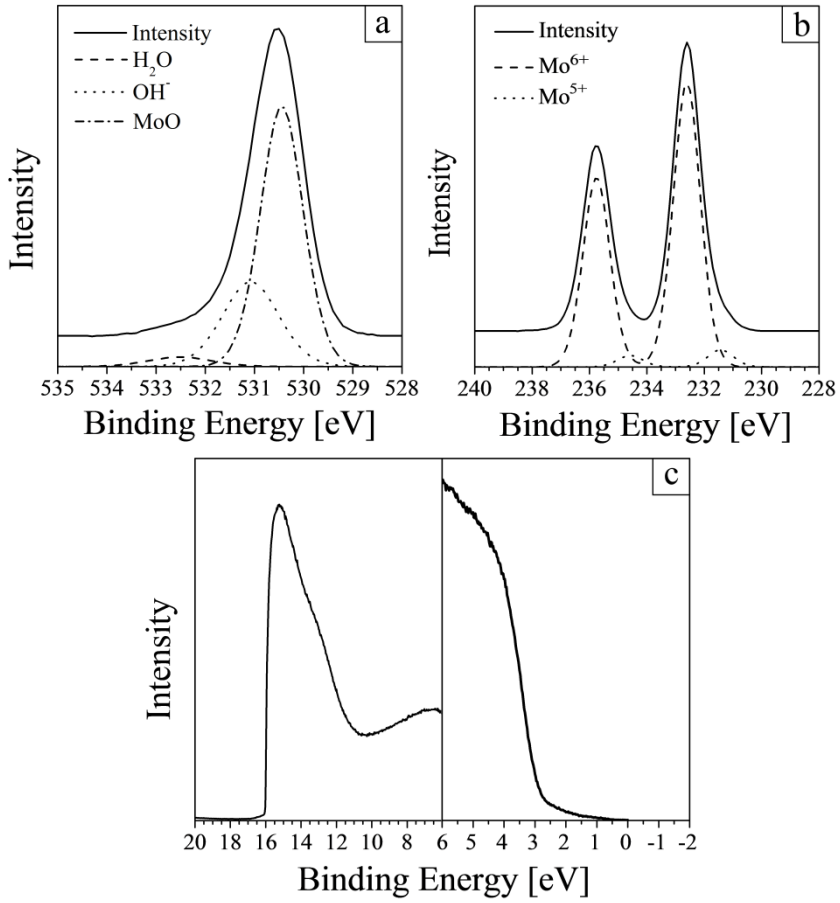

Figure 5.1 Photoelectron spectroscopy scans of vacuum evaporated molybdenum oxide showing (a) the O1s peak, (b) the Mo3d peak, and (c) UPS scans showing the secondary electron cut off and the valence band region.

Figure 5.2 shows the transmittance data for 15nm films of Molybdenum (VI) Oxide a sharp drop in transmission due to the optical absorption is observed with an absorption edge of 420nm giving an optical band gap for the material of approximately 3eV this is close to reported figures for the band gap of the air exposed vacuum evaporated Molybdenum (VI) Oxide.[4]

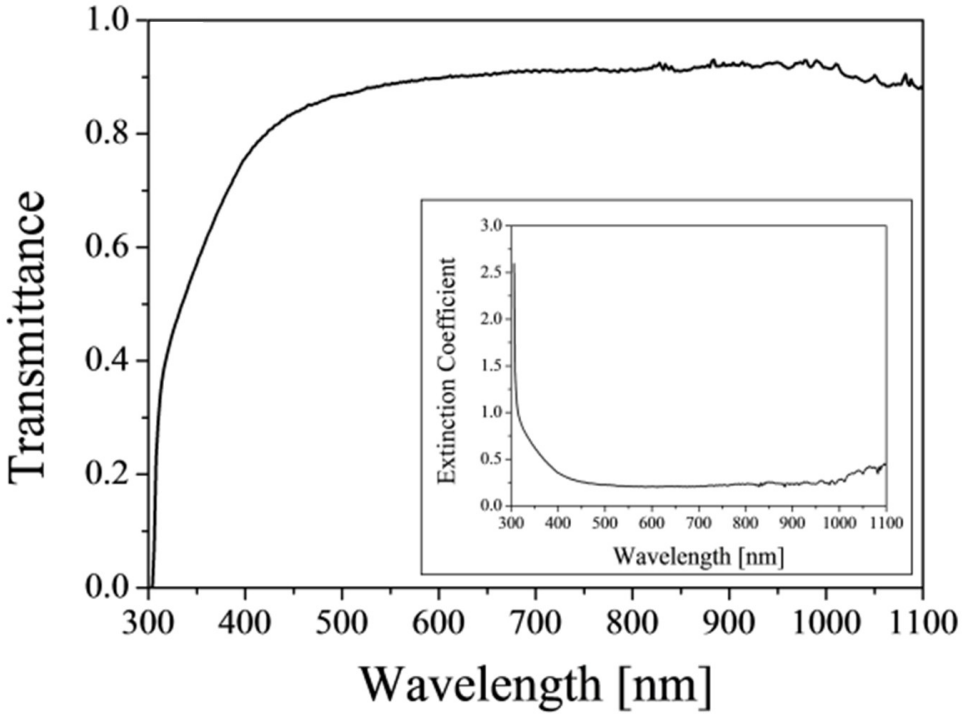

Figure 5.2 Shows optical spectroscopy data for vacuum deposited Molybdenum (VI) Oxide films with the calculated extinction coefficient of the film on the inset.

5.3 Metal Oxide: Vanadium Oxide

Vanadium Oxide, like Molybdenum Oxide, has been successfully used within organic photovoltaic devices. However much of the work done using vanadium oxide has been using shallow HOMO polymers such as P3HT.[1] **Figure 5.3** shows photoelectron spectroscopy scans of vacuum deposited vanadium oxide. Like with Molybdenum Oxide three different species are present within the O1s spectra, they have been attributed to H_2O at 531.4eV, hydroxides adsorbed onto the surface at 530.5eV and Vanadium-Oxygen bonds within the film at 530eV. The amount of bonds associated with water is 10.5%, this value is larger than that for Molybdenum Oxide, the reason for this is likely due to the higher density of Molybdenum Oxide reducing the rate of water absorption. The high

resolution V2p peak shows the presence of two different species, these are attributed to V^{5+} at 524.6eV/517.1eV and V^{4+} at 523.4eV/516.4eV these species are analogous to the Mo^{6+} and Mo^{5+} species respectively with the presence of the reduced state being due to the reoccupation of the 4s orbital for Vanadium and the 5s orbital for Molybdenum. In addition the reduction of the V^{5+} to V^{4+} is due to the high temperature low pressure deposition of the Vanadium (V) Oxide. UPS data shows that the Fermi level of the vacuum deposited film, as calculated from the secondary electron cut-off, as -5.1eV. From the valence band region of the scan it is calculated that the valence band should be approximately 2.3eV below the Fermi level giving an absolute position of -7.4eV.

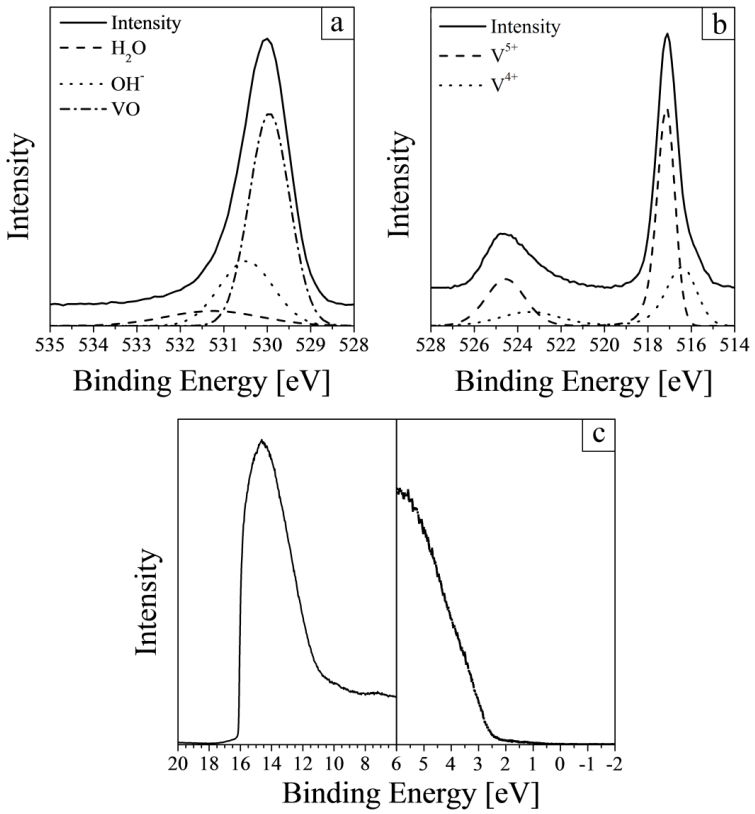

Figure 5.3 Photoelectron spectroscopy scans of vacuum evaporated vanadium oxide showing (a) the O1s peak, (b) the V2p peak, and (c) UPS scans showing the secondary electron cut off and the valence band region.

Figure 5.4 shows the transmittance of the vanadium oxide film along with the calculated extinction coefficient. Ellipsometry data for Vanadium Oxide films was taken and the optical properties of the film determined. Results show that across most of the visible spectrum the coefficient of absorption is close to zero at wavelengths above 700nm the transmittance of the film exceeds 90%. However at shorter wavelengths at 550nm and below where light absorption within the active layer occurs there is reduced transmittance in the vanadium oxide films. The extinction coefficients obtained from absorbance spectroscopy show that the absorbance edge is approximately 520nm, the optical band

gap therefore is approximately 2.4eV this is the same as reported for thick films of Vanadium (V) Oxide.[5]

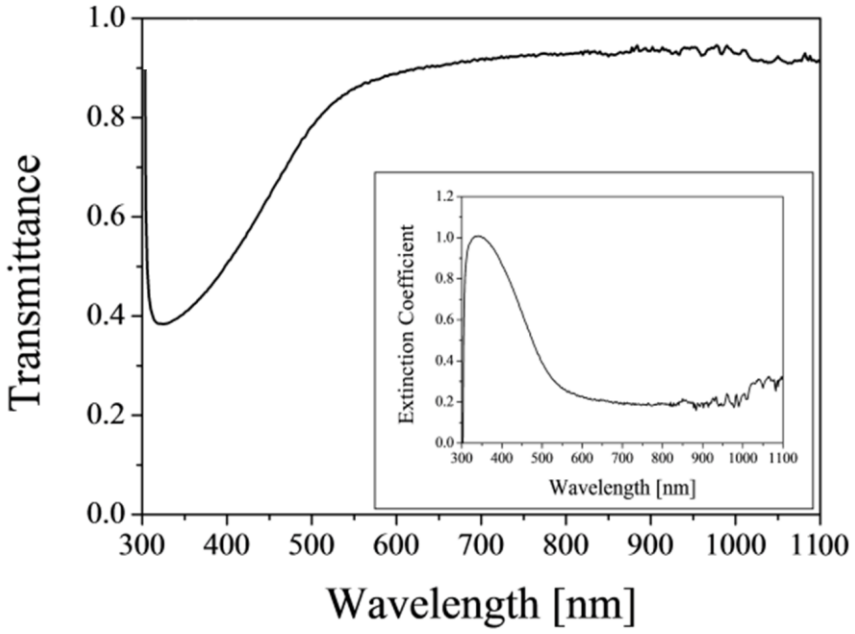

Figure 5.4 Shows absorption spectroscopy data for vacuum deposited Vanadium (V) Oxide films with the calculated extinction coefficient of the film on the inset.

5.4 Organic Semiconductor: PCDTBT

PCDTBT is one of the most commonly used current generation donor materials in bulk heterojunction organic photovoltaic devices. It has been characterised within literature as having a deep HOMO level leading to a deep LUMO level allowing for increased stability within atmospheric conditions, the structure of this material in shown in **Figure 3.2**. Spectroscopic information obtained for this material is shown in **Figure 5.5** UPS has been used to determine both the positions of the Fermi level of the material and the HOMO level. Samples were spun onto ITO coated quartz substrates, it can be seen that

the Fermi level of the material is situated at -3.7eV and the HOMO level being 1.7eV deeper than the Fermi level giving a value of -5.4eV. Absorbance data shows that the peak absorbance of PCDTBT is at approximately 570nm giving an optical bandgap of 2.1eV.

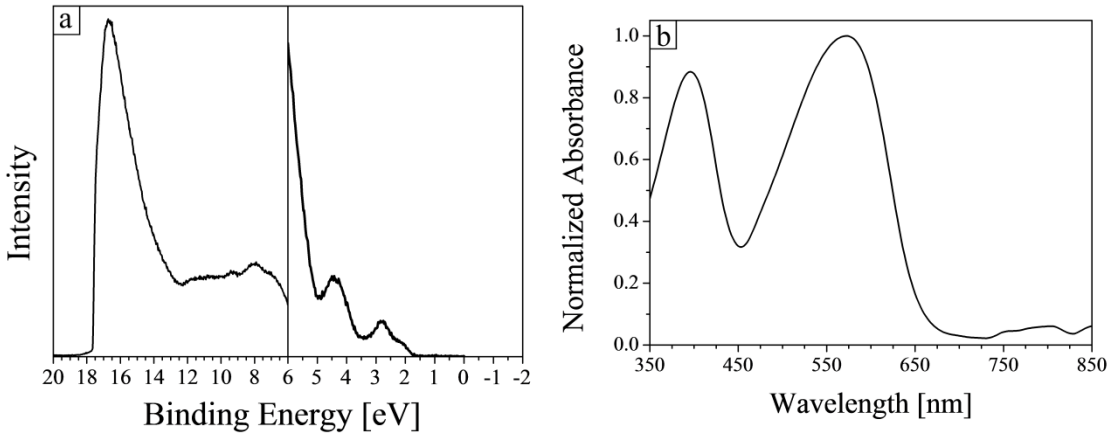

Fig 5.5 Shows spectroscopy data for PCDTBT films where (a) is UPS spectra and (b) UV-Vis absorbance data.

5.5 Organic Semiconductor: PCDTBT-8

PCDTBT-8 is a newly synthesised material with a similar structure to PCDTBT however in order to improve the solubility of the polymer additional side chains have been added to the thiophene unit.[3] The chemical structure of the donor polymer is shown in **Figure 3.2. Figure 5.6** shows spectroscopic data obtained for thin films of PCDTBT-8 spun coat onto ITO substrates, UPS scans show a distinct secondary electron cut off giving a Fermi Level position of -4.8eV, there are several occupied molecular orbitals that can be seen within the PCDTBT-8 spectra. The first of these has a peak at -4.4eV below the Fermi

level, the second at -2.8eV and a final weakly emitting peak which is the highest occupied molecular orbital has a cut off at approximately -0.6eV. This gives an absolute position for the HOMO of approximately -5.4eV, this is close to the value given for PCDTBT indicating the presence of soluble side chains does not significantly alter the electronic structure. One interesting observation is that the first of these two occupied orbitals are in the same positions as occupied orbitals observed in PCDTBT however the peaks observed in PCDTBT-8 are of much lower intensity. The absorption peak of the PCDTBT-8 film is at approximately 540nm this is equivalent to 2.3eV, this gives a LUMO position of -3.1eV.

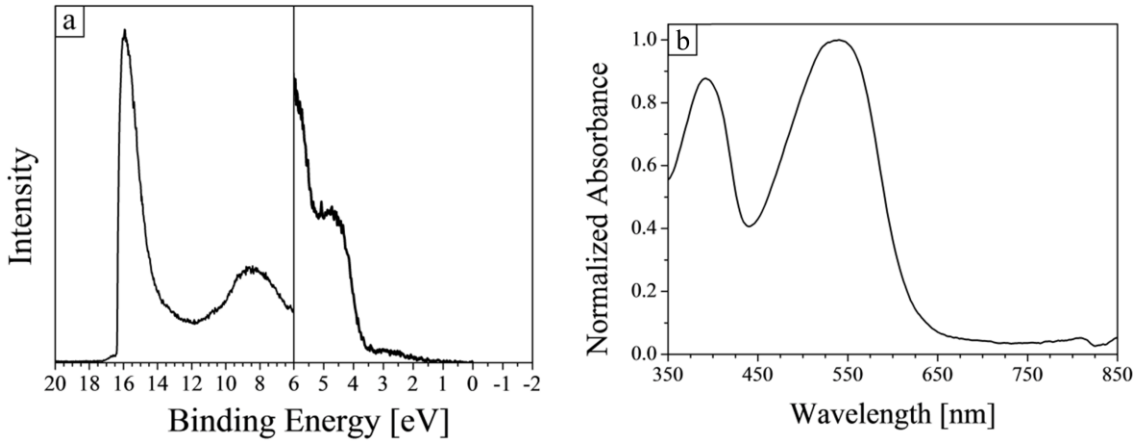

Fig 5.6 Shows spectroscopy data for PCDTBT-8 films where (a) is UPS spectra and (b) UV-Vis absorbance data.

5.6 Conclusion

Through the spectroscopic studies of both molybdenum oxide and vanadium oxide it can be seen that both materials have deep work function with pinning of the Fermi level close to the conduction band. Both materials offer high transmission across the visible spectra; however vanadium oxide shows a lower energy band gap resulting in absorption in the

blue region of the spectra. This absorption in vanadium is at higher energies than the absorption band of the semiconducting donor materials PCDTBT and PCDTBT-8. This results in a reduction in the effective amount of light that can reach the active layer when vanadium oxide is used in comparison to molybdenum oxide. Even with this slight increase in absorption for vanadium oxide both materials have good prospects for being used as hole extraction layers. **Figure 5.7** given below shows the electronic energy levels of relevant materials used throughout this work against each other as determined via spectroscopic studies of the materials and literature values.[2, 6-9]

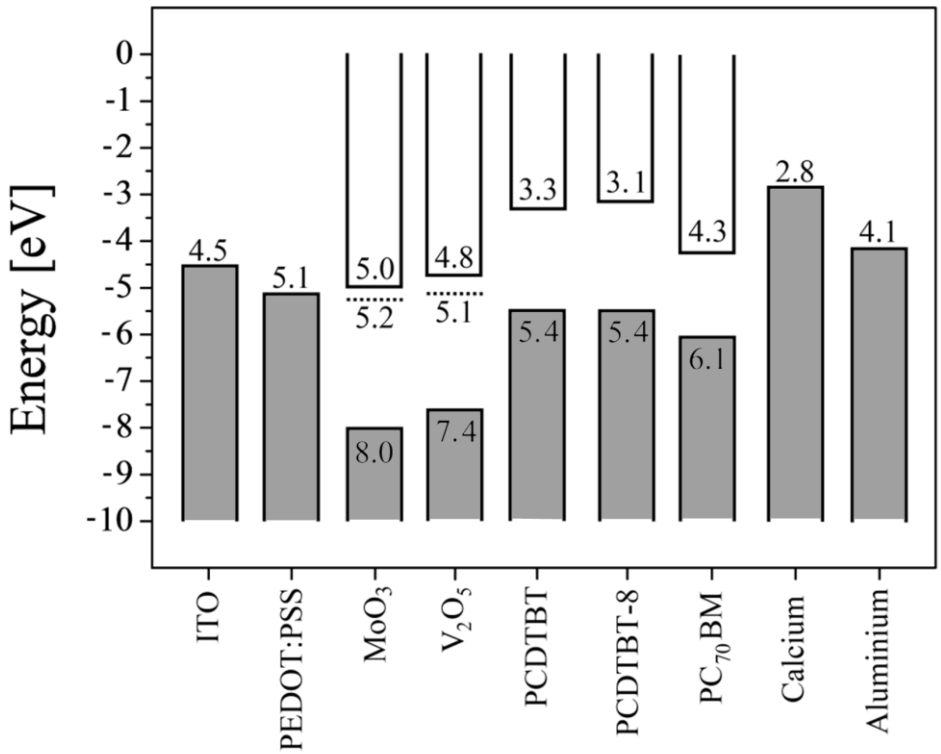

Figure 5.7 An energy level diagram showing the relevant energy levels for each of the materials used throughout the following experimental chapters either determined through spectroscopy of materials or from literature.

5.8 References

[1] V. Shrotriya, G. Li, Y. Yao, C. W. Chu & Y. Yang. Transition Metal Oxides as the Buffer Layer for Polymer Photovoltaic Cells. *Applied Physics Letters*. **88**. (2006) 073508

[2] Y. Sun, C. J. Takacs, S. R. Cowan, J. H. Seo, X. Gong, A. Roy & A. J. Heeger. Efficient, Air-Stable Bulk Heterojunction Polymer Solar Cells Using MoOx as the Anode Interfacial Layer. *Advanced Materials*. **23** (2011) 2226-2230

[3] D. C. Watters, J. Kingsley, H. Yi, A. Iraqi & D. Lidzey. Optimising the Efficiency of Carbazole co-polymer Solar Cells by Control Over the Metal Cathode Electrode. *Organic Electronics*. **13** (2012) 1401-1408

[4] M. C. Gwinner, R. D. Pietro, Y. Vaynzof, K. J. Greenberg, P. K. H. Ho, R. H. Friend & H. Sirringhaus. Doping of Organic Semiconductors Using Molybdenum Trioxide: a Qunatitative Time-Dependent Electrical and Spectroscopic Study. *Advanced Functional Materials*. **21** (2011) 1432-1441

[5] A.Z. Moshfegh & A. Ignatiev. Formation and Characterization of Thin Film Vanadium Oxides: Auger Electron Spectroscopy, X-ray Photoelectron Spectroscopy, X-ray Diffraction, Scanning Electron Microscopy, and Optical Reflectance Studies. *Thin Solid Films*. **198** (1991) 251-268

[6] Y. He & Y. Li. Fullerene Derivative Acceptors for High Performance Polymer Solar Cells. *Physical Chemistry Chemical Physics*. **13** (2011) 1970-1983

[7] K. Sugiyama, H. Ishii, Y. Ouchi & K. Seki. Dependence of Indium–Tin–Oxide Work Function on Surface Cleaning Method as Studied by Ultraviolet and X-ray Photoemission Spectroscopies. *Journal of Applied Physics*. **1** (2000) 295-298

[8] G. Greczynski, T. Kugler, M. Keil, W. Osikowicz, M. Fahlman & W. R. Salaneck.

Photoelectron spectroscopy of thin films of PEDOT–PSS conjugated polymer blend: a mini-review and some new results. *Journal of Electron Spectroscopy and Related Phenomena*. 121. (2001) 1-17

[9] D. R. Lide. *Handbook of Chemistry and Physics*. 79th edition. Boca Raton: CRC Press; 1998

Chapter 6

Solution Processing of Vanadium (V) Oxide

6.1 Introduction

Vanadium (V) Oxide has been shown to be an effective hole extraction layer within organic photovoltaic devices. However Vanadium (V) Oxide has severe limitations in comparisons to other metal oxides due to its high toxicity. Solution processed versions of Vanadium (V) Oxide could present an alternative means as the precursor compounds themselves may not be toxic. Vanadium (V) Isopropoxide is a solution processable form of Vanadium (V) Oxide where additional soluble side chains are added onto the oxygen atoms. This allows for the material to be processed in a wide range of solvents allowing for greater ease of processing upon multiple different surface types.

6.2 Thickness Dependence

Devices were fabricated by spin coating Vanadium (V) Isopropoxide in the organic solvent isopropyl alcohol at concentrations of 10mg.ml^{-1}, 5mg.ml^{-1} and 3mg.ml^{-1} in order to control the thickness of the deposited Vanadium (V) Oxide layer. The hole extraction layer was spun in atmosphere and then transferred to the glovebox in order to complete the device fabrication. In order to calibrate the thickness of the deposited Vanadium (V) Oxide films were spun at several spin speeds onto silicon and then measured via ellipsometry. The data points obtained were used to calculate the thickness by the spin-speed thickness relationship where the thickness is proportional to the inverse of spin speed squared.[1] **Figure 6.1** shows the thickness dependence on spin speed for several concentrations of Vanadium (V) Isopropoxide in isopropyl alcohol. From this data it is possible to determine the correct spin speed and solution concentration needed to deposited films with thicknesses between 20nm and 2nm.

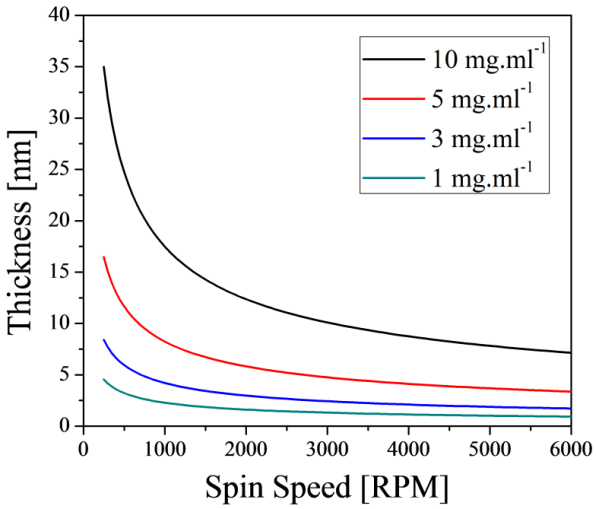

Figure 6.1 Thicknesses of Vanadium (V) Oxide as calculated by ellipsometry for different concentrations and spin speeds of solutions.

Spinning in atmosphere allows for the hydrolysis of the deposit vanadium Isopropoxide film, **Equation 6.1** shows the chemical reaction that occurs when vanadium Isopropoxide is exposed to air. Water itself undergoes constant splitting and reformation where it breaks into constituent OH^- and H^+ when a H^+ cation is present it causes the cleaving of the alkyl chain and binds with the singly bound oxygen present on the vanadium oxide. The OH^- anion then binds with the positively charged alkyl chain and isopropanol is formed, this then evaporates from the surface. The vanadium intermediary molecules then react releasing water and leaving behind Vanadium (V) Oxide.

$$2.OV(OCH(CH_3)_2)_3 + 6.H_2O \rightarrow 6.C_3H_7OH + 2.VO_4H_3 \qquad \textbf{Equation 6.1}a$$

$$2.VO_4H_3 \rightarrow V_2O_5 + 3.H_2O \qquad \textbf{Equation 6.1}b$$

Figure 6.2 shows the calculated optical properties of 15nm films of solution processed Vanadium (V) Oxide films. It can be seen that the absorption properties of these films vary in comparison to vacuum deposited versions, a higher transmittance is seen across the entire visible spectrum with films showing greater than 95% transmittance between 500nm and 1100nm. Similarly to vacuum deposited films there is an absorption peak observed at 400nm with the edge leading up to around 500nm this peak has a higher transmission of 85% in comparison to 40% for vacuum deposited films. In addition the refractive index observed is lower than that for vacuum deposited films. This combination of observed optical characteristics for solution processed Vanadium (V)

Oxide point towards a film similar to that of vacuum deposited Vanadium (V) Oxide but of lower density. [2]

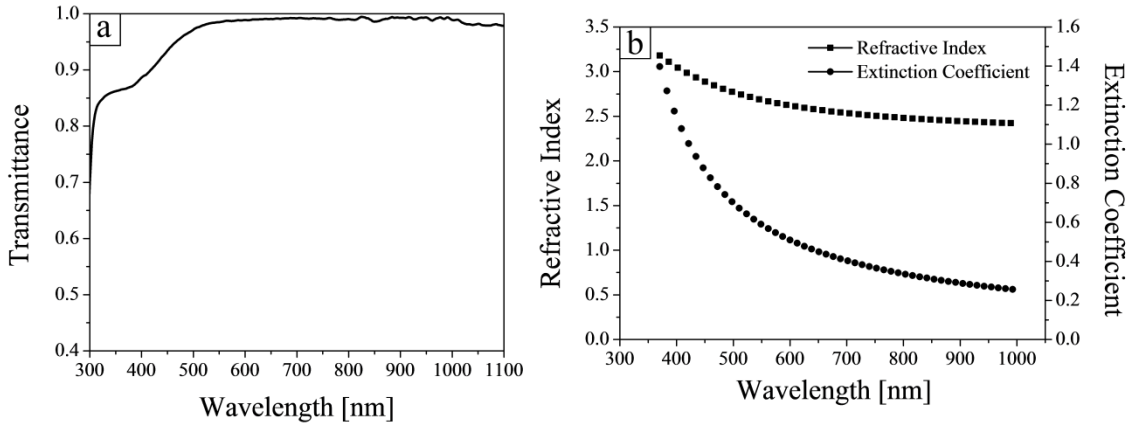

Figure 6.2 Shows optical spectroscopy data for solution deposited Vanadium (V) Oxide films with (a) transmittance data obtain from absorption spectroscopy and (b) ellipsometry data calculating the refractive index and extinction coefficient of the deposited film.

Figure 6.3 shows performance parameters for devices fabricated with Vanadium (V) Oxide layers with thicknesses varying from 12nm to 2nm. It can be seen that the highest contribution to the change in PCE is due to the large variations observed in the J_{sc} generated by the devices with varying thicknesses. As there is no variation in the V_{oc} when the film tends towards 2nm in thickness it can be assumed that surface coverage of the ITO remains complete. In addition the electronic interactions at the interface between the anode and the organic layer will be due to PCDTBT and Vanadium (V) Oxide. As the film becomes thinner the absorption of light as it passes through the

Vanadium (V) Oxide will reduce, the reduction in J_{sc} opposes this and the likely reason for a reduction in J_{sc} is from the Vanadium (V) Oxide acting as an optical spacer. As organic layer thickness is fixed at approximately 55nm adding an optical spacer layer will alter the optimal thickness of the organic active layer, this will shift towards a thinner film. This shift in optimal active layer thickness due to the thickness of the optical spacer layer is one of the reasons for the drop in J_{sc} for thicker films; in addition the optical properties determined via ellipsometry indicate that the material has a short bandgap of approximately 2.6eV this is close to the range of values reported in literature.[3,4] This gives it some absorption in the blue region of the spectra where a portion of the light harvest by the donor material is, this in effect reduces the intensity of light within the organic layer.

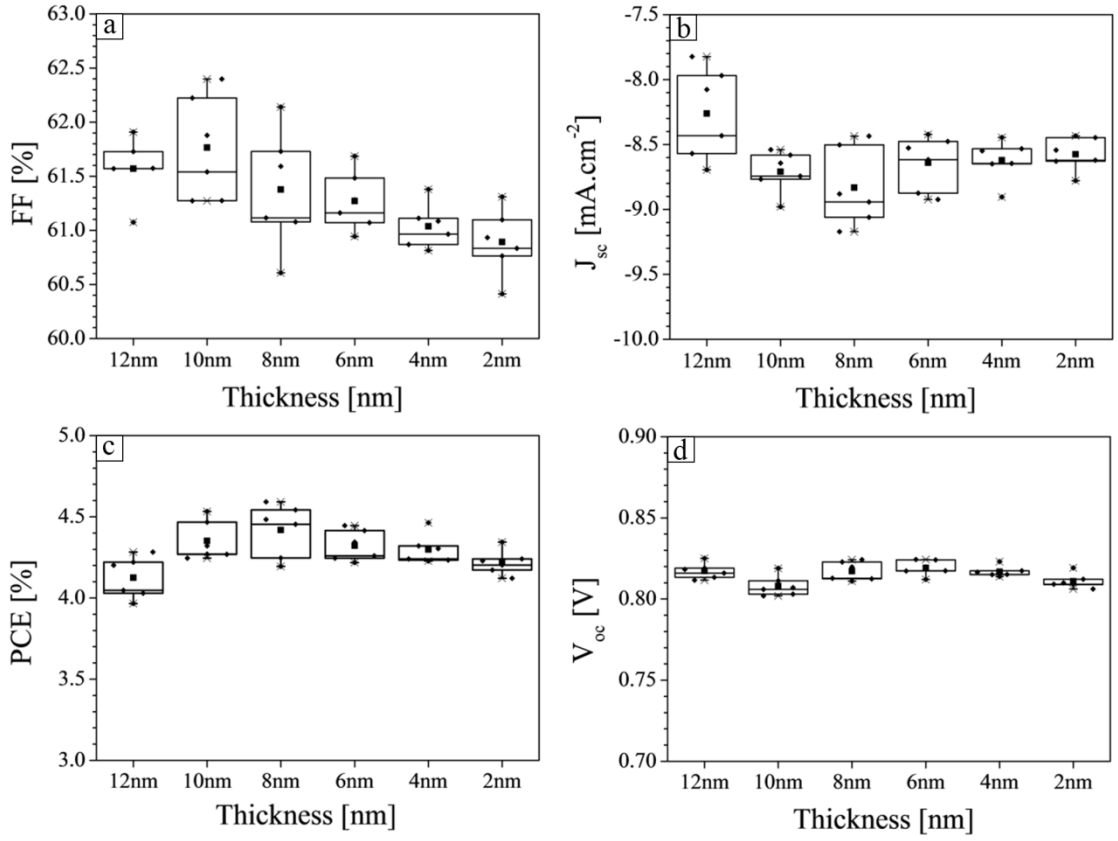

Figure 6.3 Comparison of performance parameters for OPV's using solution processed Vanadium (V) Oxide with varying film thicknesses. Where the performance parameters are (a) Fill Factor, (b) Short Circuit Current, (c) Power Conversion Efficiency, and (d) Open Circuit Voltage.

6.3 Atmospheric Dependence

In order to reduce both the cost and the inbuilt energy of organic photovoltaic devices the solution processed layers ideally need to be deposited within atmospheric conditions without losing the high performances obtained in inert atmospheres. Comparisons of devices fabricated within an inert atmosphere and for devices fabricated in air using optimum thicknesses of Vanadium (V) Oxide layer have been done. **Figure 6.4** shows

the results for devices with the hole extraction layer spun in atmospheric conditions and those spun in air. For all device parameters a reduction is observed for those fabricated within the inert nitrogen glovebox, the average values for the FF, J_{sc}, PCE and V_{oc} drop from 58%, -10.2mA.cm^{-2}, 4.9%, and 0.85V for atmosphere deposited films to 48%, -9.0mA.cm^{-2}, 2%, and 0.46V for glovebox deposited films. This is a significant reduction in performance and the ability to determine the cause of this difference is difficult as many techniques that would measure changes within the films properties, such as AFM, XPS, UPS, and UV-Vis spectroscopy, require exposure to atmospheric conditions. Vanadium (V) Isopropoxide and many similar metallic Isopropoxides undergo hydrolysis in which exposure to water causes the breakdown of the Isopropoxide molecule. Upon hydrolysis Vanadium (V) Oxide remains along with isopropyl alcohol created via the hydrolysis reaction, this then evaporates from the film. In the inert atmosphere in the glovebox the presence of water is limited to below 0.1ppm, this means that the amount of water available for hydrolysis is limited. It has been shown that the electronic structure of Vanadium (V) Isopropoxide before hydrolysis exhibits a metallic structure with occupation of the V3d orbital.[5] In its oxidized form Vanadium has no electrons occupying the V3d orbital and the highest occupied orbital is that of O2p, this results in a deep valence band for fully oxidized films with the Fermi level pinned below the empty V3d orbital. If hydrolysis does not occur the Fermi level will be situated above the V3d orbital leading to a much shallower work function. This shallow work function for films spun within the inert atmosphere of the glovebox explains why there is such a large difference in the performance as there would likely be a large interfacial barrier for hole extraction between the Vanadium (V) Isopropoxide and the PCDTBT. These results therefore indicate that the processing of

the Vanadium (V) Oxide interface requires the presence of a significant amount of water for the film to fully undergo hydrolysis.

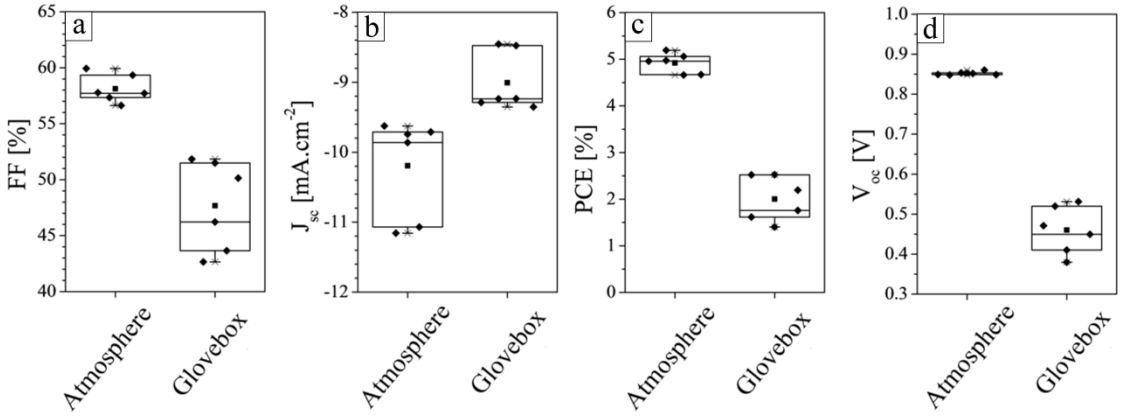

Figure 6.4 Comparison of performance parameters of OPV's where the Vanadium (V) Oxide films are deposited in different atmospheres. Where the performance parameters are (a) Fill Factor, (b) Short Circuit Current, (c) Power Conversion Efficiency, and (d) Open Circuit Voltage.

6.4 Temperature Dependence

Most forms of solution processable metal oxides require post deposition annealing in order to achieve fully stoichiometric oxides. Devices were fabricated with 8nm thick Vanadium (V) Oxide layers annealed at temperatures ranging from 100^{o}C to 400^{o}C and compared against unannealed devices. Figure 6.5 shows AFM images of the deposited Vanadium (V) Oxide films annealed at different temperatures, for all deposited films high surface uniformity is observed over 5µm X 5µm scans. The RMS roughness of bare ITO is 2.6nm upon deposition of the Vanadium (V) Oxide layer the RMS

roughness increases to approximately 3.5nm. The RMS roughness stays the same for films until they are annealed up to 200°C and above, after this the RMS roughness drops from 3.5nm to 2.7nm. It can be observed that as the annealing temperature increases that the underlying structure of the ITO becomes more visible this would indicate that a reduction in the thickness of the deposited layer is occurring.

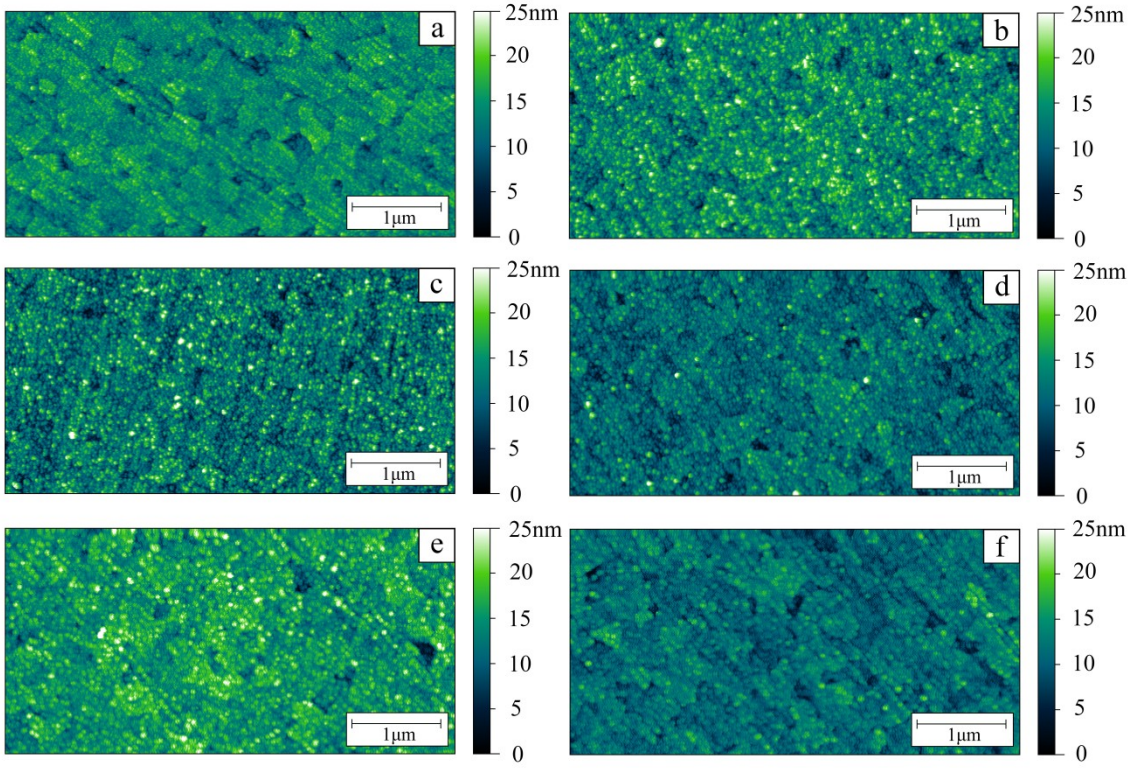

Figure 6.5 AFM images of the surfaces of (a) ITO, (b) unannealed films of Vanadium (V) Oxide films and ((c), (d), (e) and (f)) Vanadium (V) Oxide films annealed at 100°C, 200°C, 300°C and 400°C respectively.

Figure 6.6 shows electron spectroscopy data for Vanadium (V) Oxide unannealed films and films annealed at temperatures ranging from 200°C and 400°C. **Figure 6.6**a shows

that for all samples the Vanadium 2p peak has two different species present these have been attributed to the fully oxidised state V^{5+} and the reduced state V^{4+}. Upon annealing the amount of reduced states V^{4+} increases however no reduced metallic states are present. **Figure 6.6**c shows that UPS spectra for films annealed at temperatures below 300^{o}C are fixed and that the work function of the deposited layer is approximately -5.5eV upon annealing at temperatures of 300^{o}C and higher the work function shifts to lower binding energies. The position of the valence band remains constant and there is no significant emission from states close to the valence band indicating that the film still has a true bandgap.

	No Anneal	**200°C**	**300°C**	**400°C**
H_2O	7%	8%	12%	11%
OH^-	46%	52%	50%	55%
V-O	47%	40%	38%	34%
V^{5+}	85%	78%	74%	72%
V^{4+}	15%	22%	26%	28%
Fermi Level	-5.51eV	-5.46eV	-5.4eV	-5.25eV
Valence Band	-7.78eV	-7.75eV	-7.75eV	-7.76eV

Table 6.1 Percentage abundance of different chemical states present in the O1s scans and V2p scans along with Fermi level and valence band positions derived from UPS spectra.

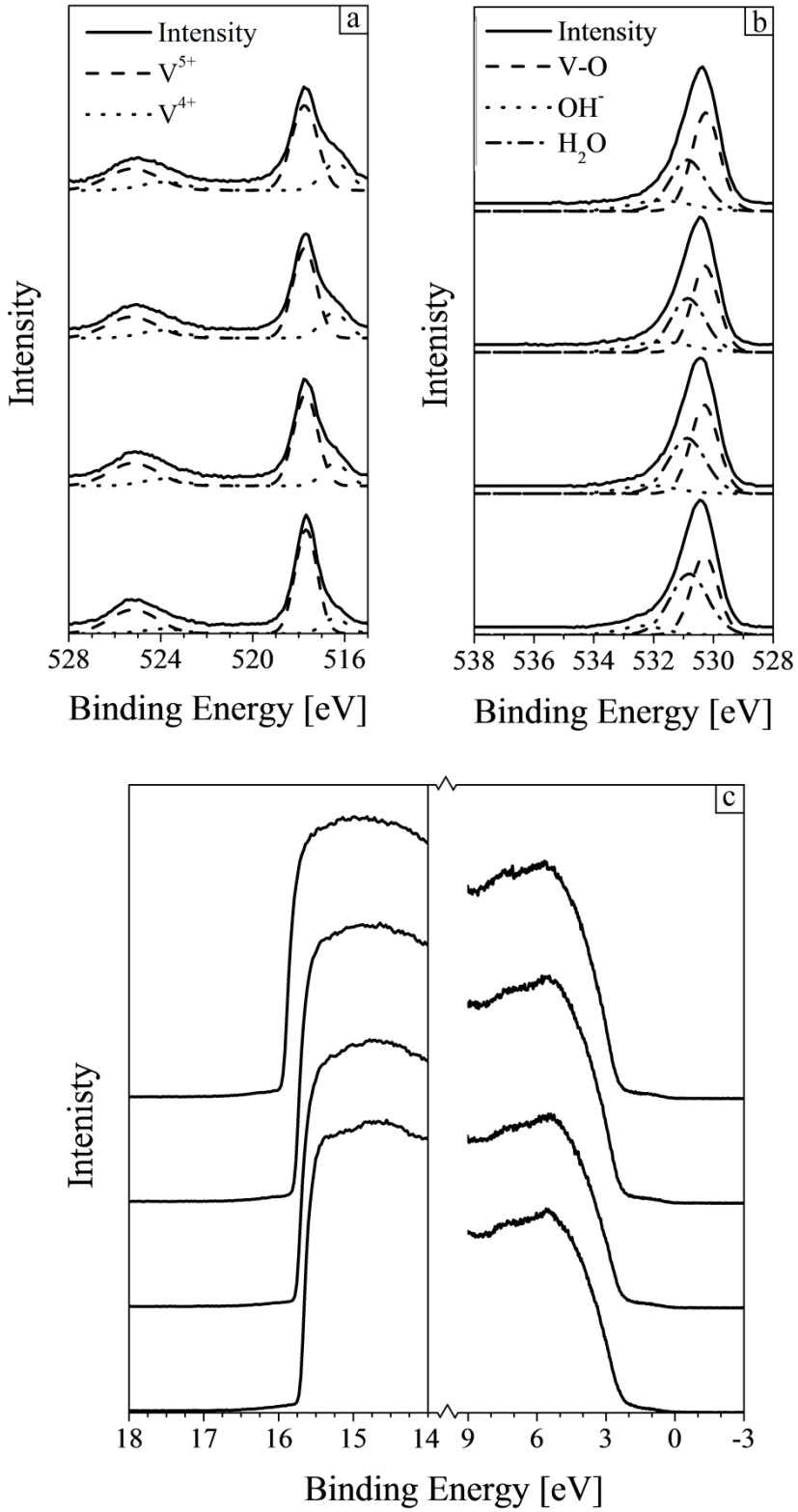

Figure 6.6 Photoelectron spectroscopy data of thermally annealed Vanadium (V) Oxide films where (a) is the V2p spectra, (b) O1s spectra and (c) UPS spectra.

Figure 6.7 shows device data obtained for OPV's fabricated with Vanadium (V) Oxide films thermally annealed at different temperatures. A decline in the average PCE is observed between unannealed films and those annealed at 200^{o}C however this decline is not statistically significant. Upon annealing at temperatures of 300^{o}C and above the performance of the devices shows a significant decline from an average PCE of 4.2% at 200^{o}C to 3.1%. This drop in efficiency is driven by a decrease in all device parameters with a significant drop in the V_{oc} from 0.77V to 0.63V, from the UPS results annealing at temperatures of 300^{o}C and higher causes the work function to drop from –5.5eV to -5.2eV this reduction in work function will induce contact barriers. The formation of contact barriers lead to drops in all device parameters due to increased series resistance. The reason for the drop in work function observed is not due to the formation of metallic states within the film, however it has been observed in other work that annealing metal Isopropoxide films at high temperatures can lead to changes in the crystalline structure.[6] Work function itself is a surface property and can vary due to crystalline orientation, if changes to the crystalline structure are occurring this could lead to changes in the work function.[7] Device data therefore indicates that the major effect of annealing major is the reduction of the work function of the material and that there is no observable advantage of annealing films post deposition.

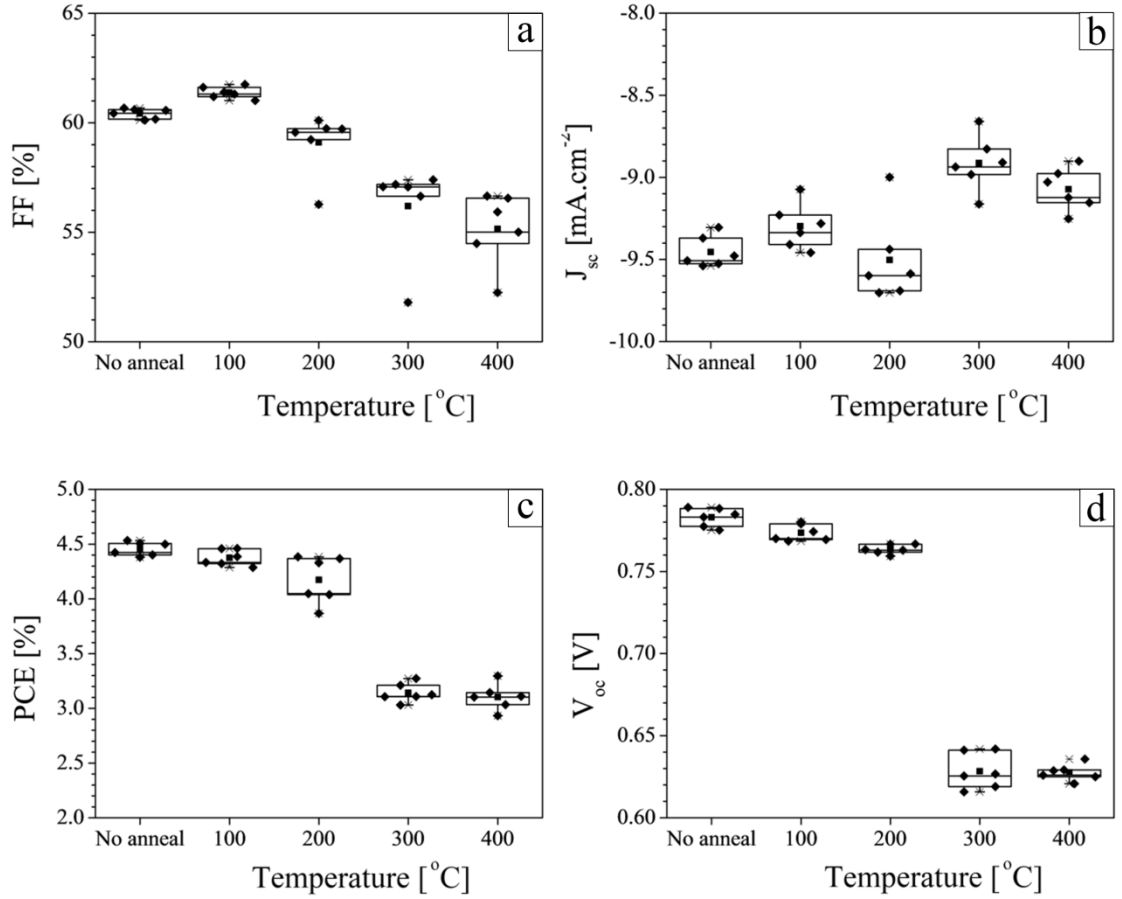

Figure 6.7 Comparison of performance parameters of OPV's where the Vanadium (V) Oxide films are thermally annealed at different temperatures. Where the performance parameters are (a) Fill Factor, (b) Short Circuit Current, (c) Power Conversion Efficiency, and (d) Open Circuit Voltage.

6.5 Comparisons against other materials

In order to determine how effective solution processed vanadium (V) Oxide is within organic photovoltaic devices it has been compared against both vacuum evaporated Vanadium (V) Oxide and also the current benchmark hole extraction material PEDOT:PSS. **Figure 6.8** shows how the various device characteristics vary for each of

the different hole extraction layers. ITO alone produces poor device results with average efficiencies of around 1% this is due to the shallow work function of approximately -4.5eV for ITO.[8] This leads to non-ohmic contact resulting in extraction barriers and increased series resistance within the device. PEDOT:PSS, Vacuum evaporated Vanadium (V) Oxide and solution processed Vanadium (V) Oxide all show device performance that are comparable. It should be noted that a larger deviation in the measured parameters is observed for films that have been solution processed. Vacuum evaporation allows for high uniformities across the substrate, solution processing however is a highly dynamic process where thickness variations are observed across the length of the substrate. These changes in thickness are the likely cause of differences in the deviations of device results between the vacuum evaporated Vanadium (V) Oxide films and the solution processed PEDOT:PSS and Vanadium (V) Oxide.

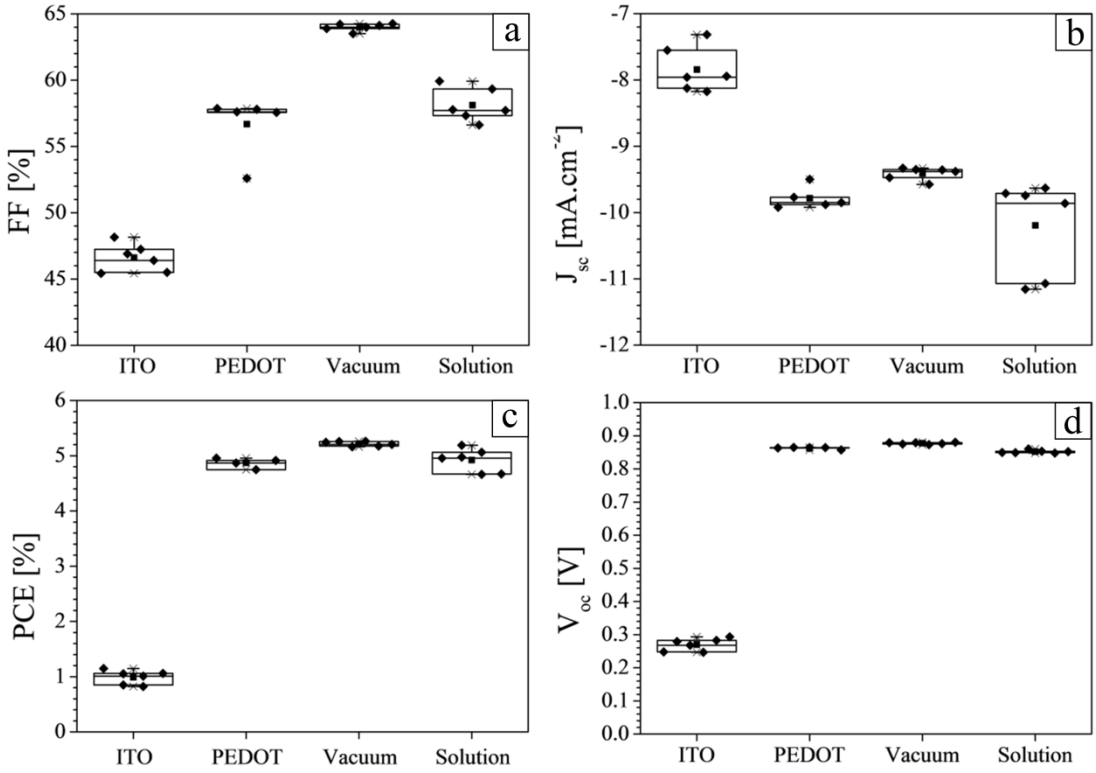

Figure 6.8 Comparison of performance parameters for OPV's fabricated with various optimized hole extraction layers. Where the performance parameters are (a) Fill Factor, (b) Short Circuit Current, (c) Power Conversion Efficiency, and (d) Open Circuit Voltage.

6.6 Conclusion

It has been shown that it is possible to fabricate OPV's with the use of a solution processable form of Vanadium (V) Oxide called Vanadium (V) Isopropoxide. These devices were fabricated at low temperatures under atmospheric conditions without leading to a reduction in device performance in comparison to vacuum evaporated Vanadium (V) Oxide. It is observed that in order to obtain high performance devices the

deposited Vanadium (V) Isopropoxide must be exposed to water in order for hydrolysis of the deposited material to occur. This reaction leads to the formation of Vanadium (V) Oxide films with Isopropyl alcohol as the waste product of the reaction which rapidly evaporates from the thin films due to its low boiling point. Further annealing of films leads to no significant change in the device performance for temperatures below 300^{o}C above this point reduction in the work function of Vanadium (V) Oxide occurs, leading to reductions in the performance due to extraction barriers that form at the PCDTBT Vanadium Oxide interface.

6.7 References

[1] A. G. Emslie, F. T. Bonner & L. G. Peck. Flow of Viscous Liquids on a Rotating Disk. *Journal of Applied Physics*. **29** (1958) 858-862

[2] E. F. Schubert, J. K. Kim & J. Q. Xi. Low-Refractive-Index Materials: A New Class of Optical Thin-Film Materials. *Physica Status Solidi B*. **244** (2007) 3002-3008

[3] M. Benmoussa, E. Ibnouelghazi, A. Bennouna & E. L. Ameziane. Structural, Electrical and Optical Properties of Sputtered Vanadium Pentoxide Thin Films. *Thin Solid Films*. **265** (1995) 22-28

[4] Z. S. El Mandouh & M. S. Selim. Physical Properties of Vanadium Pentoxide Sol-Gel Films. *Thin Solid Films*. **371** (2000) 259-263

[5] I. Novak & B. Kovac. Polyoxometalates and Vanadium Alkoxides: Electronic Structure and Properties. *Chemical Physics Letters*. **474** (2009) 33-35

[6] S. Mahshid, M. Askari & M. S. Ghamsari. Synthesis of TiO_2 Nanoparticles by Hydrolysis and Peptization of Titanium Isopropoxide Solution. *Journal of Materials Processing Technology*. **189** (2007) 296-300

[7] H. Ishii, K. Sugiyama, E. Ito & K. Seki. Energy Level Alignment and Interfacial Electronic Structure at Organic/Metal and Organic/Organic Interfaces. *Advanced Materials*. **11** (1999) 605-625

[8] Y. Park, V. Choong, Y. Gao, B. R. Hsieh & C. W. Tang. Work Function of Indium Tin Oxide Transparent Conductor Measured by Photoelectron Spectroscopy. *Applied Physics Letters*. **68** (1996) 2699-2701

Chapter 7

Spray Coated Molybdenum (VI) Oxide

7.1 Introduction

Several factors affect the overall viability of organic photovoltaics as a solution to the production of clean energy. Among these the most important are the monetary cost and the energy cost in the production of these devices. In order to allow organic photovoltaics to accomplish this, high throughput using low energy deposition techniques are needed. Processing under vacuum or at high temperatures is therefore not an acceptable method of depositing materials. Current methods of depositing hole extraction layers made from Molybdenum (VI) Oxide are involve both high temperatures and vacuum.[1,2] In the previous chapter work on a solution processable version of Vanadium (V) Oxide showed that it is possible to replace vacuum evaporated films with solution processed versions without compromising performance. In this chapter work has been carried out using Ammonium Molybdate Tetrahydrate which has been shown previously to work at low temperatures.[1] This work looks at depositing both the hole extraction layer and the organic active layer without any post deposition treatment using ultrasonic spray coating a roll-to-roll compatible technique.

7.2 Studying the Properties of the Deposited Films

In **Chapter 7.3** organic photovoltaic device results are shown for device fabricated using molybdenum oxide hole extraction layers deposited via vacuum evaporation, reactive sputtering and solution processing with several different post deposition thermal annealing temperatures. In order to understand and discuss the results obtained from these devices information on what is happening to the deposited molybdenum oxide layers needs to be given first. Several techniques have been undertaken in order to characterise how the thermal annealing step affects the deposited molybdenum oxide. Initial analysis of the films was focused upon observing any possible changes in the chemical and electronic structure of the deposited films through X-ray Photoelectron Spectroscopy (XPS) and Ultraviolet Photoelectron Spectroscopy (UPS). **Figure 7.1** to **Figure 7.5** shows variations in (a) O1s spectra, (b) N1s spectra, (c) Mo3d spectra and (d) UPS scans with an enhanced view of the valence band region for unannealed films and those annealed at 200^{o}C, 300^{o}C, 350^{o}C and 400^{o}C. The background intensity for all high resolution scans was calculated using a Shirley background substitution. Wide scans for all the samples show large amounts of Nitrogen, Molybdenum, Oxygen and Carbon with no trace of contamination from other sources.

Mo3d scans show the presence of two different species of molybdenum within the films these are attributed to Mo^{6+} and Mo^{5+} oxidation states. In transition metal oxides the higher the oxidation state the more electrons are donated to O2p orbitals, this loss of electron density around the molybdenum atom results in higher binding energies for electrons that remain in molybdenum atomic orbitals. It can be seen that the percentage concentration of the reduced Mo^{5+} state increases as the films are annealed. For unannealed films the concentration of Mo^{5+} states present are 1.5%, upon annealing

at 200°C the concentration of Mo^{5+} increases by a small amount to 1.7%. This reduction in oxidation state is due to the decomposition of Mo^{6+} Oxide at high temperatures. The sample annealed at 300°C shows a significant increase in the presence of these reduced Molybdenum Oxide states to 9.7%, further annealing at 350°C and 400°C does not lead to an increase and the concentration of Mo^{5+} states are 7% and 7.9% respectively. It should be noted that the standard deviation between the fitted peaks and the measured spectra is below 5 for all scans indicating high fitting accuracy. The concentration of reduced states within vacuum evaporated films as seen in XPS scans in **Chapter 5.1** is 5.4% while for films sputtered at 25% oxygen concentration as seen in XPS scans in **Chapter 8.5** is 10.8%, for these films the performance of devices fabricated with them are nearly identical.

N1s scans incorporate both chemical states associated with Nitrogen species (409.9eV) and also those from Molybdenum due to the close proximity of the Mo3p peak (411.6eV to 394eV).[2] Oxidized Molybdenum as seen within the samples has the possibility of the Mo3p peak overlapping nitrogen species within the N1s spectra, however due to the high oxidation state of the molybdenum oxide the peaks associated with Mo3p are shifted to energy levels higher than the N1s peak. The two peaks fitted in the N1s spectra are associated with ammonium (NH_4^+) that is present within the Ammonium Molybdate Tetrahydrate and nitrogen gas (N_2) that has absorbed into the film from the surrounding environment. Assignment of the small peak is due to the positively charged Nitrogen atom that leads to an increased binding energy. The assignment of molecular Nitrogen to the secondary peak is due to the high content of nitrogen within the sample preparation atmosphere allowing for the absorption of the gas into the film. For unannealed samples the intensity of the peak associated with

Ammonium is 16.8% of the total intensity of the N1s spectra upon annealing at the different temperatures the intensity of this peak drops to 12.8%, 8.7%, 8.1% and 4% respectively. This drop in intensity is due to the de-sorbtion of trapped ammonium present within all the films upon deposition.

O1s spectra recorded for samples annealed at different temperatures show the presence of three different chemical states of oxygen. The highest binding energy state is associated with water (H_2O) due to Oxygen within water has a small dipole negative dipole due to the high electronegativity of oxygen reducing the binding energy in comparison to molecular oxygen. The next lowest binding energy peak is associated with the formation of metal hydroxides (OH^-) the negative charge of the molecule is localised to the oxygen making the oxygen binding energy lower than for oxygen within water. The last peak in the O1s spectra is that for Oxygen bound to Molybdenum (ie. MoO); the bond between Molybdenum and Oxygen results in the donation of an electron from the Molybdenum 4d or 5s orbital to the O2p orbital. Oxygen will then have a charge of -2e leading to a further decrease in the binding energy of the electrons within Oxygen's orbital. Across all the different annealing conditions the abundance of the peaks with relation to each other does not change. One outcome of this is that annealing does not lead to a change in the absorbed water at the films surface; absorption of water can cause changes in the electronic structure of the film by altering the cluster size of Molybdenum Oxide.[3] The Molybdenum hydroxide peak shows good agreement with the Molybdenum 3d spectra due to the fact that no metallic states are induced by the annealing process. If metallic states are present this would allow for electrons to be redistributed through the Mo4d conduction band leading to a formation of a surface dipole and the ionic binding of more hydroxide groups at the surface.

UPS spectra showing both the secondary electron cut-off and valence band region give information on the position of the Fermi level for deposited film and also the position of the valence band. The position of the secondary electron cut-off for the different annealing conditions shows a variation between 16eV and 16.1eV however this does not correlate with the change in annealing temperature. In addition the error associated with the determination of the secondary electron cut-off is ±0.1eV making the difference in the secondary electron cut-off between the samples within experimental error. The Fermi level is then from the energy of the incoming UV photon and the secondary electron cut-off and is shown, for the deposited films, to be on average -5.04eV ±0.1eV. The valence band of the deposited layer varies from 2.97eV below the Fermi level for unannealed films to 2.89eV below the Fermi level for films annealed at 400^{o}C. Once again this variation is within experimental error for UPS therefore no observable change in the position of the valence band in relation to the Fermi level is observed. From both UPS scans it is possible to say that there is no change in the electronic structure of the deposited film that could be the cause of the change in device performance.

From the combination of both XPS and UPS data it is clear that the annealing of the solution processed molybdenum Oxide layer does not lead to any significant change in the chemical or electronic structure of the deposited layers that could result in changes in device performance. The only notable change in the films seen through these techniques is the reduction in the trapped ammonium within the film, this occurs due to the dissolving of ammonium in water allowing for the evaporation of ammonia. Tabulated data for all the photoelectron spectroscopy scans are shown in **Table 7.1**.

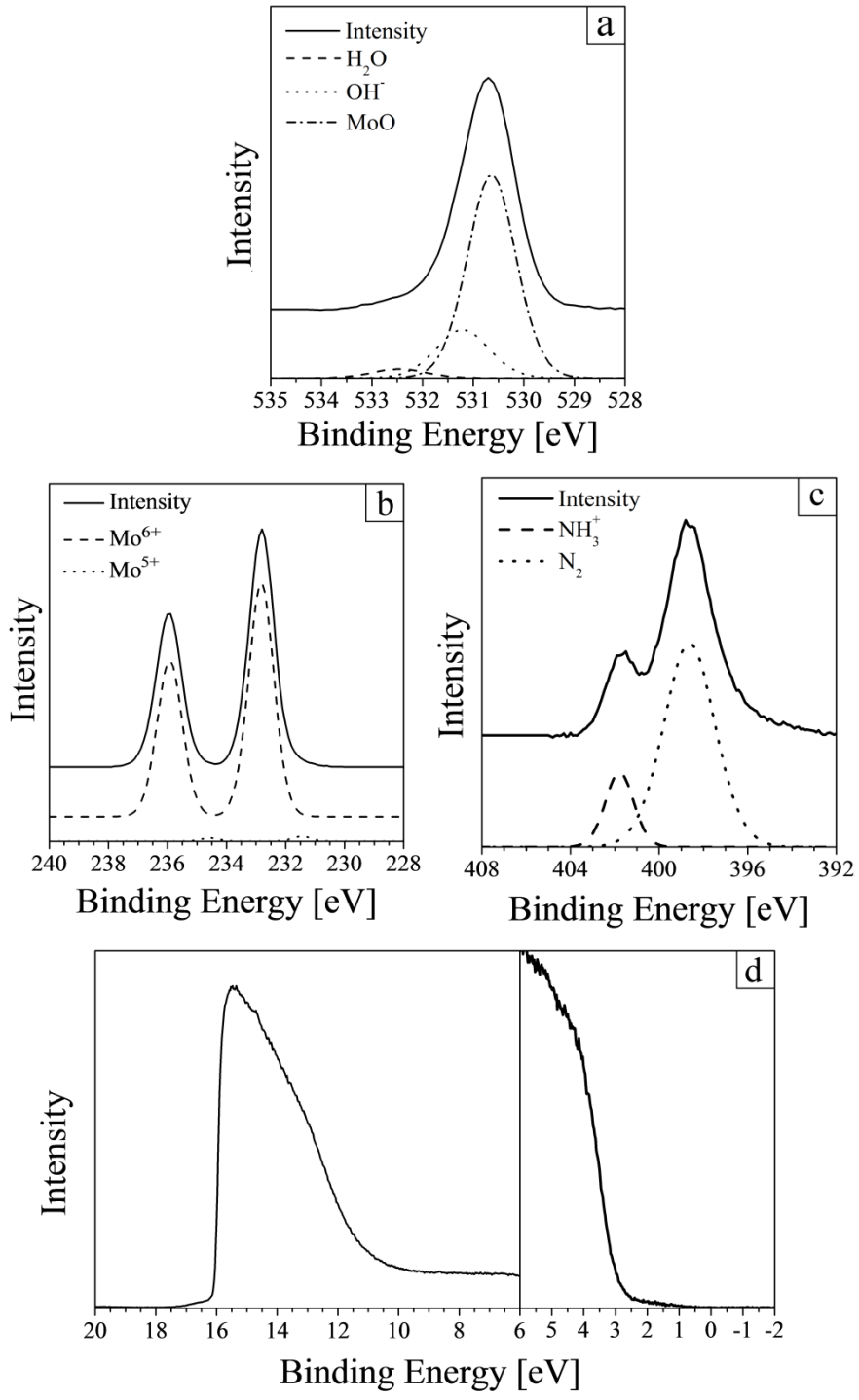

Figure 7.1 Photoelectron Spectroscopy scans of unannealed solution processed Molybdenum Oxide showing (a) O1s, (b) Mo3d, (c) N1s, (d) UPS scans with an enhanced valence region.

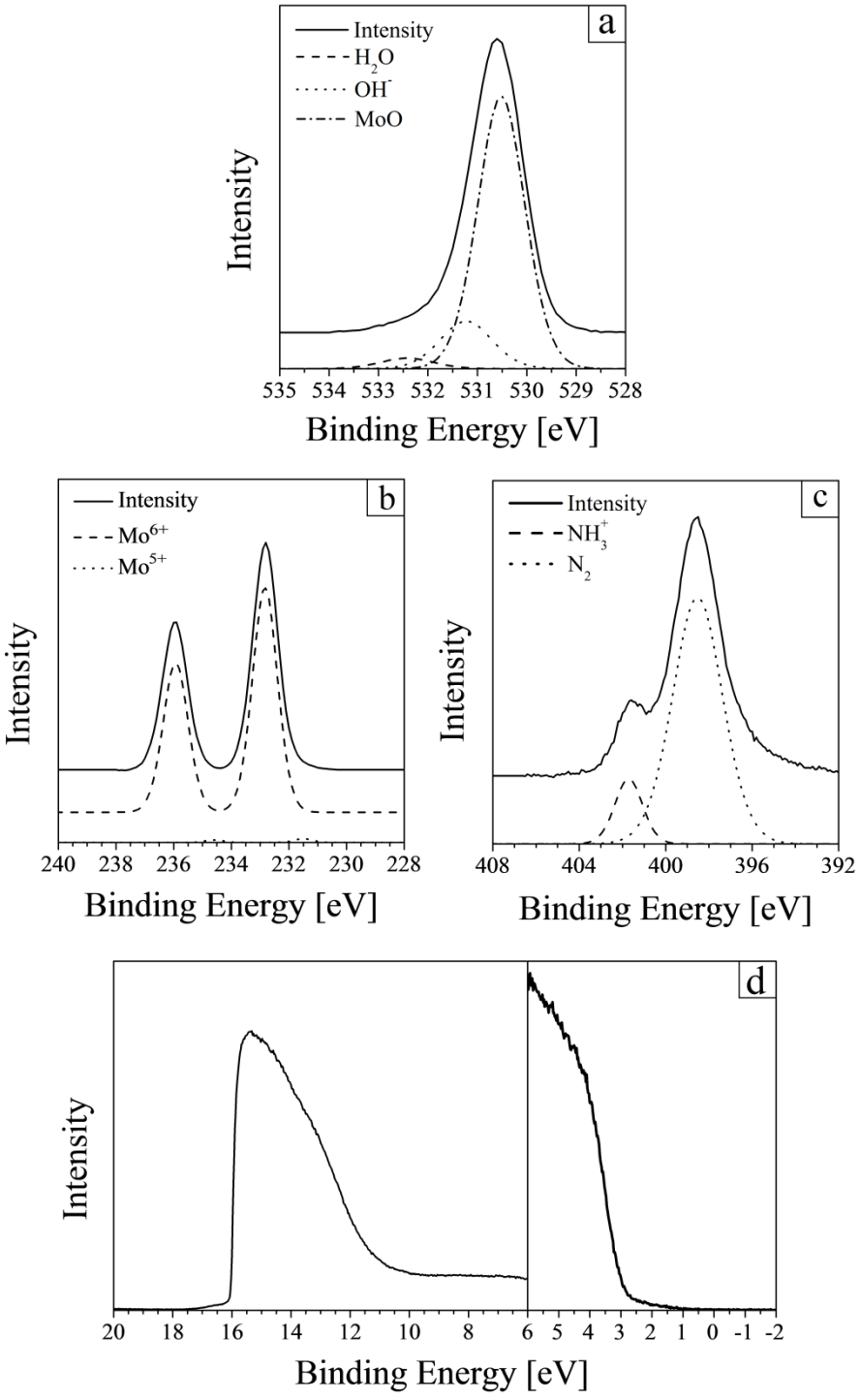

Figure 7.2 Photoelectron Spectroscopy scans of solution processed Molybdenum Oxide annealed at 200^{o}C showing (a) O1s, (b) Mo3d, (c) N1s, (d) UPS scans with an enhanced valence region.

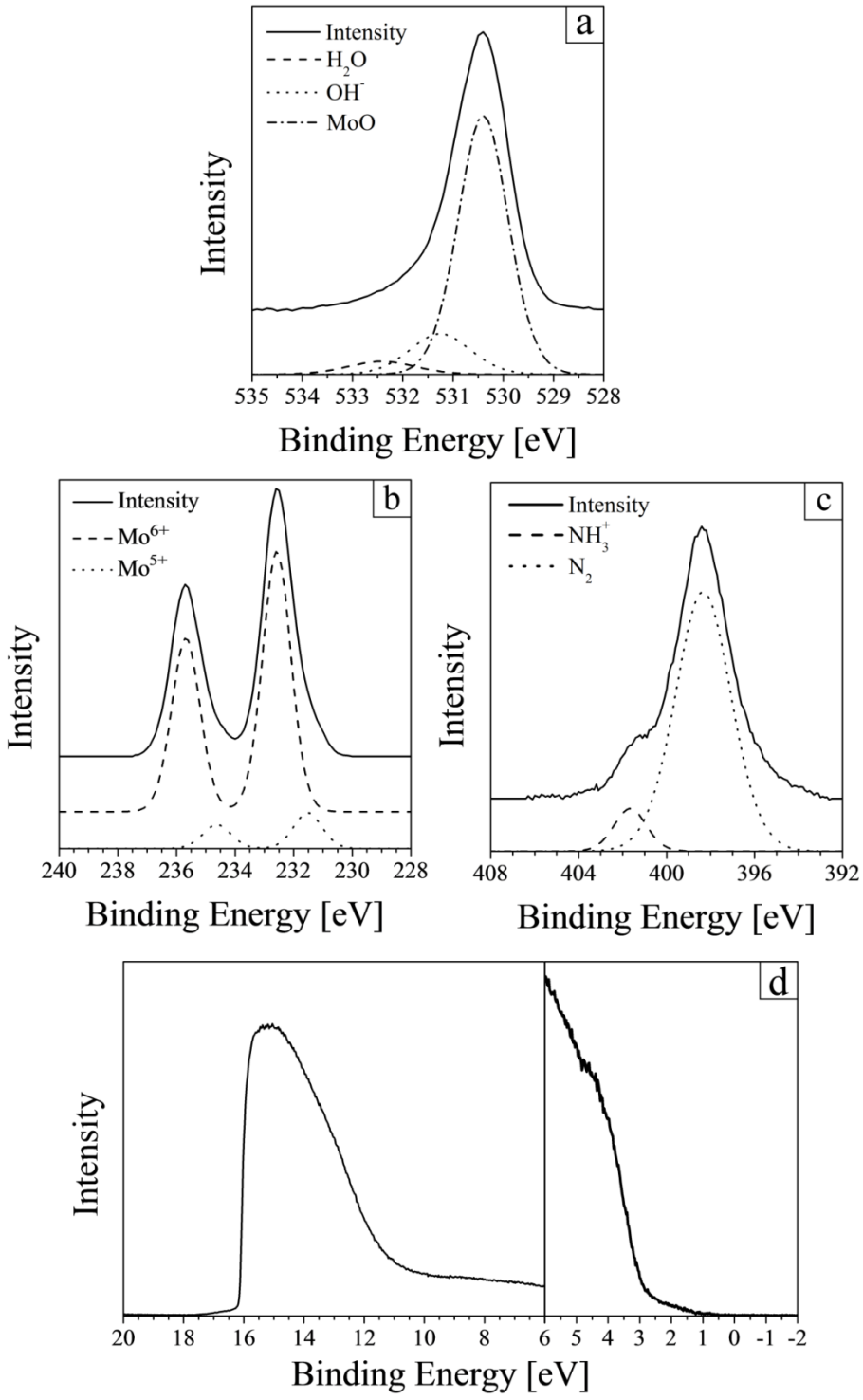

Figure 7.3 Photoelectron Spectroscopy scans of solution processed Molybdenum Oxide annealed at 300^{o}C showing (a) O1s, (b) Mo3d, (c) N1s, (d) UPS scans with an enhanced valence region.

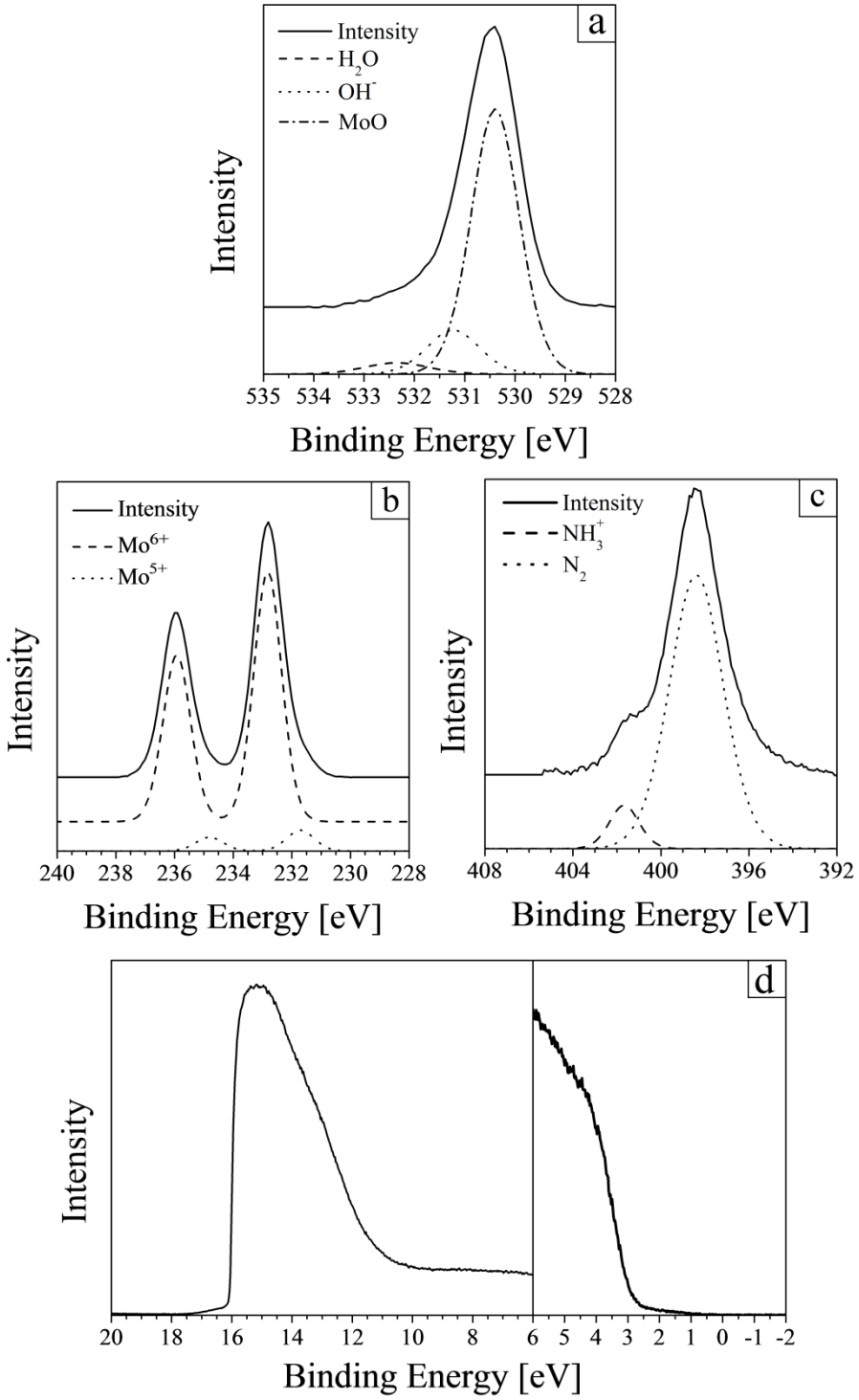

Figure 7.4 Photoelectron Spectroscopy scans of solution processed Molybdenum Oxide annealed at 350^{o}C showing (a) O1s, (b) Mo3d, (c) N1s, (d) UPS scans with an enhanced valence region.

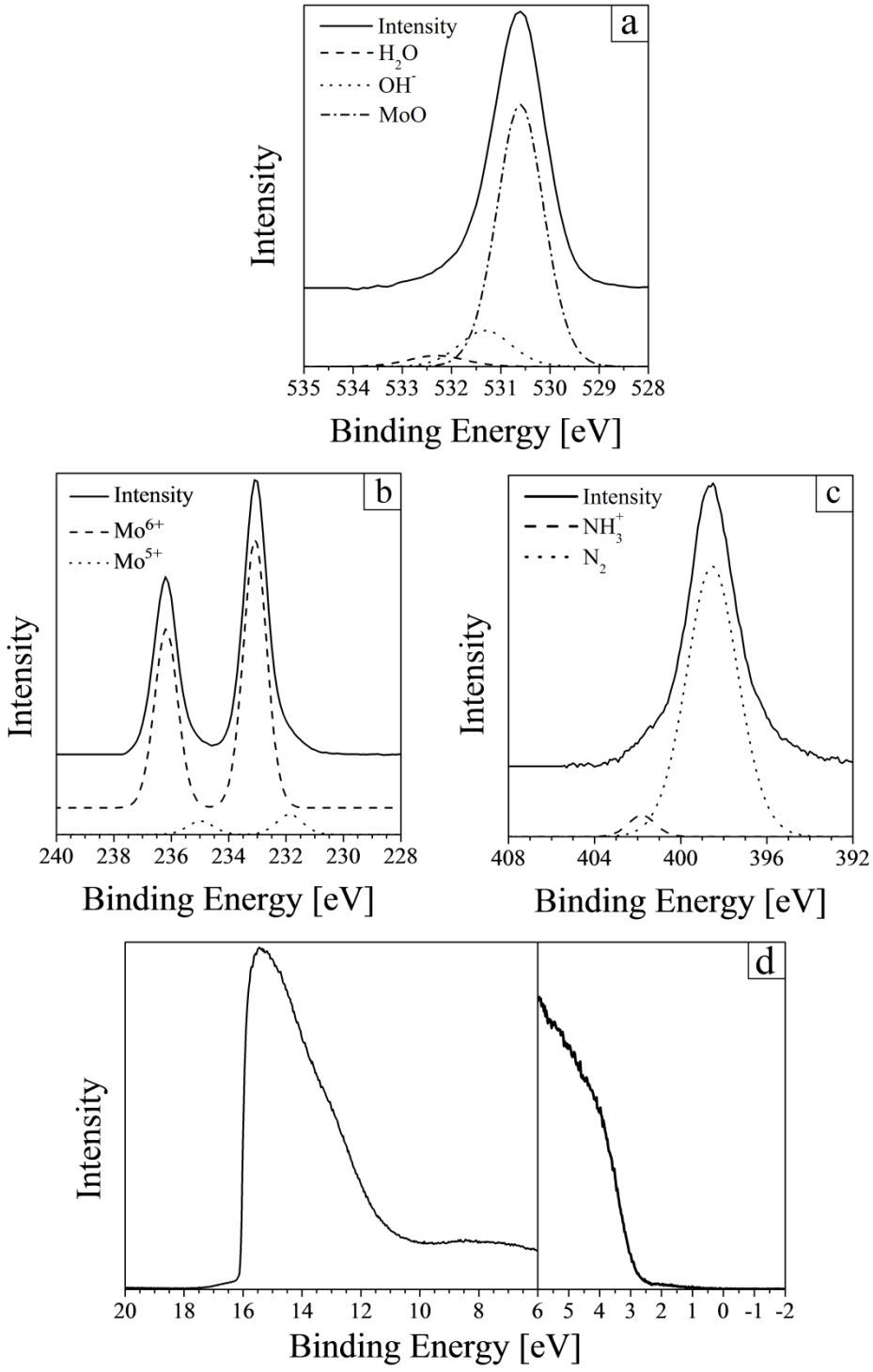

Figure 7.5 Photoelectron Spectroscopy scans of solution processed Molybdenum Oxide annealed at 400^{o}C showing (a) O1s, (b) Mo3d, (c) N1s, (d) UPS scans with an enhanced valence region.

		No Anneal	200°C	300 °C	350 °C	400 °C
Mo3d	Mo^{6+}	98.5%	98.3%	90.3%	93%	92.1%
	Mo^{5+}	1.5%	1.7%	9.7%	7%	7.9%
O2p	H_2O	3.8%	3.6%	5.4%	4.7%	4.1%
	OH^-	20%	15.6%	15.1%	14.8%	12.7%
	MoO	76.2%	80.8%	79.5%	80.5%	83.2%
N1s	NH_4^+	16.8%	12.8%	8.7%	8.1%	4%
	N_2	83.2%	87.2%	91.3%	91.9%	96%
UPS	Fermi	-5.15eV	-5.18eV	-5.09eV	-5.16eV	-5.13eV
	Valence	-8.12eV	-8.13eV	-8.11eV	-8.05eV	-7.98eV

Table 7.1 Tabulated data for the different photoelectron spectroscopy scans of solution processed molybdenum oxide films under different annealing conditions.

Figure 7.6 shows images obtained by Atomic Force Microscopy (AFM) for a 20μm x 20μm scan; unnanealed films show high surface uniformity with the RMS roughness of the sample being approximately 0.8nm with a peak to peak roughness of 13nm. The underlying ITO typically shows an RMS roughness of 2.6nm as seen in **Chapter 6.4** indicating that the addition of the solution processed molybdenum oxide leads to a smoothening of the contact between the electrode and the organic layer. This planarization has been reported to lead to improvements in device performance due to the reduction in possible shorts through the device.[4] Upon annealing of the films at 200°C and 300°C a slight increase in the surface roughness is observed with an RMS roughness for the films of 1.4nm and 1.6nm respectively. The active layer that is

deposited onto the Molybdenum Oxide layer is approximately 80nm; the change in the RMS roughness between as-sprayed films and those annealed at 300^{o}C is approximately 1% of the active layer thickness. This is extremely small increase and the likelihood of inducing shorts due to the roughening of the surface via annealing is minimal. Upon increasing the annealing temperature to 400^{o}C the RMS roughness of the film rises to 6.9nm and the films can be seen to undergo crystallization. These crystallized regions show large differences in the height in comparison to the surrounding material. The variation in height is on the same order as the thickness of the deposited active layer this will likely lead to paths for shorts to form between the anode and cathode. With the formation of short pathways through the organic layer reductions in the V_{oc} and J_{sc} are likely to be observed due to the increased charge carrier recombination and shunt current.

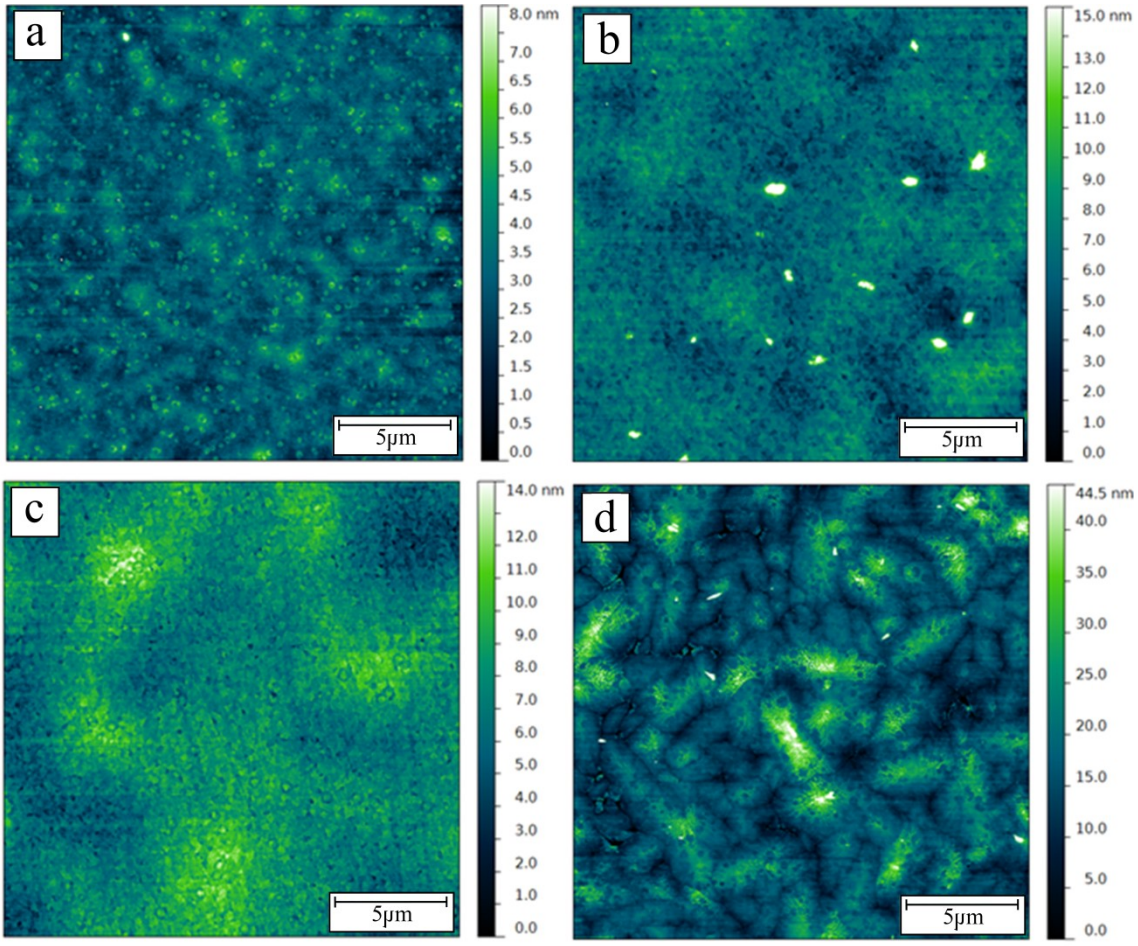

Figure 7.6 20µm x 20µm AFM scans of the deposited Ammonium Molybdate Tetrahydrate for (a) no annealing, (b) 200^{o}C, (c) 300^{o}C, and (d) 400^{o}C.

Figure 7.7 shows a higher resolution AFM scan of the annealed samples with a total scan size of 1µm X 1µm. Over this region the surface roughness shows a similar trend to the large area scans in which unannealed film shows reduced surface roughness in comparison to ITO. The unannealed sample has an RMS roughness of 0.5nm with a peak to peak roughness of 7.7nm. With annealing at 200^{o}C and 300^{o}C the RMS roughness of the Molybdenum Oxide increases to 0.7nm and 0.9nm, and the peak to peak roughness increases to 7.8nm and 8.6nm. For both films these low roughness

values indicate that the likelihood of shorts occurring through the organic layer remains small. At 400°C both the RMS and peak to peak show a large increase to 2.5nm and 33.1nm upon crystallization. The changes in peak to peak roughness seen upon crystallization on the small scale indicate that shorts are likely to occur often due to the high rate of variation in the height of the surface.

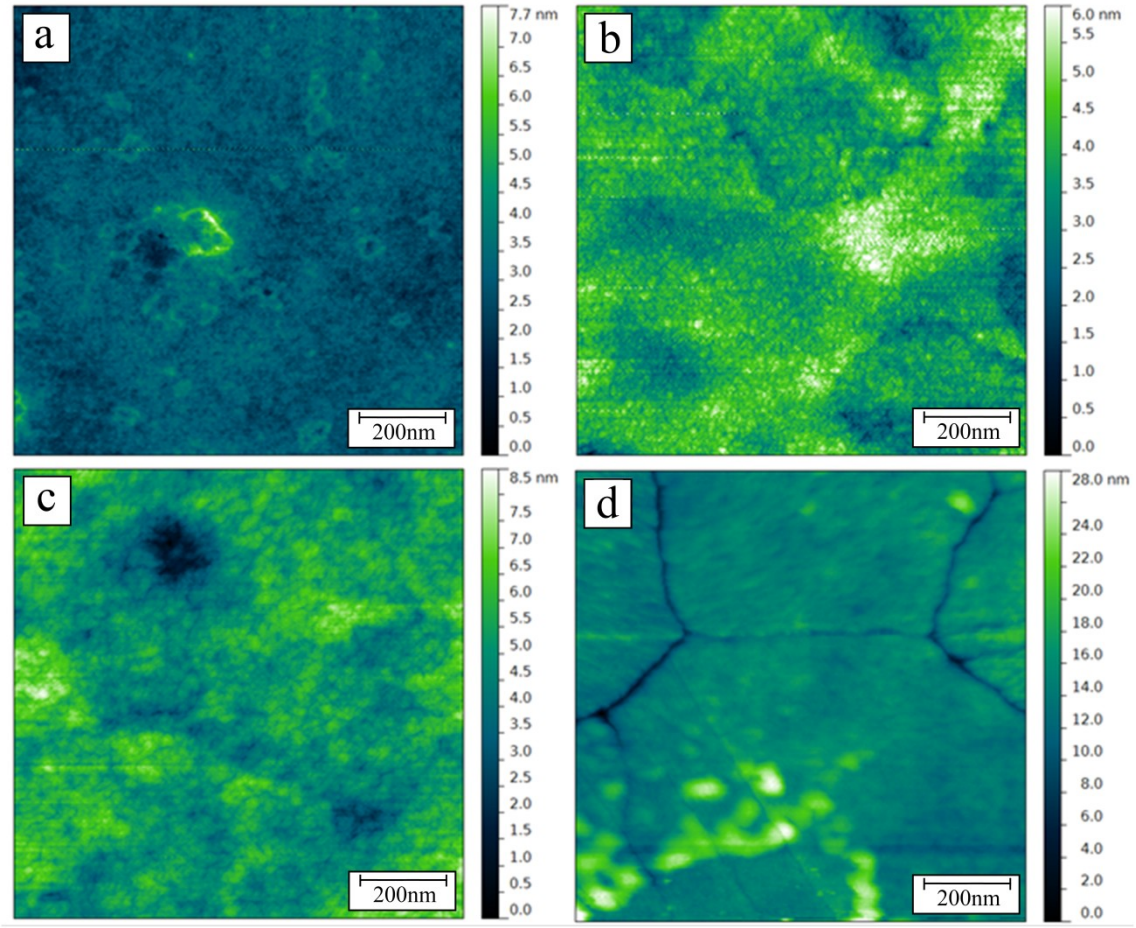

Figure 7.7 1μm x 1μm AFM scans of the deposited Ammonium Molybdate Tetrahydrate for (a) no annealing, (b) 200°C, (c) 300°C, and (d) 400°C.

Figure 7.8 shows spectroscopic ellipsometry results in which the thickness of the deposited ammonium molybdate tetrahydrate film varies as the substrate is annealed up to a temperature of 300^{o}C. The substrates are then left to cool as the samples are measured in order to see how the subsequent cooling affects the films thickness. The initial thickness of the deposited layer is 13.2nm, upon annealing a sharp decline in the thickness occurs between 75^{o}C and 200^{o}C with a temporary reduction in the rate observed between 100^{o}C and 150^{o}C. The solution that the Molybdenum Oxide is cast from contains a blend of two solvents, water and acetonitrile; these two solvents have boiling points of 100^{o}C and 82^{o}C.[2] It is expected that these two solvents should evaporate from the film at different rates depending on the temperature that the substrate is annealed at. The initial drop in thickness (as a function of temperature) can be attributed mainly to the evaporation of acetonitrile from the film, while drops at higher temperatures should be a combination of evaporation of both trapped solvents. Thermal expansion of the film will act to counter the reduction in the thickness and is the reason behind the drop in the rate of thickness reduction observed between 100^{o}C and 150^{o}C. At higher temperatures reductions in the thickness is still observed, earlier work on ammonium molybdate tetrahydrate showed that thermal annealing causes decomposition of the precursor material to Molybdenum (VI) Oxide through a multistage process.[7] This decomposition begins at temperatures as low as 100°C, **Equation 7.1** shows the chemical reaction involved in the thermal decomposition of ammonium molybdate tetrahydrate. This decomposition is what leads to the reduction in film thickness at higher temperatures this is due to a combination of removal of residual NH_4 as observed in XPS, reduction in the molybdate cluster size and densification of the deposited film.

$$\frac{1}{7}(NH_4)_6.Mo_7O_{24}.4H_2O \xrightarrow{100°C\text{-}140°C} \frac{1}{5}(NH_4)_4Mo_5O_{17} + \frac{24}{35}H_2O + \frac{2}{35}NH_3$$ **Equation 7.1**a

$$\frac{1}{5}(NH_4)_6.Mo_7O_{24}.4H_2O \xrightarrow{175°C\text{-}235°C} \frac{1}{4}(NH_4)_4Mo_5O_{17} + \frac{3}{20}H_2O + \frac{3}{10}NH_3$$ **Equation 7.1**b

$$\frac{1}{4}(NH_4)_6.Mo_7O_{24}.4H_2O \xrightarrow{275°C\text{-}298°C} \frac{1}{14}(NH_4)_4Mo_5O_{17} + \frac{5}{28}H_2O + \frac{5}{14}NH_3$$ **Equation 7.1**c

$$\frac{1}{14}(NH_4)_6.Mo_7O_{24}.4H_2O \xrightarrow{320°C\text{-}340°C} \frac{1}{22}(NH_4)_4Mo_5O_{17} + \frac{2}{77}H_2O + \frac{4}{77}NH_3$$ **Equation 7.1**d

$$\frac{1}{22}(NH_4)_6.Mo_7O_{24}.4H_2O \xrightarrow{\geq 340°C} MoO_3 + \frac{1}{22}H_2O + \frac{1}{11}NH_3$$ **Equation 7.1**e

Once cooling of the film begins the thickness shows a gradual decrease due to the reduced thermal expansion, once at room temperature the final film thickness is 7.7nm. Over the heating and cooling cycle the film shows a 42% reduction in total thickness, the trapped solvent within spray coated Molybdenum Oxide films therefore contribute a significant amount to the overall thickness.

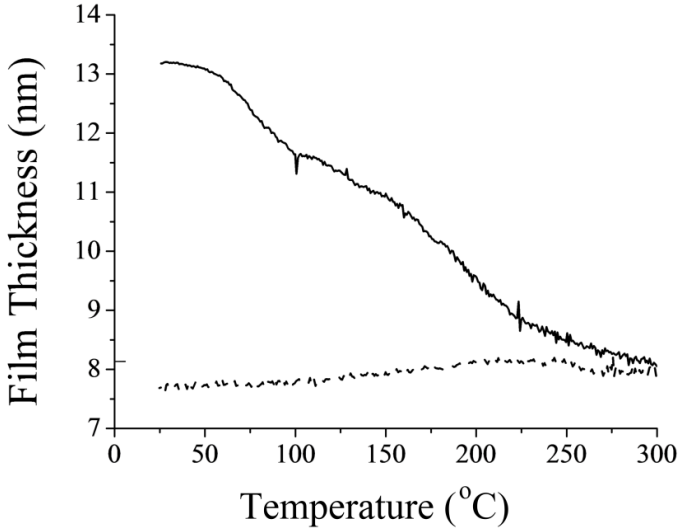

Figure 7.8 The thickness of deposited Molybdenum Oxide as it is heated to 300°C (−) and left to cool to room temperature (···)

7.3 Comparison of PCDTBT OPV Devices

Devices were fabricated with a PCDTBT:$PC_{70}BM$ (Poly[N-9'-heptadecanyl-2,7-carbazole-alt-5,5-(4',7'-di-2-thienyl-2',1',3'-benzothiadiazole)]: 6,6]-Phenyl-C71-butyric acid methyl ester) active layer that had been spray coated on top of vacuum evaporated and sputtered control devices, and solution processed molybdenum oxide. The solution processed molybdenum oxide was annealed at several temperatures between 200°C and 400°C for 1 minute; in addition samples of solution processed molybdenum oxide were left unnanealed as a comparison. The thickness of the vacuum deposited layers was 10nm at a pressure below 10^{-6}mbar with the sputter deposited film being deposited at 20% oxygen partial pressure with a chamber pressure of $1.6x10^{-2}$mbar and a flow rate of 9 SCCM. Solution processed Molybdenum Oxide was spray coated onto clean ITO substrates kept at 60°C in air with a pass height and speed of 50mm and 60mm.s^{-1}.

Ammonium Molybdate Tetrahydrate ($(NH_4)_6^+.Mo_7O_{24}^{6-}.4H_2O$) was dissolved in a 2:3 de-ionized water: acetonitrile blended solution at a concentration of 6mg.ml^{-1}. PCDTBT:$PC_{70}BM$ was dissolved in chlorobenzene at a ratio of 1:4 with an overall concentration of 4mg.ml^{-1}. The organic active layer was sprayed onto substrates held at 40^{o}C with a pass height and speed of 35mm and 80mm.s^{-1}, for more information on spray coating technique please see **Chapter 3.6**. **Figure 7.9** shows the variations in device performance parameters for the different deposition conditions of molybdenum oxide. In addition **Table. 7.2** shows the average values for devices fabricated under different processing conditions. It can be seen that for vacuum evaporated and sputter deposited devices the performance is the same within experimental error for the Fill Factor (FF), Short Circuit Current (J_{sc}), Power Conversion Efficiency (PCE) and Open circuit Voltage (V_{oc}). However in comparison to the spray coated Molybdenum Oxide device the performance is significantly lower. The reason for this was due to poor wetting of the organic layer for devices fabricated using vacuum deposited Molybdenum Oxide; this led to a thinner organic layer than was expected causing a reduction in both the J_{sc} and FF from what could be achieved with these devices.

Solution processed Molybdenum Oxide shows a large variation as a function of annealing temperature, for unnanealed films and films annealed at 200^{o}C the performance is at a minimum with the PCE and J_{sc} being effectively zero. UPS data shows that the work function of the deposited Molybdenum Oxide layer does not change with annealing temperature and is equal to that of vacuum deposited Molybdenum Oxide. This means that contact resistances at the interface between the anode and the hole transporting PCDTBT should not vary as a function of temperature. If this is the case then the Molybdenum Oxide layer itself is the only variable and for

low annealing temperatures is acting as a highly resistive layer that effectively blocks the transport of charge. The only observed difference between these films and those annealed at higher temperatures is the thickness of the deposited Molybdenum Oxide layer. Due to the large film swelling that occurs from trapped solvents one possible reason for the observed device characteristics could be that the solvents act to separate molybdate (Mo_7O_{24}) clusters. As charge carrier conduction through the film occurs because of electron transport through the Mo4d orbital localised on the molybdenum atom separation of the clusters would lead to an increased distance between the charge transport sites.

Upon annealing between 250^{o}C and 350^{o}C the performance of devices show an increase that is driven by both the change in J_{sc} and FF. As mentioned previously the UPS data show that over this annealing range the device show no variation in the electronic properties, and the work function of these layers remains fixed. AFM data shows a gradual increase in the roughness of the film when thermally annealed however this change is very small and would not account for such large variations that are seen in the device data. The only evidence for any significant change within the Molybdenum Oxide layer is from ellipsometry showing that the thickness has a large dependence upon trapped solvent. Increases in device performance are therefore attributed to this reduction in the thickness leading to a denser film. This has also been shown in previous work that films deposited from ammonium molybdate tetrahydrate have a strong dependence upon the thickness of the layer.[1] Devices fabricated using Molybdenum Oxide annealed at 400^{o}C show a drop in all the metrics that are used to gauge device performance. AFM data obtained show that at this temperature crystallization occurs and the surface of the film increase in roughness, this increase will

lead to shorts through the organic layer. Shorts through the device cause reductions in V_{oc} due to charge recombination and the J_{sc} is reduced because of alternative paths for current to flow a reduction in both these values leads to a reduction in FF.

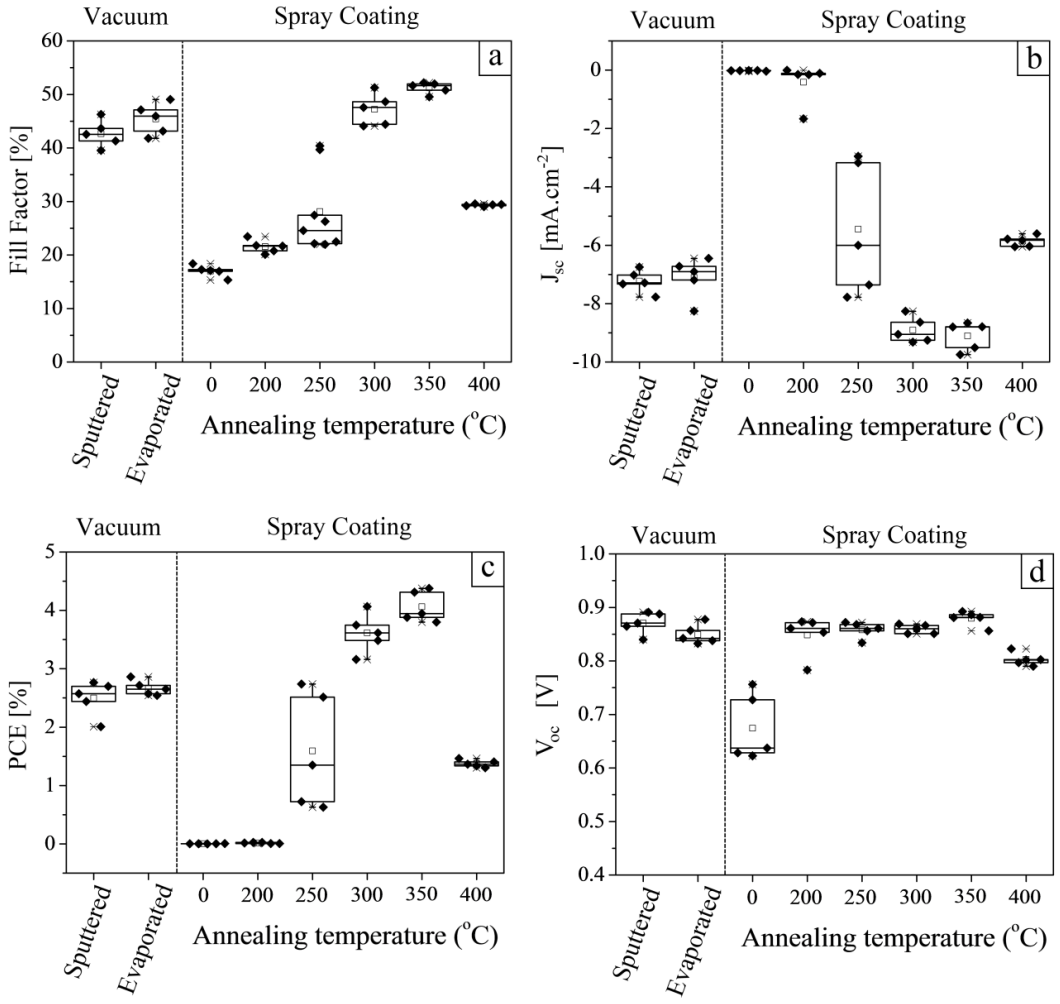

Figure 7.9 Comparison of performance parameters for devices with molybdenum oxide hole extraction layers deposited via vacuum deposition techniques and spray coating followed by subsequent annealing. Where the performance parameters are (a) Fill Factor, (b) Short Circuit Current, (c) Power Conversion Efficiency, and (d) Open Circuit Voltage.

	FF (%)	V_{oc} (V)	PCE (%)	J_{sc} (mA.cm^{-2})
Sputtered	42.5	0.87	2.49	-7.32
Evaporated	45.9	0.84	2.66	-6.90
Unannealed	17.0	0.67	0.01	-0.01
200^{o}C Anneal	21.8	0.85	0.01	-0.17
250^{o}C Anneal	28.0	0.86	1.59	-5.45
300^{o}C Anneal	47.5	0.86	3.62	-8.92
350^{o}C Anneal	51.6	0.88	4.07	-9.12
400^{o}C Anneal	29.2	0.80	1.37	-5.86

Table 7.2 Shows the average values for the Fill Factor, Open Circuit Voltage, Power Conversion Efficiency and Short Circuit Current for OPV device fabricated with different molybdenum oxide hole extracting layers.

7.4 Improvements in Device Performance

The work performed in previous experiments showed that annealing did not cause significant changes in either the chemical state or electronic structure as observed by photoelectron spectroscopy. In addition high temperature annealing exceeding 350^{o}C led to the crystallization of the deposited layer putting an upper limit on the annealing temperature. Annealing below this temperature led to slight roughening of the surface and was not the cause of the large variations in the performance of devices. Spectroscopic ellipsometry revealed that the main reason behind the changes in device performance was the reduction in thickness of the Molybdenum Oxide layer via the driving out of trapped solvent. In order to achieve a low temperature solution

processable Molybdenum Oxide film via a scalable process such as spray coating greater control of the thickness of the deposited layer is needed. In spray coating the thickness can be controlled by variations in the amount of solution dispensed onto the surface, this can be altered by changing the nozzle height or the pass speed this method allows for fine tuning of the thickness. A large reduction in film thickness can only be achieved by variations in the initial concentration of the dispensed solution. In order to deposit Molybdenum Oxide films via spray coating that require no annealing the concentration of the dispensed solution was reduced to $1mg.ml^{-1}$, $0.5mg.ml^{-1}$ and $0.25mg.ml^{-1}$.

Figure 7.10 shows the average device results for films sprayed at the three different concentrations; in addition films have been annealed at $150^{o}C$, $250^{o}C$ and $350^{o}C$ to see if further annealing leads to increase in the performance. The average values obtained are also shown in **Table 7.2**. It can be seen for the highest concentration solution ($1mg.ml^{-1}$) that working devices can be obtained for unannealed films, upon annealing of these higher concentration films a gradual increase in the performance is seen. The increase in performance, as seen in previous work, is due to the improved FF and J_{sc} this indicates that for the higher concentration films that there is still trapped casting solvent. For films deposited from $0.5mg.ml^{-1}$ solution the unannealed films show performance almost identical to that of films cast from higher concentration solutions and annealed at $350^{o}C$. This confirms that reduction in film thickness is the driving force behind the improvements seen within devices where the molybdenum oxide layer had been annealed. Reducing the thickness of deposited films either by further solution concentration reduction to $0.25mg.ml^{-1}$ or by thermal annealing does not lead to major changes within efficiency. The only exception to this is for films

deposited from 0.5mg.ml^{-1} solution and annealed at 350^{o}C, an average efficiency of 4.6% is observed with this being 0.4% higher than the average for any other device. Looking at the individual values for the FF, V_{oc} and J_{sc} it can be seen that none of them show any major improvement over values obtained under different deposition conditions. The high PCE observed for films deposited from 0.5mg.ml^{-1} solution and annealed at 350^{o}C are due to statistical variations from a low sample size rather than any improvements brought about by changes in the processing conditions.

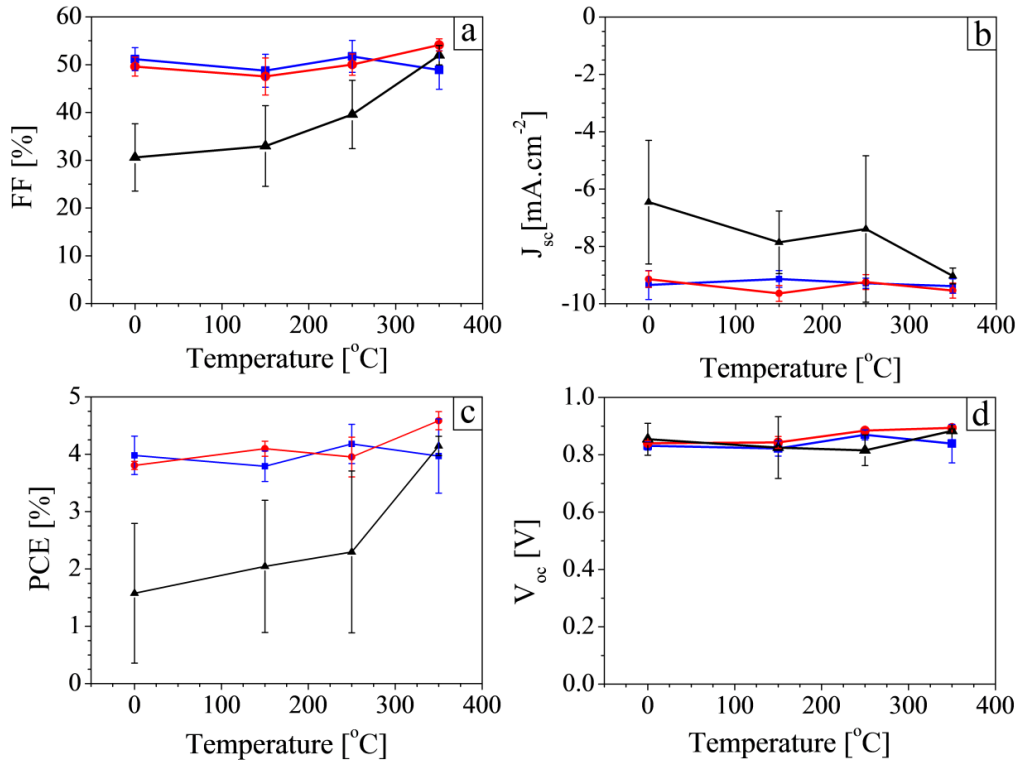

Figure 7.10 Comparison of performance for films deposited from solutions with 1mg.ml^{-1} (▲), 0.5mg.ml^{-1} (●), and 0.25mg.ml^{-1} (■). Where the performance parameters are (a) Fill Factor, (b) Short Circuit Current, (c) Power Conversion Efficiency, and (d) Open Circuit Voltage.

	Concentration	0°C	150 °C	250 °C	350 °C
FF [%]	1mg.ml^{-1}	31	33	40	52
	0.5mg.ml^{-1}	50	48	50	54
	0.25mg.ml^{-1}	51	49	52	49
J_{sc} [mA.cm^{-2}]	1mg.ml^{-1}	-6.5	-7.9	-7.4	-9
	0.5mg.ml^{-1}	-9.1	-9.6	-9.2	-9.5
	0.25mg.ml^{-1}	-9.3	-9.1	-9.3	-9.4
PCE [%]	1mg.ml^{-1}	1.6	2	2.3	4.1
	0.5mg.ml^{-1}	3.8	4.1	4	4.6
	0.25mg.ml^{-1}	4	3.8	4.2	4
V_{oc} [V]	1mg.ml^{-1}	0.85	0.83	0.82	0.88
	0.5mg.ml^{-1}	0.84	0.84	0.88	0.89
	0.25mg.ml^{-1}	0.83	0.82	0.87	0.84

Table 7.2 Average results for OPV devices fabricated with solution processed molybdenum oxide spray coated from different.

7.5 Conclusion

Using ultrasonic spray-coating it is possible to sequentially deposit molybdenum oxide from a solution for use in organic photovoltaic device. Results show that the thermal annealing of the Molybdenum Oxide film causes increases in all device parameters with a peak PCE of 4.1% occurring at an annealing temperature of 350°C. This increase in device performance is attributed to the reduction in thickness of the Molybdenum Oxide

layer due to the driving out of trapped solvent within the deposited layer and subsequent structural rearrangement. XPS and UPS reveal that no significant change in the chemical composition or the electronic structure of the Molybdenum Oxide film occurs and that the only change observed is a small increase in reduced Mo^{5+} states and the loss of NH_4^+ from the layer. Annealing beyond a critical temperature induced crystallization of the deposited Molybdenum Oxide layer leading to a reduction in the PCE of the device to 1.4%. This performance reduction is due to shorts within the device induced by the high surface roughness of the anode material leading to a reduction in the V_{oc}, FF and J_{sc}. In order to obtain maximum device performance the deposited molybdenum oxide must be below a specific thickness. Further device data in which the concentration of the deposited Molybdenum Oxide solution was varied show that is possible to deposit a film thin enough via spray coating to obtain high device performance without annealing. For unannealed devices the highest power conversion efficiency obtained was 4.3% for a $0.25mg.ml^{-1}$ solution. The highest PCE for any cell was 4.8% for devices deposited from $0.5mg.ml^{-1}$ solution followed by thermal annealing at 350^oC. This indicates that with further optimization of the initial solution it should be possible to deposit spray coated Molybdenum Oxide films that require no annealing that have performances greater than spin coated PEDOT:PSS. In addition characterisation of how the lifetime of solution processed devices compare to those fabricated using vacuum deposited molybdenum oxide is needed. Along with characterisation of the lifetime of solution processed molybdenum oxide for different annealing conditions to see if the levels of trapped solvents affect the stability of devices.

7.6 References

[1] V. Shrotriya, G. Li, Y. Yao, C. W. Chu & Y. Yang. Transition Metal Oxides as the Buffer Layer for Polymer Photovoltaic Cells. *Applied Physics Letters*. **88** (2006) 073508

[2] J. Meyer, S. Hamwi, M. Kroger, W. Kowalsky, T. Riedl & A. Kahn. Transition Metal Oxides for Organic Electronics: Energetics, Device Physics and Applications. *Advanced Materials*. **24** (2012) 5408-5427

[3] S. Murase & Y. Yang. Solution Processed MoO_3 Interfacial Layer for Organic Photovoltaics Prepared by a Facile Synthesis Method. *Advanced Materials*. **24** (2012) 2459-2462

[4] D. R. Lide. *Handbook of Chemistry and Physics*. 79th edition. Boca Raton: CRC Press; 1998

[5] M. C. Gwinner, R. D. Pietro, Y. Vaynzof, K. J. Greenberg, P. K. Ho, R. H. Friend & H. Sirringhaus. Doping of Organic Semiconductors Using Molybdenum Trioxide: a Quantitative Time-Dependent Electrical and Spectroscopic Study. *Advanced Functional Materials*. **21** (2011) 1432-1441

[6] H. Hoppe & N. S. Sariciftei. Organic Solar Cells: An Overview. *Journal of Materials Research*. **24** (2004) 1924-1945

Chapter 8

The Effect on Devices of Reduced States in sputtered MoO_x Films

8.1 Introduction

Deposition of metal oxides by various different means can often lead to variations in the oxidation state of the deposited material. A prime example of this is with vacuum evaporation; this deposition technique relies on heating a small amount of material at just below or beyond its melting point and allowing material to undergo evaporation or sublimation from the surface. However these materials can undergo decomposition in which the oxidation state reduces due to leeching of oxygen from the surface to the surrounding environment.[1,2] Due to the high temperatures needed to evaporate metal oxides it is often the case that reduced oxidation states are observed in deposited films, it is also possible that high temperature heat treatment of solution processed films could lead to these reduced states. In the following chapter work has been undertaken in order to observe if reduced states of Molybdenum Oxide can affect device performance in organic photovoltaics. Characterisation of the reactive sputtering process is done looking at the presence of different oxidation states and the average overall oxidation

state. The effect these reduced states have on the performance of organic photovoltaic devices are studied by looking at a combination of the energy level structure of deposited films, the average oxidation states of deposited films, and the presence of specific oxidation states through x-ray photoelectron spectroscopy and ultraviolet photoelectron spectroscopy, and comparing that to solar cell device results obtained.

8.2 Deposition Characterisation

Initial characterisation of the sputter deposition of Molybdenum Oxide was done by studying the changes in the DC bias of the deposition target. As mentioned previously in **Chapter 3.8** oxidation of the surface layers of the sputter target lead to the formation of insulating layers at the targets surface, these insulating layer lead to changes in the applied bias of the deposition system in order to maintain a fixed power coupled into the plasma. This process can be done to test the points in which changes in the oxidation state of the target occur and at what point target poisoning occurs. Deposition from the Molybdenum target was started at 0% oxygen partial pressure and the Bias was allowed to settle for 30seconds before increasing the partial pressure of oxygen. **Figure 8.1** shows the bias response for the increase in oxygen partial pressure, the solid line with squares shows the bias for increasing partial pressure and the dotted line with circles shows it for decreasing partial pressure. The initial drop in applied bias is due to an increase in the overall system pressure, this overall increase leads to more molecules present within the chamber increasing the probability of collisions. With a higher probability of collisions occurring the amount of charge carriers within the plasma increase this leads to a reduction in the applied voltage needed to maintain the plasma at

a fixed power. Further increases in the partial pressure lead to a gradual increase in the bias this is due to oxidation of the surface of the target. The rate of removal of this oxide layer will likely be higher than the oxidation rate of the target as the increase in bias is only small over this time scale. This gradual increase in bias occurs until around 15%, when the partial pressure is further increased the applied voltage sees a increase of 0.5V per percent increase to 1.5V per percent increase as a function of the increase in oxygen partial pressure. This indicates that a switch from oxidation of the surface layer of the target to oxidation of deeper layers is occurring leading to an increase in the resistance of the target. At 30% the rate of increase in the bias reaches a maximum of 2.8V per percent increase indicating that oxidation of the targets surface is complete. Increases in the applied bias after 30% oxygen partial pressure are due to the diffusion of oxygen into the target leading to a further increase in resistance. Upon reducing the oxygen partial pressure it can be seen that a hysteresis effect occurs in the applied bias, this hysteresis is due to poisoning of the target in which the oxidation of the target has reached a sufficient depth into the surface that it takes a prolonged amount of sputtering time to remove this oxide layer. From **Figure 8.1** it is possible to estimate that oxidation of the surface occurs from 5% oxygen partial pressure onwards, this oxidation is not fully complete until some point between 15% oxygen partial pressure and 20% oxygen partial pressure. Beyond this oxygen within the chamber directly oxidizes molybdenum just below the surface layer until 30% when a maximum is reached and diffusion is the main process by which further oxidation of the target occurs. This is the point at which the target can be said to be poisoned and a minimum deposition rate will be obtained for the sample.

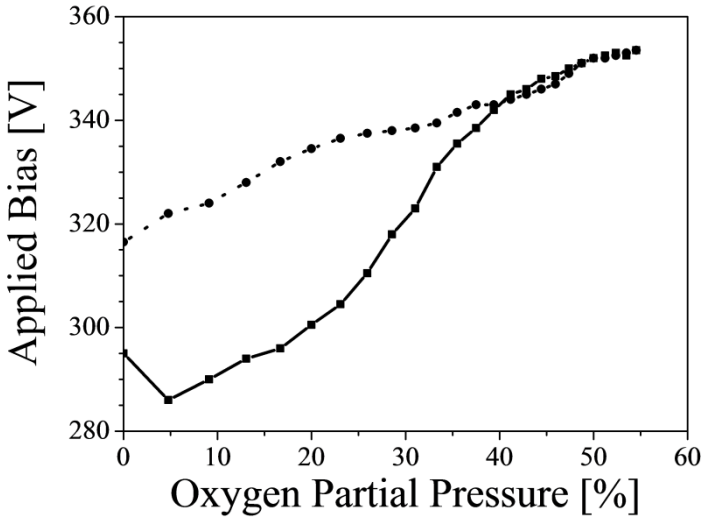

Figure 8.1 Shows how the variations in the partial pressure of oxygen can cause changes to the applied bias to the target and how the reverse bias characteristics (Dotted line and circles) vary for high oxygen content.

Figure 8.2 shows how the three main deposition parameters cause variations in the deposition rates of the molybdenum/molybdenum oxide layer. The films deposited for varying pressure and power were done using Argon as the sputtering gas. **Figure 8.2**a shows the variation in deposition rate as a function of the overall pressure, the power was maintained at 200W, it can be seen that an increase in deposition rate is observed until approximately $1.3x10^{-2}$mbar. This increase in deposition rate is due to the increased presence of Argon able to be used in sputtering material from the surface, as mentioned previously in **Chapter 3.8** the pressure dependence on sputtering rate is a trade off between an increased number of ions available for sputtering and an increased amount of atoms and molecules for scattering. As the scattering begins to dominate this trade off the deposition rate drops, this scattering is also important for reducing the amount of high energy atoms are sputtered from the surface. By sputtering at higher

pressures the damage to the substrate from high energy sputtered atoms can be reduced. **Figure 8.2**b shows the deposition rates dependence upon the power, it can be seen that it can be estimated as a linear dependence, higher powers lead to higher energy sputtered atom. The power has a limit to the value it can be reduced to as the ability to strike a plasma is reduced as the applied bias is directly related to the power used. From these experiments the lowest power that could reliably result in a plasma being struck was around 180W. **Figure 8.2**c shows the deposition rates dependence on the oxygen partial pressure, in this experiment the overall pressure was fixed at $1.5x10^{-2}$mbar and the power fixed at 200W. It is possible to relate regions within the graph to the bias dependence upon oxygen partial pressure shown in **Figure 8.1**, for low oxygen partial pressures the deposition rate drops at a slow rate similar to the slow increase in the bias observed. This slow drop in deposition rate is due to the increased surface coverage of the oxide layer, a large drop is not observed yet as the surface is likely not fully oxidized. Between 10% and 20% a drop in the deposition rate of approximately $1Å.s^{-1}$ is seen, this is due to the complete surface coverage of Molybdenum Oxide and the oxidation of the target just beneath the surface layer. Such a drastic change is observed due to the sputtering yield of Molybdenum Oxide being lower than that of pure molybdenum. The deposition rate shows a gradual decline after this surface oxidation as the oxide layer on the surface penetrates deeper into the target.

From these graphs the ideal sputtering conditions to use in devices would be the lowest possible power that a plasma can be reliably struck and as higher pressure as possible. However in reality with reactive sputtering this is not viable due to the extremely low deposition rates that occur at higher oxygen concentration, for

subsequent depositions of molybdenum oxide via sputtering the power was maintained at 200W and the overall pressure was kept at $1.5x10^{-2}$mbar.

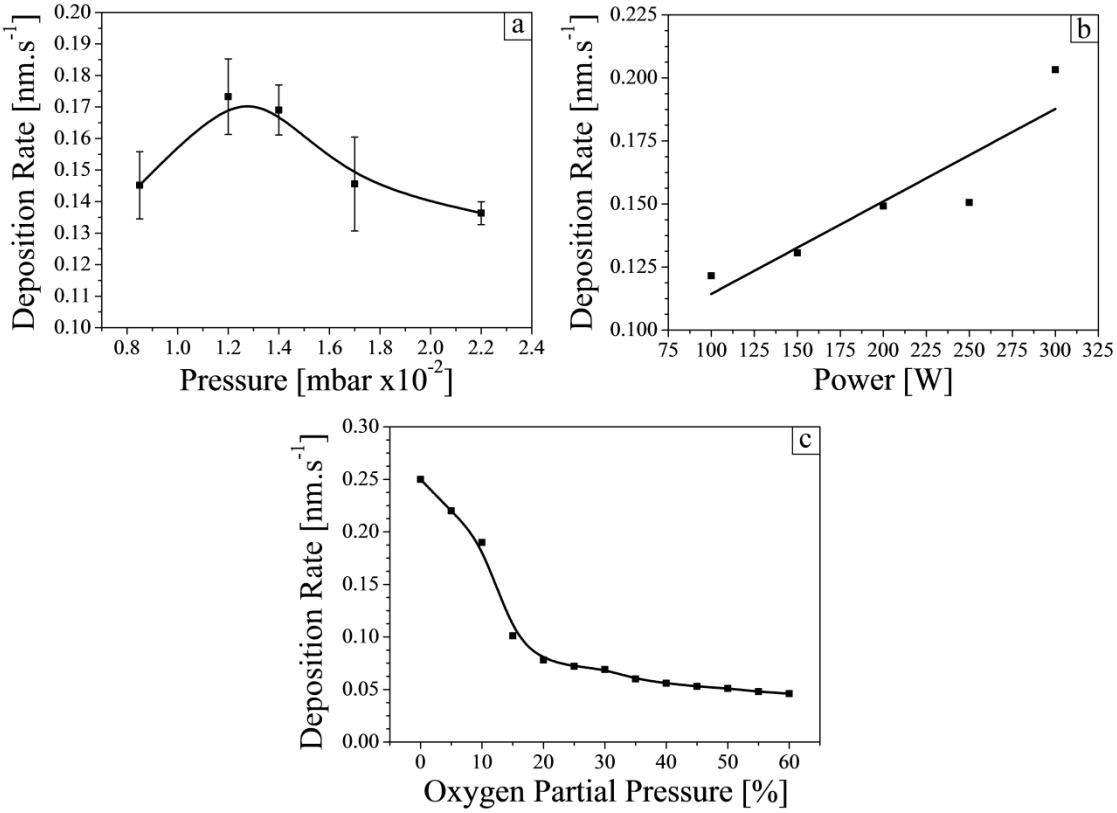

Figure 8.2 Sputtering conditions have varying effects on the deposition rate; (a) the pressure, (b) the power, and (c) the oxygen partial pressure are shown.

8.3 Optical Properties of Films

Spectroscopic ellipsometry of the deposited films was performed between 350nm and 700nm for samples sputtered between 0% oxygen partial pressure and 45% oxygen partial pressure. **Figure 8.3** shows the real and the imaginary part (the extinction coefficient) of the refractive index, along with the comparison of measure and fitted values for delta and psi for samples sputtered at 0%, 10% and 15% oxygen partial pressure. The Molybdenum Oxide layer was modelled using a combination of a Drude oscillator to model the absorption due to electrons within the conduction band and Lorentzian oscillators to model band to band absorption of light. Results show that for films sputtered at 0% oxygen concentration that the extinction coefficient calculated is a high value ranging from 2 to 2.4 across the visible spectrum. This high absorption across much of the measured spectrum is due to the absorption from electrons within the conduction band as is indicative of metallic materials. Comparisons against the measured refractive index for purely metallic molybdenum by Palik reveal that similarities are observed in the spectra.[3] The observed refractive index as measured by Palik varies from around 3.2 at 300nm to 5 at 1200nm with a rapid increase in the refractive index between 300nm and 500nm. These values are close to those observed for Molybdenum Oxide films sputtered at 0% oxygen content however it should be noted that due to the presence of Molybdenum Oxide species even within films sputtered at 0% oxygen content the films are not pure Molybdenum like those measured by Palik.

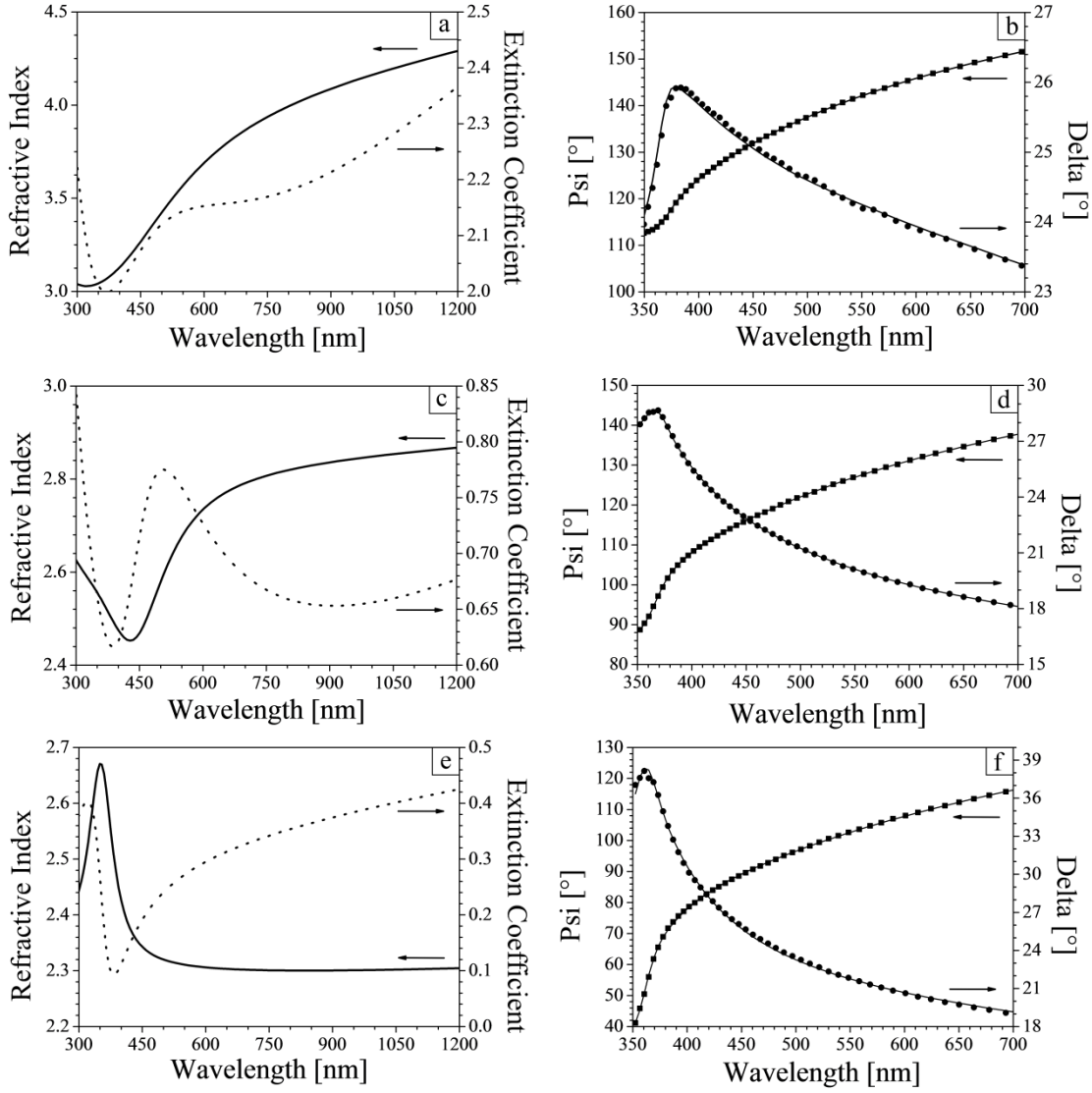

Figure 8.3 Films sputtered at 0% (a and b), 10% (c and d) and 15% (e and f) oxygen partial pressure showing (a, c and e) the real and imaginary parts of the refractive index, and (b, d and f) the comparison of measured values (■ and ●) against the fitted values (–) of Delta and Psi.

Figure 8.4 shows the real and the imaginary part (the extinction coefficient) of the refractive index, along with the comparison of measure and fitted values for delta and psi for samples sputtered at 20% and 25% oxygen partial pressure. Observations with the modelled spectra of molybdenum oxide sputtered at 15% that show that a single oscillator is observed at around 400nm, the energy of this peak is approximately 3.1eV and is associated with absorption from the O2p band to the $Mo4d_{3/2}$ band in highly oxidized molybdenum oxide. This peak indicates that the oxide material dominates the optical properties of the film and the modelling using the Cauchy dispersion model at higher oxygen concentrations will yield more accurate results due to the reduced fitting parameters. From films sputtered at both 20% and 25% oxygen partial pressure ellipsometric data shows that the absorption peak remains static. The dispersion of light at longer wavelength shows an increase in intensity however the dispersion at shorter wavelengths close to the absorption band edge is reduced.

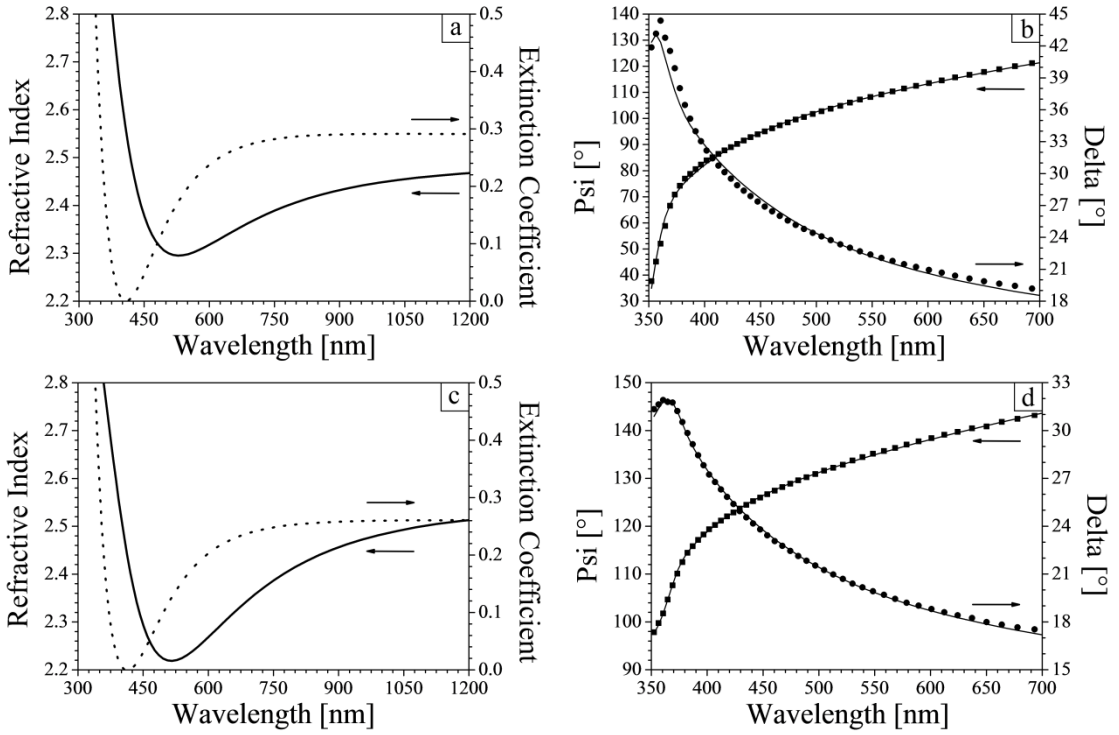

Figure 8.4 Films sputtered at (a and b) 20% and (c and d) 25% oxygen partial pressure showing (a and c) the real and imaginary parts of the refractive index, and (b and d) the comparison of measured values (■ and ●) against the fitted values (–) of Delta and Psi.

8.4 Oxidation of Sputtered Films

Films sputtered in tandem with substrates used for devices were measured via XPS in order to determine the overall oxidation state of the film, the presence of individual oxidation states, and possible contaminants within the film. **Figure 8.5** and **Figure 8.6** shows scans of the wide spectra, O1s spectra and Mo3d spectra for films sputtered between 0% oxygen partial pressure and 25% oxygen partial pressure. In addition XPS scans were taken for samples up to 70% oxygen partial pressure, the scans for these are not shown however results obtained from the Mo3d peaks are shown in **Figure 8.3**.

Wide scans from all samples indicate that only Carbon, Nitrogen, Oxygen and Molybdenum were found. A small trace of Silicon (less than 0.5%) was also found in samples sputtered at 5%, 10% and 15% the presence of this silicon is attributed to the underlying silicon substrates used for XPS analysis and should not be present within the devices. O1s spectra for all samples reveal the presence of three different species within the films; these are water (H_2O), metal hydroxides (OH^-) and molybdenum oxide (MoO). The O1s peak backgrounds were fitted using a Shirley background substitution and the chemical states were fitted using several Gaussian peaks. The peaks of these chemical states are situated on average at 531.9eV, 530.9eV and 530.2eV.[4,5] **Table 8.1** shows the variation in the abundance and position of these different species for films sputtered between 0% oxygen partial pressure and 30%.

The backgrounds of the Mo3d spectra were subtracted using a Shirley background substitution until 25% oxygen partial pressure; at higher oxygen partial pressure a linear background subtraction was used. Individual oxidation states were fitted using a doublet pair that was separated by 3.15eV where the full width half maximum (FWHM) were made equal and the intensity of the higher binding energy peak was two thirds that of the lower binding energy peak.[4,6,7] In the samples sputtered with low oxygen concentration multiple doublet peaks are observed corresponding to different oxidation states ranging from Mo^{1+} to Mo^{6+} with increased oxygen during sputtering the intensity of the lower binding energy peaks decreases and the intensity of the higher binding energy peaks increase. **Table 8.2** shows the abundances of the different doublet peaks and their position for samples sputtered between 0% oxygen partial pressure and 30% oxygen partial pressure.

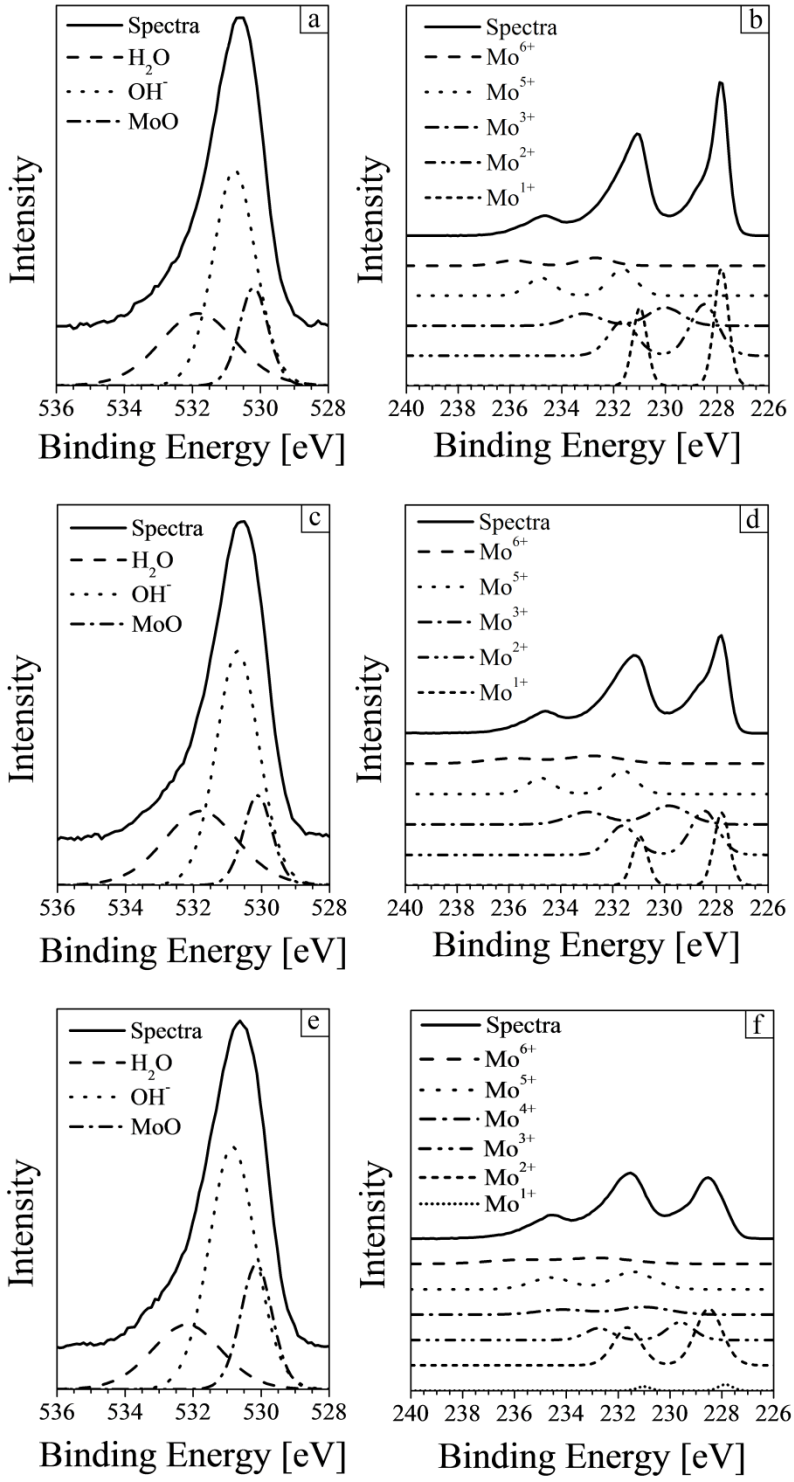

Figure 8.5 High resolution XPS scans of the O1s peak, and Mo3d peak for films sputtered at, (a,b) 0% oxygen partial pressure, (c,d) 5% oxygen partial pressure, and (e,f) 10% oxygen partial pressure.

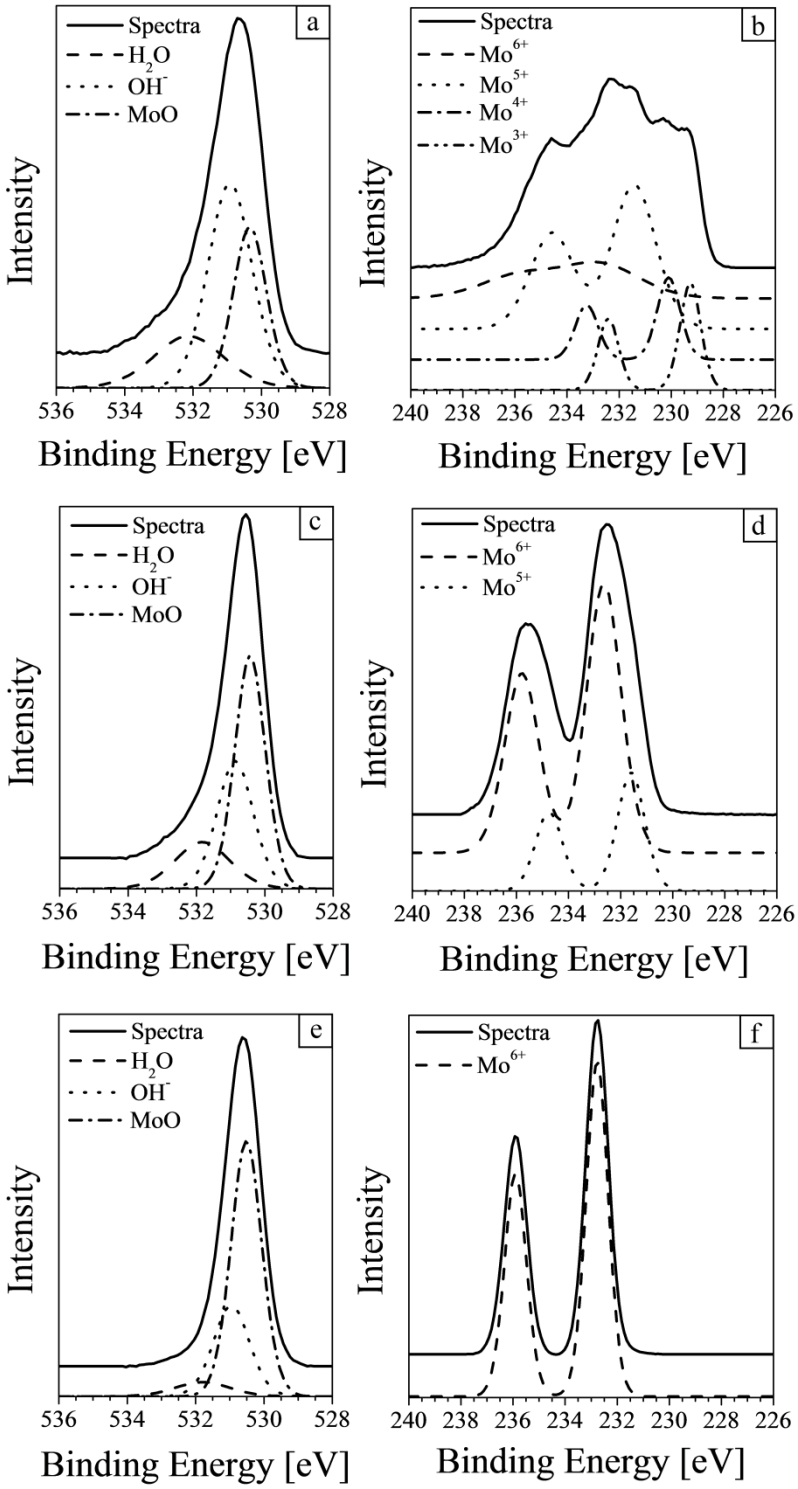

Figure 8.6 High resolution XPS scans of the O1s peak, and Mo3d peak for films sputtered at, (a,b) 15% oxygen partial pressure, (c,d) 20% oxygen partial pressure, and (e,f) 25% oxygen partial pressure.

	0%	5%	10%	15%	20%	25%	30%
H_2O	531.8eV	531.8eV	532.2eV	532.1eV	531.8eV	531.8eV	531.9eV
OH^-	530.8eV	530.7eV	530.9eV	530.9eV	530.9eV	531.0eV	531.1eV
MoO	530.2eV	530.1eV	530.1eV	530.3eV	530.4eV	530.5eV	530.6eV
H_2O	15.6%	14.7%	10.9%	10.3%	11.1%	4.3%	5.8%
OH^-	76.4%	78.4%	79.5%	74.6%	58.3%	43.1%	36.4%
MoO	8.1%	6.9%	9.6%	15.1%	30.5%	52.6%	57.8%

Table 8.1 Position and abundances of the difference chemical peaks in the high resolution O1s spectra.

Table 8.1 shows that as the oxygen content of the film are increased the relative abundance of the H_2O and OH^- species decrease both of these are related to penetration of water into the film. This reduction is likely due to the increased presence of the O-Mo-O bonds within the film because of the higher oxidation state of the Molybdenum Oxide film. **Table 8.2** shows an increase in the higher oxidation states and a decrease in the lower oxidation states as the oxygen content in the chamber increases. This correlates to the increased relative abundance of the O-Mo-O peak that is seen in the O1s spectra.

	0%	5%	10%	15%	20%	25%	30%
Mo^{1+}	230.9	230.9	231.0	-	-	-	-
Mo^{2+}	231.7	231.6	231.7	-	-	-	-
Mo^{3+}	-	232.9	232.8	232.4	-	-	-
Mo^{4+}	233.2	-	-	233.2	-	-	-
Mo^{5+}	234.8	234.8	234.8	234.6	234.7	234.2	234.3
Mo^{6+}	235.9	235.9	235.9	235.9	235.8	235.9	236
Mo^{1+}	35.71	26.88	2.33	-	-	-	-
Mo^{2+}	30.67	27.31	43.25	-	-	-	-
Mo^{3+}	-	20.7	14.09	17.31	-	-	-
Mo^{4+}	13.19	-	-	14.54	-	-	-
Mo^{5+}	14.94	15.47	28.65	48.33	25.9	0.13	0.53
Mo^{6+}	5.49	9.64	11.67	19.82	74.1	99.87	99.47
O:Mo	1.29	1.39	1.65	2.35	2.87	2.999	2.997

Table 8.2 Position and abundances of the difference chemical peaks in the high resolution Mo3d spectra. Values given are for the $3d^{3/2}$ emission peak, the abundances and FWHM are the same for the $3d^{5/2}$ peak and the binding energy is 3.15eV lower.

Figure 8.7 shows that the oxidation state of the film increases rapidly beyond 5% oxygen partial pressure, this correlates with the increase in bias observed at 5% total pressure as seen in **Figure 8.1**. Initial increases in the overall oxidation state is driven by the rise in the amount of the Mo^{5+} state, once the metallic Mo^{4+} state and below are no longer present the Mo^{6+} state begins to lead to the increase in overall oxidation state.

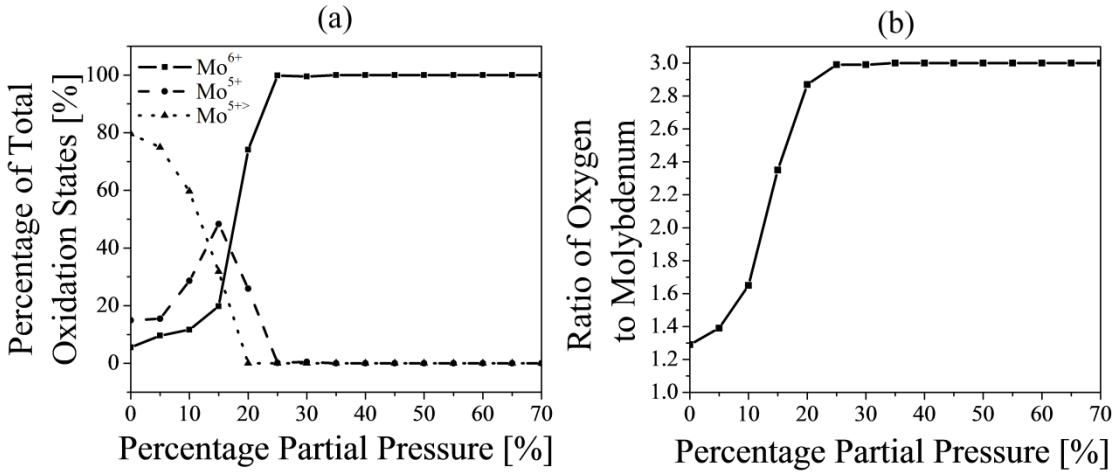

Figure 8.7 Results of the XPS scans of sputtered samples between 0% and 70% oxygen partial pressure showing (a) the percentage presence of Mo^{6+}, Mo^{5+} and metallic states below Mo^{5+}, and (b) the oxygen to molybdenum ratio.

8.5 Oxidation State and Electronic Structure

A second sputtering run was done for films reactively sputtered between 0% oxygen partial pressure and 25% oxygen partial pressure in order to determine how the energy level structure varied along with the stoichiometry. For each sample XPS spectra of the Mo3d, O1s and C1s peaks were taken along with a wide scan across the XPS emission spectra. In addition Ultraviolet Photoelectron Spectroscopy (UPS) scans from 0eV binding energy to 21.2eV were taken looking at the secondary electron cut-off and the valence band region. Wide scans were used to see if any contamination was present from other materials and C1s peaks were used to calibrate the position of the XPS peaks. **Figure 8.8** shows the spectra for films deposited with 0% oxygen partial pressure. Emission from the Mo3d peak is shown in **Figure 8.8**a, background subtraction was performed using a Shirley background correction. Doublet peaks were

fitted in which the ratio of the areas of the $3d^{3/2}$ and $3d^{5/2}$ peaks were 1:2, the FWHM of the doublet peaks were identical and the distance between the peaks was fixed at 3.15ev.[6,7] Information on the different chemical states of Molybdenum ranging from Molybdenum (VI) Oxide to Molybdenum (I) Oxide can be seen in **Table 8.4**. **Figure 8.8**b shows the O1s emission in higher detail, the background of the spectra has been corrected using the Shirley background correction. The spectra have been broken down into several individual Gaussian peaks corresponding to Oxygen within different states of chemical bonding. There are three different chemical states of oxygen measured and these have been attributed to $H\text{-}O^-$ (OH-), Mo-O-Mo (MoO), and H-O-H (H_2O) these peaks are located at roughly 530.2eV, 530.8eV and 531.7eV.[4,5] Positions of these peaks, abundance of each chemical state and the FWHM of the Oxygen peaks are shown in **Table. 8.5**.

Figure 8c shows the secondary electron cut-off and valence band region of the UPS spectra for the sputtered film. The work function is calculated from measuring the energy difference between the secondary electron cut-off and the Fermi level. The valence band position can be determined relative to Fermi level by looking at the drop off from the O2p peak that can be seen as the large increase in intensity at around 3eV. For metallic films the Valence band is not of importance due to the large amount of occupied states between the valence band and Fermi level. **Table 8.6** shows the different values measured and calculated from the UPS spectra for sputtered films. **Figure 8.10** to **Figure 8.13** show the different photoelectron spectroscopy scans for samples prepared at 5%, 10%, 15%, 20% and 25% oxygen respectively. Information about these spectra is given in **Table 8.3** to **Table 8.5** for comparison of different values as a function of sputtering conditions.

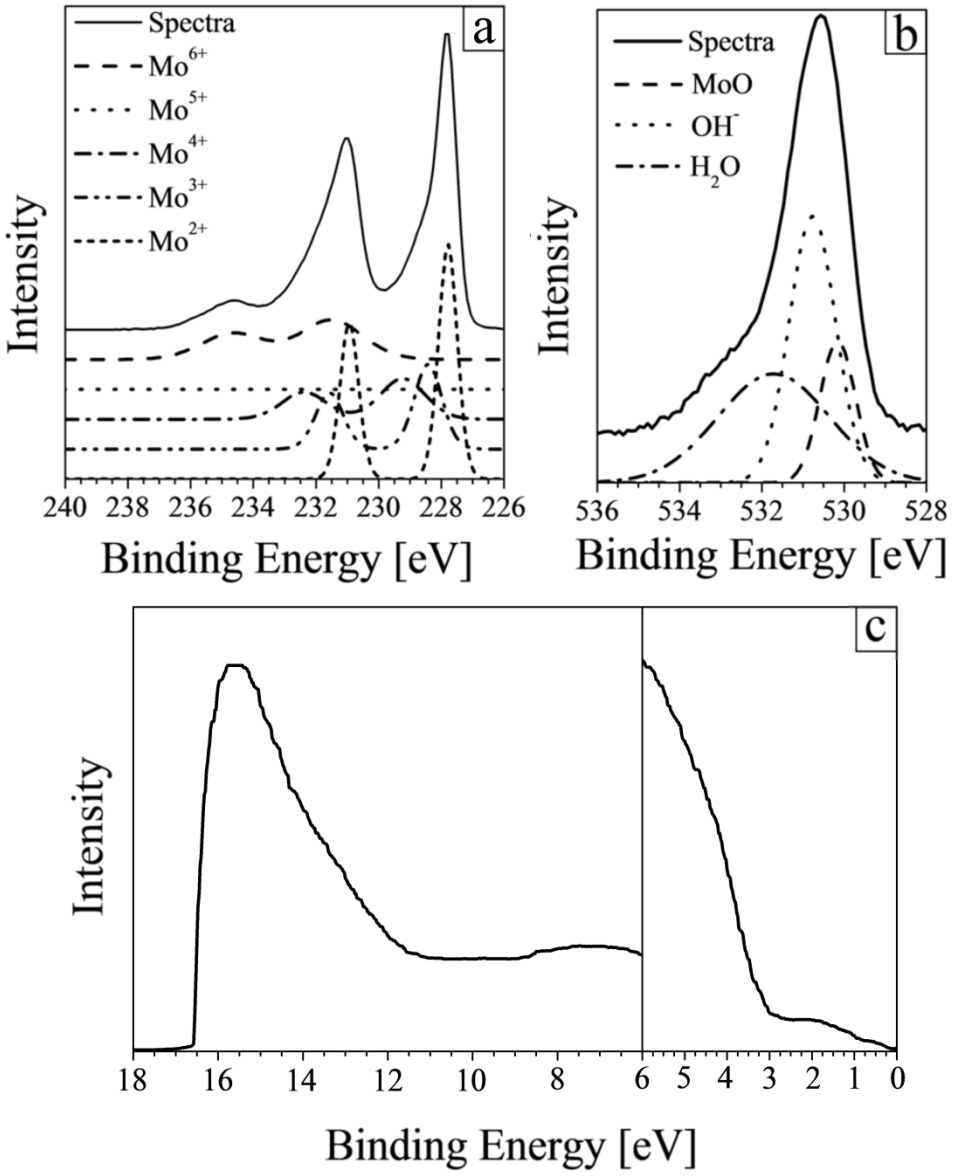

Figure 8.8 Photoelectron spectroscopy spectra for molybdenum oxide films sputtered at 0% oxygen partial pressure. X-ray photoelectron scans of the (a) Mo3d peak, (b) O1s peak, and (c) the full UPS spectra with an enhanced view of the valence band region.

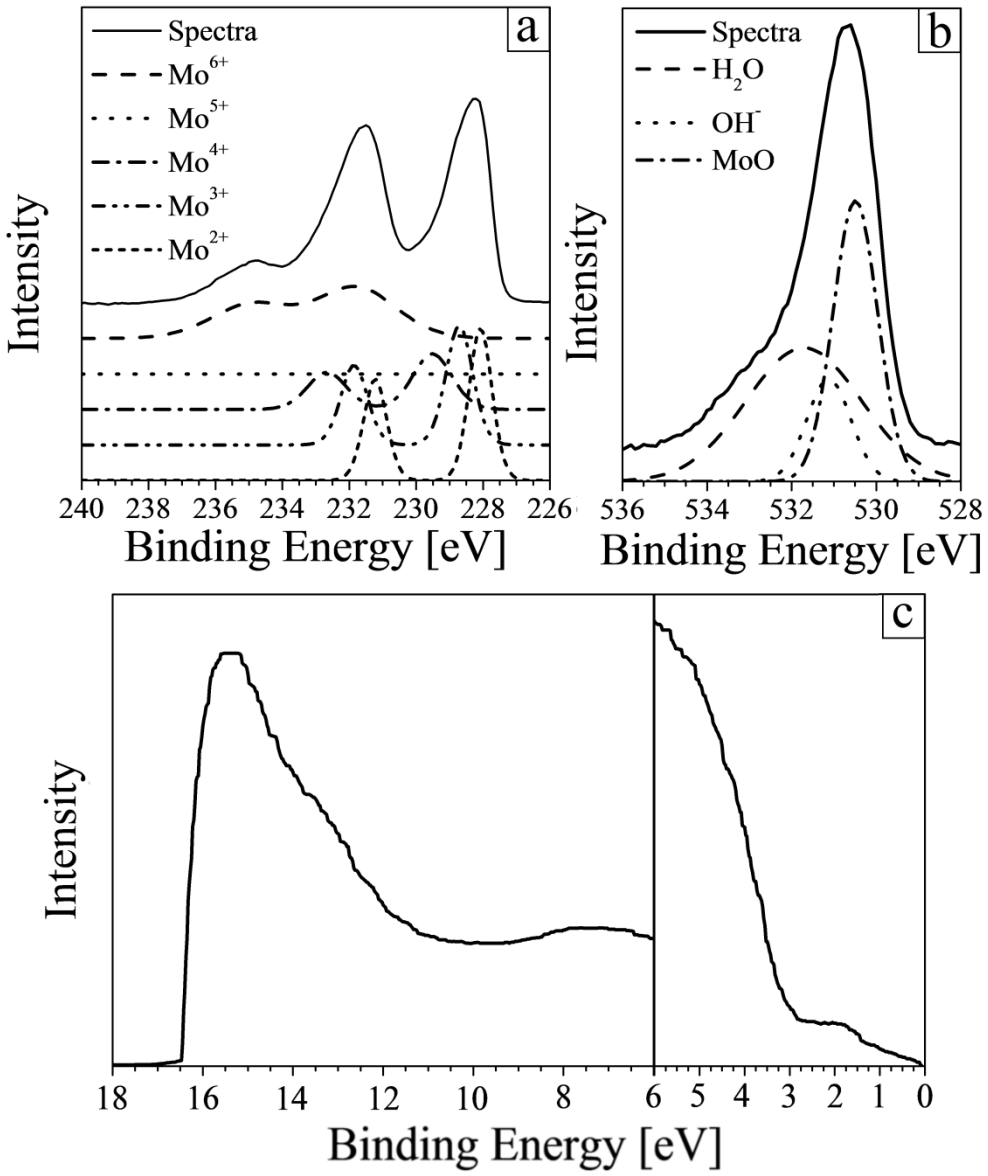

Figure 8.9 Photoelectron spectroscopy spectra for molybdenum oxide films sputtered at 5% oxygen partial pressure. X-ray photoelectron scans of the (a) Mo3d peak, (b) O1s peak, and (c) the full UPS spectra with an enhanced view of the valence band region.

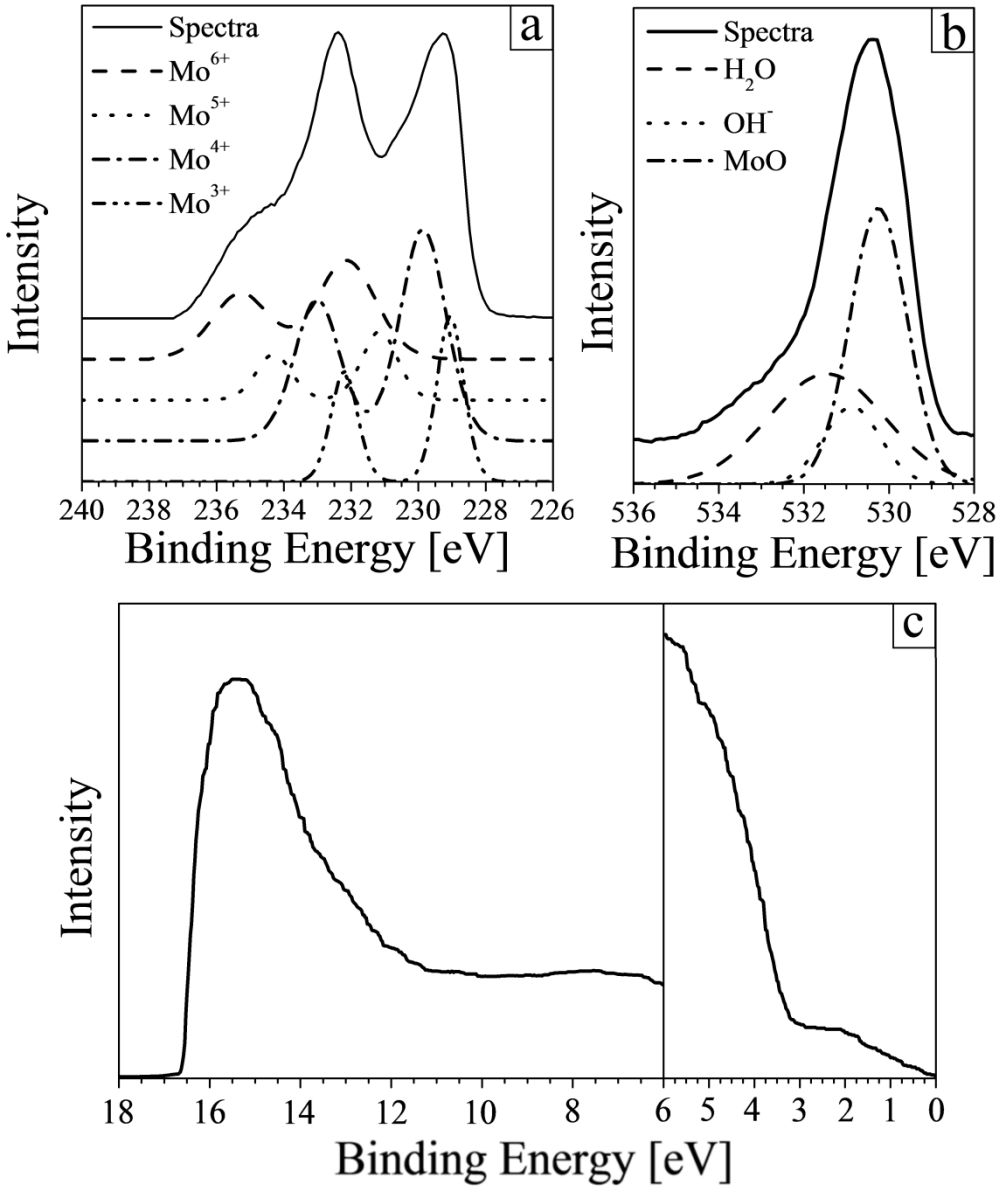

Figure 8.10 Photoelectron spectroscopy spectra for molybdenum oxide films sputtered at 10% oxygen partial pressure. X-ray photoelectron scans of the (a) Mo3d peak, (b) O1s peak, and (c) the full UPS spectra with an enhanced view of the valence band region.

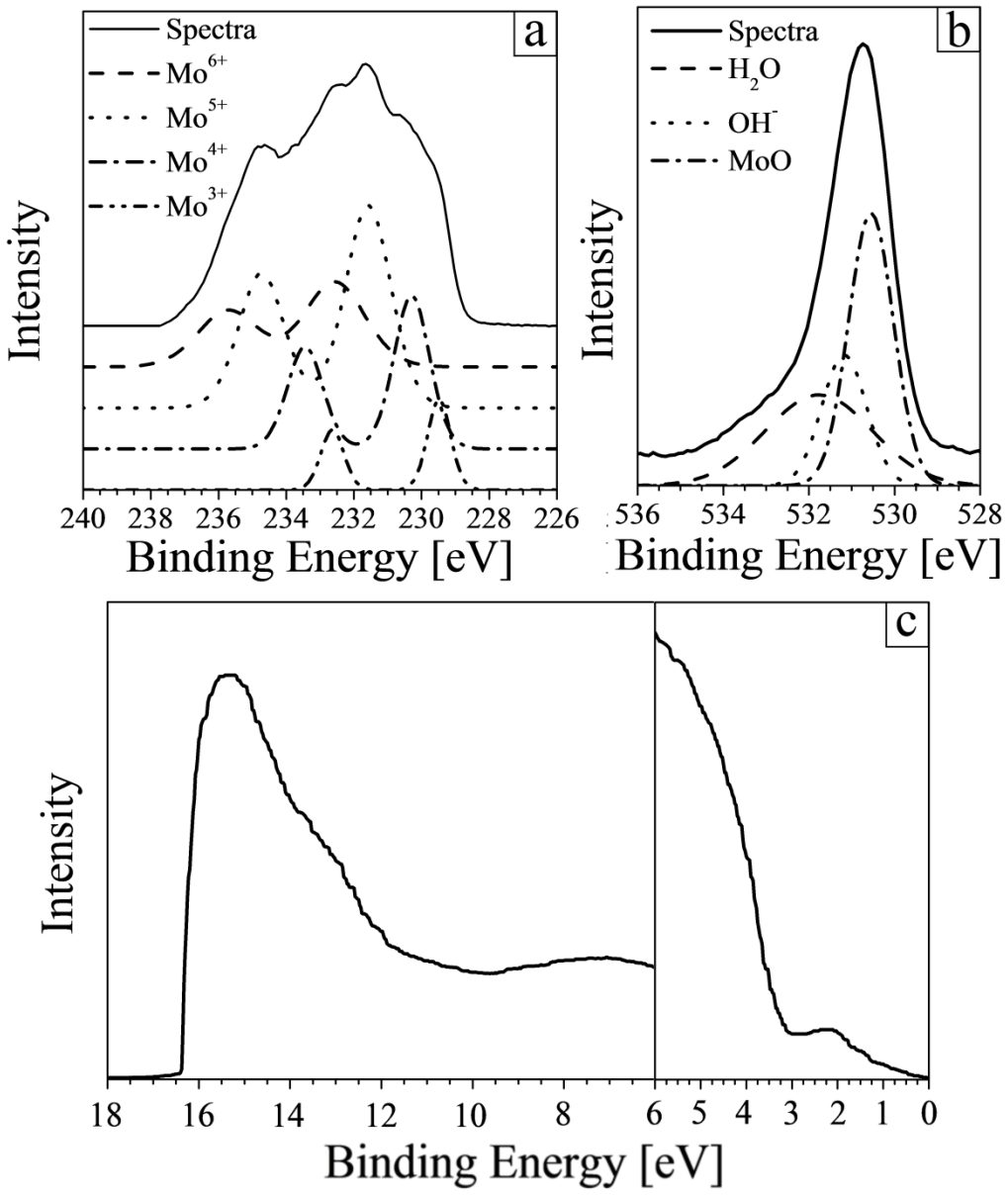

Figure 8.11 Photoelectron spectroscopy spectra for molybdenum oxide films sputtered at 15% oxygen partial pressure. X-ray photoelectron scans of the (a) Mo3d peak, (b) O1s peak, and (c) the full UPS spectra with an enhanced view of the valence band region.

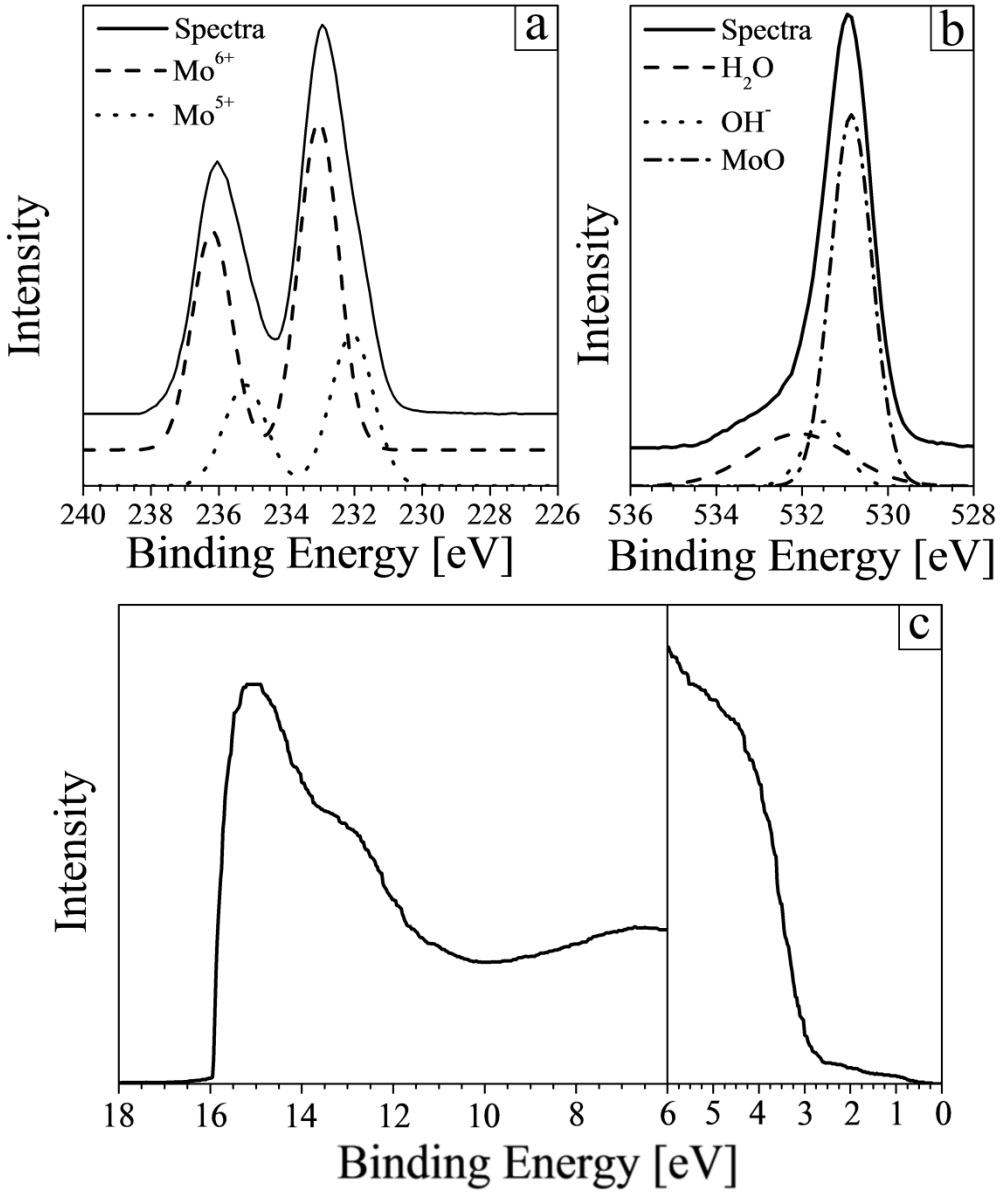

Figure 8.12 Photoelectron spectroscopy spectra for molybdenum oxide films sputtered at 20% oxygen partial pressure. X-ray photoelectron scans of the (a) Mo3d peak, (b) O1s peak, and (c) the full UPS spectra with an enhanced view of the valence band region.

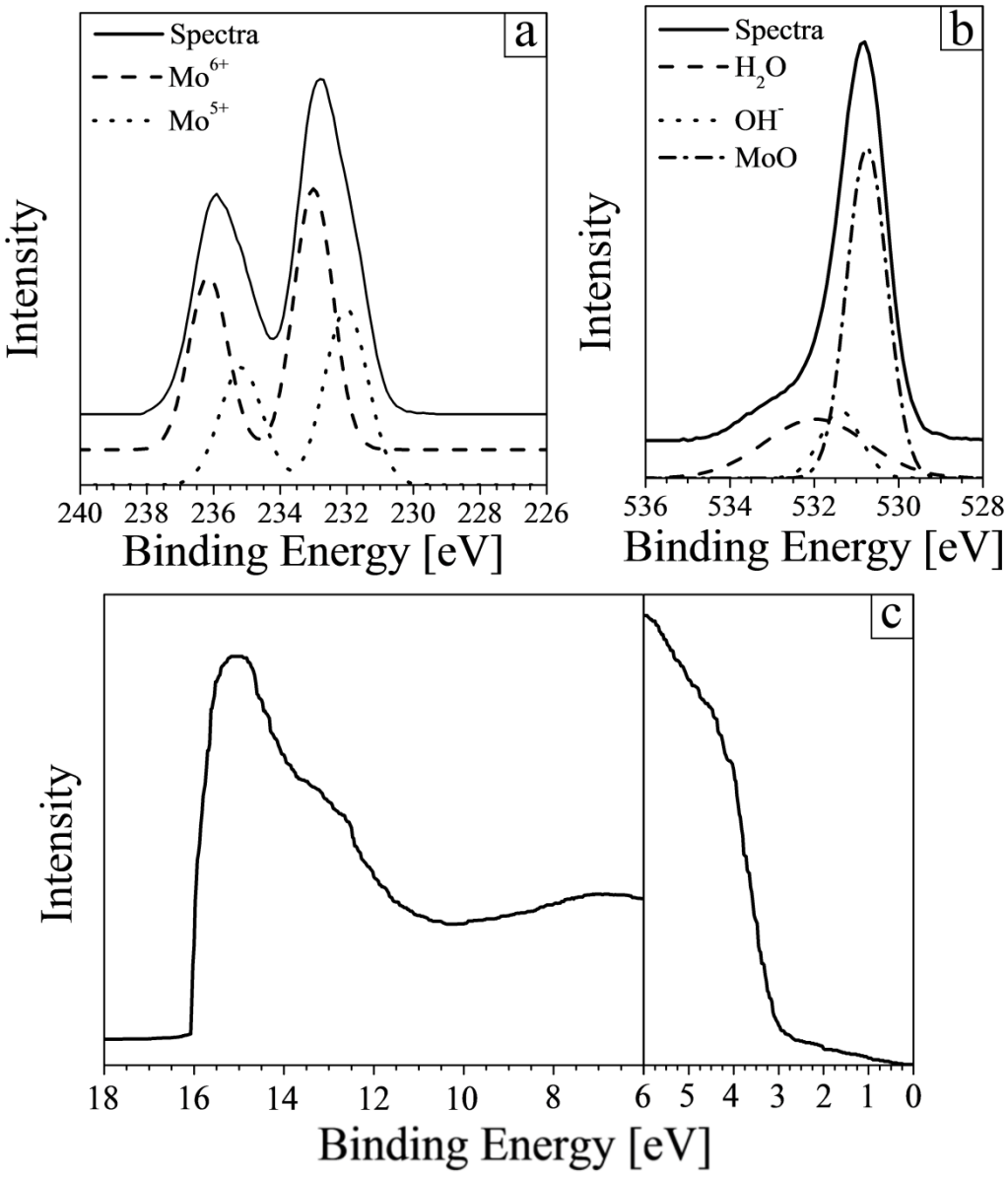

Figure 8.13 Photoelectron spectroscopy spectra for molybdenum oxide films sputtered at 25% oxygen partial pressure. X-ray photoelectron scans of the (a) Mo3d peak, (b) O1s peak, and (c) the full UPS spectra with an enhanced view of the valence band region.

	Mo 0%	Mo 5%	Mo 10%	Mo 15%	Mo 20%	Mo 25%
HO^-	530.8eV	530.8eV	530.9eV	531.2eV	531.3eV	531.6eV
MoO	530.2eV	530.2eV	530eV	530.5eV	530.8eV	530.8eV
H_2O	531.7eV	531.9eV	531.6eV	532eV	532eV	532.1eV
HO^-	1.33eV	1.40eV	1.32eV	1.29eV	1.19eV	0.99eV
MoO	1.01eV	0.98eV	1.24eV	1.21eV	1.09eV	1.15eV
H_2O	3.19eV	3.26eV	3.37eV	3.03eV	2.75eV	2.65eV
HO^-	41.9%	43.1%	29.7%	24.2%	18.4%	6.7%
MoO	17%	14.2%	33.1%	37.5%	55.7%	67.7%
H_2O	41.1%	42.7%	37.3%	38.3%	25.8%	25.6%

Table 8.3 Position, FWHM and abundances of the different chemical peaks in the high resolution O1s spectra for sputtered Molybdenum Oxide films at varying percentage pressures.

Table 8.3 shows the relative abundances, peak positions and FWHM of the different oxygen species for different sputtering conditions. The abundance of the hydroxide (OH^-) peak can be seen to vary as a function of sputtering condition, as the oxygen content within the deposited layer is increased a decrease in the hydroxide peak is seen. This is related to the presence of metallic molybdenum states allowing for the adhesion to the surface of the sample due to the formation of metal-hydroxide ionic bonds. The amount of water within the sample decreases as the oxygen content of the film increases, the adhesion of water onto metallic surfaces is due mainly to the interactions between the metallic molybdenum species and the dipole present within the water

molecule. As metallic species are reduced this interaction is decreased and less water is adsorbed onto the surface of the sample. The final species observed in the O1s spectra is the Molybdenum oxygen bond (MoO), this shows a general rise in the overall percentage as the amount of oxygen present increases, this is expected as the film becomes of a higher oxidation states more Mo-O bonds will be present within the material. It should be noted that in the C1s spectra we observe species associated with C-O and C=O bonds, these are expected to be present in the O1s spectra at a similar position to the MoO peak. The presence of these peaks are omitted from the O1s spectra due to the low intensity of the peaks in comparison to the MoO peak meaning we can assume they have negligible effect on the relative abundance of the 3 oxygen species present.

Table 8.4 Shows the relative abundances, peak positions and FWHM of the oxidation states of molybdenum oxide as observed in the Mo3d high resolution spectra. As the oxygen content within the sputtering chamber increases the oxidation state of the film increases, as is shown in the O:Mo row at the bottom of the table. In addition we see that as well as the overall oxidation state increasing the presence of the higher oxidation state species increases at the expense of lower oxidation states. It can be seen at 20% to 25% oxygen concentration that the oxidation of the film begins to become saturated as the increase in Mo^{6+} and overall oxidation is significantly reduced and that it is expected that further increase in the oxygen during sputtering will not yield high increases in the Mo^{6+} state.

	Mo 0%	Mo 5%	Mo 10%	Mo 15%	Mo 20%	Mo 25%
Mo^{6+}		-	235.3eV	235.7eV	236.0eV	235.9eV
Mo^{5+}	234.7eV	234.9eV	234.2eV	234.7eV	234.8eV	234.6eV
Mo^{4+}	-	-	233.1eV	233.4eV	-	-
Mo^{3+}	232.4eV	232.7eV	232.2eV	232.6eV	-	-
Mo^{2+}	231.6eV	231.9eV	-	-	-	-
Mo^{1+}	231.0eV	231.2eV	-	-	-	-
Mo^{6+}	-	-	2.00eV	2.21eV	1.56eV	1.66eV
Mo^{5+}	2.53eV	2.91eV	1.34eV	1.56eV	0.95eV	0.94eV
Mo^{4+}	-	-	1.40eV	1.25eV	-	-
Mo^{3+}	1.46eV	1.36eV	0.99eV	0.82eV	-	-
Mo^{2+}	1.00eV	0.95eV	-	-	-	-
Mo^{1+}	0.70eV	0.81eV	-	-	-	-
Mo^{6+}	-	-	25.4%	26.0%	89.0%	89.2%
Mo^{5+}	4.9%	9.9%	15.3%	39.8%	11%	10.8%
Mo^{4+}	-	-	35.2%	24.6%	-	-
Mo^{3+}	3.3%	4.9%	24.1%	9.6%	-	-
Mo^{2+}	4.8%	7.7%	-	-	-	-
Mo^{1+}	87%	77.6%	-	-	-	-
O:Mo	0.66	0.79	2.21	2.41	2.94	2.95

Table 8.4 Position, FWHM and abundances of the difference chemical peaks in the high resolution Mo3d spectra. Values given are for the $3d^{3/2}$ emission peak, the abundances and FWHM are the same for the $3d^{5/2}$ peak and the binding energy is 3.15eV lower.

	Mo 0%	Mo 5%	Mo 10%	Mo 15%	Mo 20%	Mo 25%
SE cut-off	16.57eV	16.46eV	16.56eV	16.37eV	15.93eV	16.06eV
Fermi Offset	0eV	0eV	0eV	0eV	0.20eV	0.24eV
Work Function	-4.65eV	-4.76eV	-4.66eV	-4.85eV	-5.49eV	-5.4eV
Valence Band	-	-	-	-	-7.88eV	-7.98eV

Table 8.5 Position of the secondary electron cut off, Fermi level offset, and the calculated positions for the work function and valence band position for sputtered Molybdenum Oxide films.

Table 8.5 shows various properties of the electronic structure of the molybdenum oxide films that can be determined via the UPS spectra. There is no linear change in the position of the work function as a function of the overall oxidation state of the deposited film. However a step change is observed between 15% and 20% oxygen content within the chamber, from the Mo3d spectra obtained for these films it can be seen that the presence of Mo^{4+} and lower oxidation states is reduced to zero. In addition a clearly defined valence band is observed for films sputtered above 15% oxygen content indicating that a shift from a metallic like film to a semiconducting/insulating film is observed.

Figure 8.14 shows the occupancy of the valence bands for Molybdenum Oxide. For purely metallic molybdenum partial occupation of the Mo5s band and full occupation of the $Mo4d_{3/2}$ band occur leading to pinning of the Fermi Level and hence the work function at just above the $Mo4d_{3/2}$ band. For films with oxidations states at Mo^{1+} to Mo^{4+} partial occupancy of the $Mo4d_{3/2}$ band will occur leading to the Fermi level being within this band. This means that further oxidation from Mo^{1+} to Mo^{4+} does not yield large changes in the work function as observed with the increase in the oxygen content during sputtering from 0% to 15%. The position of the $Mo4d_{3/2}$ state is determined by the work function of films sputtered between 0% and 15% and is estimated to be approximately -4.7eV. For films where the lowest oxidation state present is Mo^{5+} the $Mo4d_{3/2}$ band is no longer occupied and the highest occupied band is Mo5s, the Fermi level of the material then becomes pinned above the Mo5s orbital. Films sputtered at 20% and 25% have Mo^{5+} states present indicating that the Mo5s state is approximately -5.5eV. Fully stoichiometric Molybdenum (VI) Oxide has a completely empty Mo5s orbital and the highest occupied orbital is the O2p, the Fermi level will therefore be pinned at some point between the Mo5s state and the O2p state. Within devices or samples exposed to atmosphere this does not occur due to the normalization of the Fermi levels of the adsorbed or deposited layers. For these materials electron transfer occurs from the HOMO to the Mo5s eventually leading to the pinning of the Fermi level at the interface to just above the Mo5s state.

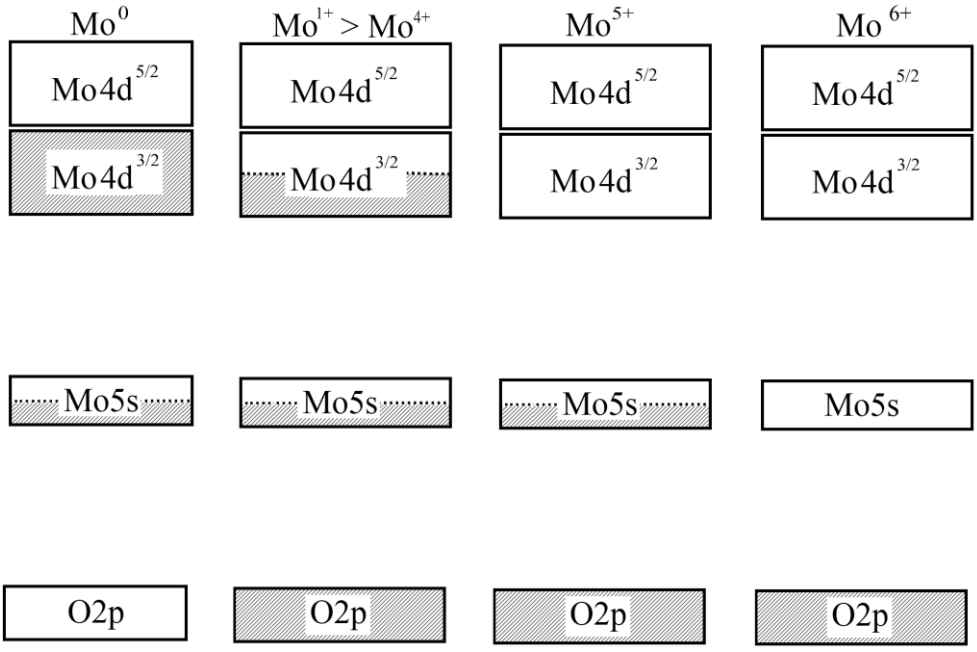

Figure 8.14 Shaded areas show the occupied electronic bands within different oxidation states of molybdenum oxide ranging from pure metallic molybdenum (Mo^0) to stoichiometric MoO_3 (Mo^{6+}).

8.6 Organic Photovoltaic Devices

Fabrication of the PCDTBT-8:$PC_{70}BM$ organic photovoltaic devices was done in tandem with the fabrication of samples prepared for AFM, Ellipsometry and XPS for sputtering conditions between 0 and 70% oxygen concentration. **Figure 8.15** shows a box plot of the Fill Factor (FF), short circuit current density (J_{sc}), power conversion efficiency (PCE) and open circuit voltage (V_{oc}) for the various devices. For devices fabricated at low oxygen concentrations (between 0% and 10%) it can be seen that there is no observable device performance. The absorption of light within the molybdenum oxide film over this region is high in comparison to films sputtered at higher oxygen partial pressure. For films sputtered at 0% the absorption of light at the peak absorption

of PCTDBT-8 is approximately 66% this drops to 22% for films sputtered at 10%. This increase in transmission does not lead to any observable increase in the performance of the organic photovoltaic device indicating that the limiting factor is not the intensity of light. The low V_{oc} shows that a non-Ohmic has contact formed between the organic layer and the molybdenum oxide layer leading to large injection barriers; this arises due to the mismatch between the work function of the Molybdenum layer of approximately -4.7eV in comparison to the HOMO of PCDTBT-8 at -5.45eV. This large interfacial barrier of 0.69eV will cause an increase in the contact resistance of a device.

As the oxygen concentration within the chamber is increased to 15% an increase in all the measured parameters is observed with the most notable increases being associated with the J_{sc} and FF of 3.82mA.cm^{-2} and 28% respectively. An increase of these two values is typically associated with a decrease in shunt current passing through the device, as the sheet resistance of the cathode increases or the number of pinholes within a device reduces the shunt current will reduce. As the molybdenum oxide on the surface of the cathode is being oxidized it is expected that the conductivity of this film should decrease. In addition the absorption of the material as calculated through ellipsometry is further reduced from 22% at 10% oxygen partial pressure to 6% at 15% oxygen partial pressure. The V_{oc} of 0.06eV for devices sputtered at this oxygen partial pressure still show that the contact between the organic layer and the metal oxide is still non-Ohmic due to the large interfacial barrier.

Upon increasing the percentage of oxygen during sputtering to 20% a further increase in performance can be seen. The most significant improvements are in the V_{oc} and PCE with them increasing by 0.86V and 2.36%. This is due to the loss of the metallic states below Mo^{5+} as can be seen in the XPS scans in **Section 8.4**; UPS scans in

Section 8.5 indicate that this loss of lower oxidation states leads to a deepening of the work function of the deposited molybdenum oxide to around -5.45eV this is the same as the HOMO of PCDTBT-8. With closely matched energy levels Ohmic contact at the interface is possible and the contact resistance within the device is greatly reduced leading to a large gain in V_{oc}. The absorption of the Molybdenum Oxide layer is reduced to 5% as calculated via ellipsometry for fully oxidized layers, this small change in the absorption between layers sputtered at 15% and 20% oxygen partial pressure does not account for the increase in the J_{sc} of 2.4mA.cm^{-2}.

At 25% the performances shows a reduction in the overall performance, except for the V_{oc}. Combinations of UPS and XPS data collected and the maintenance of the high V_{oc} indicate that energy level alignment at the interface is maintained and that any potential barriers at the interface are not the cause of this drop in performance. In addition ellipsometry data shows that the imaginary part of the refractive index does not show any significant change implying that absorption within the molybdenum oxide layer does not cause a reduction in the intensity of light that reaches the active layer. Thickness data obtained via ellipsometry also show that a trend is observed towards thinner films for higher sputtering concentrations between 20nm at 20% oxygen partial pressure and 9nm at 30% and beyond.

For devices sputtered with oxygen concentrations at 25% and higher a general trend in the increase of the FF, J_{sc} and PCE are seen up until a maximum is reached at 45% oxygen concentration where the values are 40.8%, 8.45mA.cm^{-2} and 3.16%. Afterwards a gradual reduction is observed as the percentage of oxygen during sputtering is increased to 70%, the values of the FF, J_{sc} and PCE eventually become 36.9%, 7.88mA.cm^{-2} and 2.68%. This change in the performance is not due to the

energy level alignment at the interface as indicated by the constant V_{oc} over this region and the XPS showing that no changes in the oxidation state are observed. In addition ellipsometry shows that no change in the complex refractive index occurs indicating that the transmission of light through the molybdenum oxide layer does not change with regards to the sputtering conditions. The thickness of deposited films remains constant at 9nm between 30% oxygen partial pressure and 45% oxygen partial pressure. Ellipsometric results therefore indicate that a change in the optical structure of the device due to the molybdenum oxide layers is not the cause for this change in the short circuit current, fill factor and power conversion efficiency over the range of sputtering conditions.

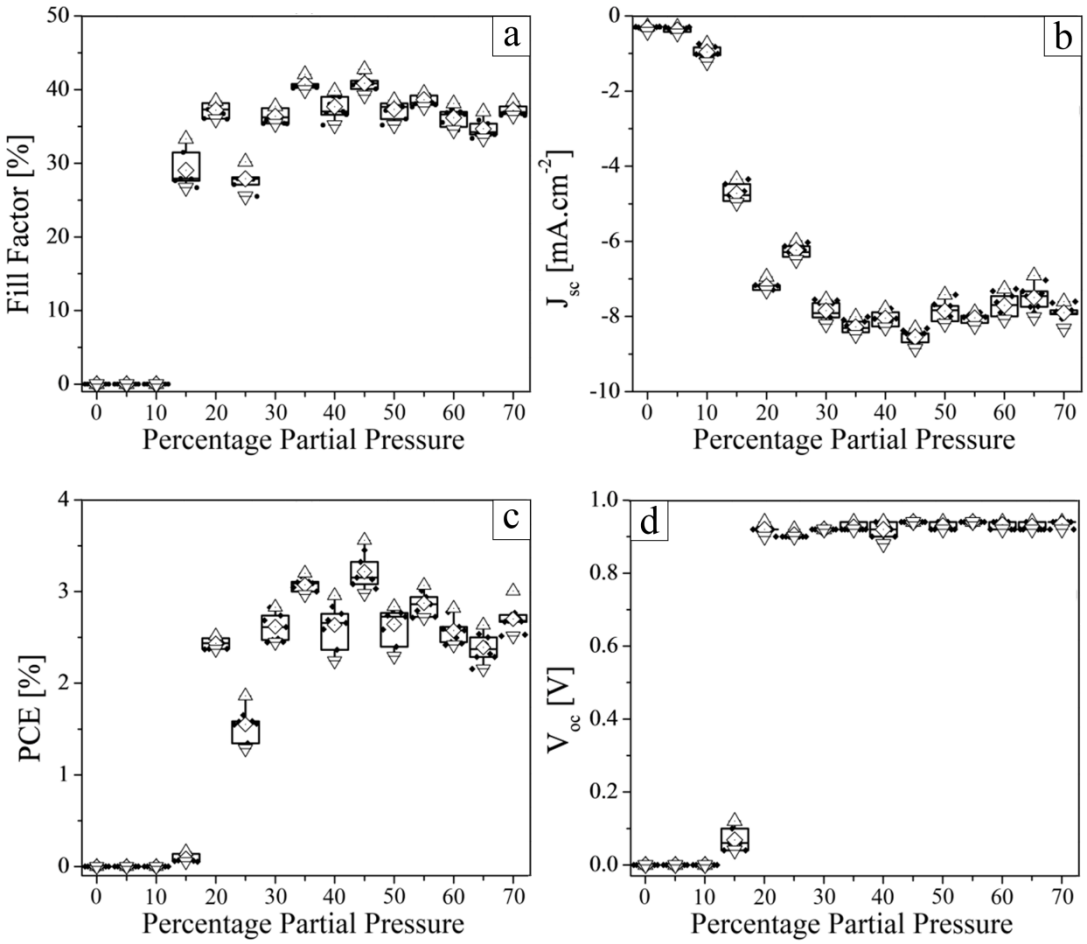

Figure 8.15 Photovoltaic device results for films sputtered between 0 and 70% oxygen. Triangles represent upper and lower quartiles, diamonds the average and circles individual data points. (a) Shows the short circuit current, (b) the fill factor, (c) power conversion efficiency and (d) the open circuit voltage.

8.7 Conclusion

Devices results in combination to measurements of the electronic, optical and physical properties of reactively sputtered molybdenum oxide films show that there are several important factors that control the performance of devices fabricated using molybdenum

oxide. The most important factor is the energy level alignment at the interface between the molybdenum oxide and the hole transporting material, by reducing the difference between the work function of the molybdenum oxide and the HOMO level of the hole transporting polymer extraction barriers are minimized and contact resistance is reduced. The work function of the molybdenum oxide layer is determined largely due to the presence of lower oxidation states these being Mo^{4+} and below. These oxidation states allow for partial occupation of the $Mo4d_{3/2}$ orbital and a pinning of the Fermi Level and the work function at shallower values of between 4.65eV and 4.75eV. In addition these oxidation states exhibit metallic behaviour due to the partial occupation of the Mo4d orbital allowing for the easy thermal excitation of charge carriers into the unoccupied orbitals. Observations in device performance show that once the lower states are removed device performance shows a marked increase even with large amounts of reduced Mo^{5+} present. In addition to the interfacial barriers caused by the presence of metallic molybdenum states large amount of absorption is observed across the visible spectra as shown via ellipsometry, this absorption reduces the amount of light transmitted to the organic layer and hence the maximum amount of excitons that can be formed.

Once the deposited films are above this oxidation threshold the work function is pinned at the Mo5s orbital and the absorption of light due to metallic states is reduced. This leads to two different properties of the deposited film that affect the performance of the device for films sputtered at higher oxygen concentration, the first of these is the surface roughness that could lead to shorts and the second is the thickness of the deposited film that will increase scattering and absorption. For higher oxygen content the deposition rate is reduced due to lower sputtering yield from Oxygen ions and also

target poisoning leading to a drop in the deposition rate. Ellipsometry results have shown that the thicknesses of sputtered films have thicknesses around 14nm ±5nm.

An additional note that can be made about the results from the devices comes from those sputtered at 20%, the presence of Mo^{5+} states within these devices are very high in comparison to films sputtered at higher oxygen concentrations and molybdenum oxide produced via vacuum evaporation. The percentage of Mo^{5+} states that are present in films sputtered at 20% is 35.9% with the remainder being Mo^{6+}. The performance of devices sputtered at 20% are close to the performance for device sputtered at higher concentrations indicating that the Mo^{5+} presence even in large quantities does not alter the electronic structure of the interface and effect charge extraction.

8.8 References

[1] A. Siokou, G. Leftheriotis, S. Papaefthimiou & P. Yianoulis. Effect of the Tungsten and Molybdenum States on the Thermal Coloration of Amorphous WO_3 and MoO_3 films. *Surface Science*. **485-485**. (2001) 2994-299

[2] L. Lozzi, L. Ottaviano, M. Passacantando, S. Santucci & C. Cantalini. The Influence of Air and Vacuum Thermal Treatment on the NO_2 Gas Sensitivity of WO_3 Thin Films Prepared by Thermal Evaporation. *Thin Solid Film*. **391** (2001) 224-228

[3] E. D. Palik. *Handbook of Optical Constants*. Boston: Academic Press (1985)

[4] M. C. Gwinner, R. D. Pietro, Y. Vaynzof, K. J. Greenberg, P. K. H. Ho, R. H. Friend & H. Sirringhaus. Doping of Organic Semiconductors Using Molybdenum Trioxide: a Quantitative Time-Dependent Electrical and Spectroscopic Study. *Advanced Functional Materials*. **21** (2011) 1432-1441

[5] E. McCafferty & J. P. Wightman. Determination of the Concentration of Surface Hydroxyl Groups on Metal Oxide Films by a Quantitative XPS Method. *Surface and Interface Analysis*. **26** (1998) 549-564

[6] T. H. Fleisch & G. J. Mains. An XPS Study of the UV Reduction and Photochromism of MoO_3 and WO_3. *Journal of Chemical Physics*. **76** (1982) 780-786

[7] J. G. Choi & L. T. Thompson. XPS Study of as Prepared and Reduced Molybdenum Oxides. *Applied Surface Science*. **93** (1996) 143-149

Chapter 9

Conclusion and Further Work

9.1 Conclusion of Work Undertaken

The use of organic semiconductors in photovoltaics opens up the ability to produce solar cells via roll-to-roll processing allowing for the production of solar cells on a large scale. With these roll-to-roll compatible printing techniques it is possible to deposit onto substrates several meters wide at speeds of several kilometres per hour allowing for the fabrication of solar cells on an unprecedented scale. However like any burgeoning photovoltaic technology there are many issues that need to be overcome before this possibility becomes reality. The biggest obstacles to the fabrication of organic based photovoltaics is the issues with low efficiencies and short lifetimes of devices in comparison to that of already developed technologies such as silicon, copper indium gallium selenide or cadmium telluride. Improvements in these key parameters have been achieved through the use of new generation semiconducting materials such as PCDTBT which have low bandgaps and deep highest occupied molecular orbitals.[1,2] These deep HOMO level materials require electrodes that have deep work functions in order to facilitate charge extraction at the interfaces. Metal oxides have been shown to allow for efficient extraction of charges from these deep HOMO polymers with performances equalling and even exceeding those achieved with PEDOT:PSS. Metal oxides in

addition have been shown to have increased stability over PEDOT:PSS, however most work regarding these materials have been focused on the use of techniques that are incompatible with the needs of organic photovoltaics, these needs being the deposition of layers via techniques compatible with roll-to-roll processing.[3,4] Throughout this work the overarching theme was the study of metal oxides within organic photovoltaic devices with the aim of trying to improve the performance of devices using these deep HOMO level polymers. In addition focus has been placed upon the processing of these metal oxides and how the solution processing of metal oxide layers using roll-to-roll compatible materials and techniques can be achieved without sacrificing performance within a device.

Initial work presented in **Chapter 5** looked at studying the basic properties of vacuum deposited metal oxides and also the organic materials that have been incorporated into devices through later chapters. Across the commonly used hole extracting metal oxides Molybdenum (VI) and Vanadium (V) Oxide there are several features that are common. These include the high transparency across the visible region of the spectrum, deep work functions and high stability. This is true for many other hole extracting metal oxides that have been studied within the literature such as Nickel (II) Oxide. When compared against the electronic structures of the organic semiconductors it was observed that all of the metal oxides should allow for the fabrication of high performance devices. Between the different hole extracting metal oxides there is little variation, all exhibit deep work functions and high optical transmission indicating that as long as a metal oxide has these two properties they should perform well.

Chapter 6 followed on from the promising results observed with vacuum deposited Vanadium (V) Oxide seen in **Chapter 5** and looked into replicating this

performance using a solution processable precursor of this metal oxide, Vanadium (V) Isopropoxide. Comparisons of optimized devices fabricated using both spin coated and vacuum evaporated Vanadium (V) Oxide show that little difference is observed in the performance of devices fabricated through this technique. Peak power conversion efficiencies of 4.9% were achieved for devices fabricated with spin coated Vanadium (V) Oxide. From results it was seen that there are several key processing requirements needed for these films to achieve optimal efficiency these include atmospheric processing where it was found that exposure to air is an important step due to the hydrolysis of the carbon oxygen bonds present within the material. In addition thickness dependence was another important factor with this dependence likely a combination of resistive losses through the layer and also the reduction in the hydrolysis of material deeper in the film due to increased diffusion lengths for water.

Chapter 7 investigated devices fabricated using a solution processable form of Molybdenum (VI) Oxide Ammonium Molybdate Tetrahydrate looking at how to process this material using ultrasonic spray coating, a roll-to-roll compatible deposition technique. Organic photovoltaic devices fabricated using this technique showed a strong dependence upon the annealing temperature of the deposited layer. Through spectroscopic studies it was hypothesised that this dependence upon temperature was due to the reduction in film thickness by the driving out of trapped residual solvent. Further device experiments confirmed this theory. This was done by reducing the concentration of the solution in order to reduce the amount of material deposited onto a substrate. Results showed that as the concentration of the solution was reduced that the performance of the device increased without the need for annealing. Maximum power conversion efficiency for unannealed devices of 4.3% was achieved, however with

further annealing a maximum efficiency of 4.8% was obtained showing that with further control of the initial solution concentration that higher performances can be achieved. Unannealed efficiencies are comparable to device sprayed onto PEDOT:PSS coated ITO and far exceed those for device spray coated onto vacuum deposited Molybdenum Oxide.

Chapter 8 finally looked at the effect of inducing reduced states in metal oxide by depositing Molybdenum Oxide of varying oxidation states via reactive sputtering. By controlling the percentage partial pressure of the oxygen within the sputtering chamber during deposition it was possible to vary the oxidation state of the Molybdenum Oxide from MoO_2 to MoO_3. Use of spectroscopic techniques showed that as the oxygen partial pressure within the chamber increased the relative abundance of different states changed. Higher oxidation states began to become more prevalent while lower oxidation states began to disappear. Two distinct types of films were observed as the oxidation state changed; the first being highly metallic films dependent upon the presence of low oxidation states of Molybdenum, the second type was a highly transparent semiconducting film that formed when only Mo^{5+} and Mo^{6+} states were present. When metallic states were present the increase in oxidation state of the film resulted in a gradual deepening of the work function from -4.65eV to -4.85eV, however upon transitioning to a semiconducting films a large shift in the work function down to -5.2eV was observed. By incorporating these sputtered layers into organic photovoltaic devices the results showed that the presence of metallic state led to poor devices due to large interfacial barriers that form between the Molybdenum Oxide and the organic semiconductor. Once these metallic states were removed devices showed increased performance due to the deepening of the work function. These results show that the

reoccupation of lower binding energy orbitals via the reduction of metal oxides can lead to large interfacial barriers. By avoiding processing steps that induce the presence of these reduced states high device performances can be achieved.

9.2 Further Work

The results obtained within this body of work show that by using correct processing steps with metal oxides it is possible to deposit films from solution via scalable techniques while maintaining high device performances. The most promising solution processable forms of metal oxides are the isopropoxides. These are readily soluble in a variety of organic solvents allowing for solutions with low surface tension and viscosity, that can be deposited at low temperatures allowing for ease of processing for high volume roll-to-roll processing.[5-8] The natural progression of this research is towards a fully solution processable device deposited onto flexible substrates via spray coating while maintain high device performances. Within the literature work has been made in the progress towards this however issues with maintaining performance have been observed.[9-13] In order to achieve a fully solution processed device while maintaining efficiencies several crucial steps are needed along the way, the first of these is to invert these devices and deposit the low temperature solution processable metal oxides onto the organic layer. The largest problem that could be foreseen would be with the solvents used in processing the metal oxide layer. Certain solvents used may not be compatible with the organic bulk heterojunction that is being deposited onto. This could be either through dewetting of the solution from the surface leading to poor uniformity of the deposited layer or a more serious consequence would be dissolving of the organic

layer itself. If this occurs the morphology of the bulk heterojunction could be altered, metal oxide particles may even diffuse into the organic layer or it may not be possible to form a complete layer on top of the organic layer. If inversion of the device is possible without the loss of performance the next step would be to deposit the underlying electron extraction layer. This process would be very similar to what has been done within this body of work with screening of suitable metal oxides, the choice of a suitable low temperature solution processable version and then the subsequent optimization of this solution processable material. Once this has been achieved the final step would be the deposition of the electrodes. Currently a large effort across many groups is being put into finding a suitable solution processable replacement for the transparent electrode (ITO) and there have been several different paths this has taken.[14] These include the use of alternative metal oxide combination such as Aluminium Zinc Oxide,[15,16] the use of thin films of graphene,[17,18] carbon nanotube arrays,[19,20] silver nanowires,[21,22] high conductivity PEDOT:PSS,[23,24] or a combination of these approaches.[25-27]

The results obtained show that metal oxides can be processed not just in vacuum but also from solution and that these solution based metal oxides produce films with electrical and optical properties identical to that of vacuum deposited films. Solution processed metal oxides have also been show to be able to be deposited using a variety of techniques without compromising the efficiency of the device. Therefore metal oxides have the ability to be used for electrodes in printed organic electronics without affecting the scalability that is often seen as the crucial advantage of organic electronics.

9.3 References

[1] C. H. Peters, I. T. Sachs-Quintana, J. P. Kastrop, S. Beaupre, M. Lecrec & M. D. McGehee. High Efficiency Polymer Solar Cells with Long Operating Lifetimes. *Advanced Energy Materials*. **1** (2011) 491-494

[2] S. H. Park, A. Roy, S. Beaupre, S. Cho, N. Coates, J. S. Moon, D. Moses, M. Leclerc, K. Lee & A. J. Heeger. Bulk Heterojunction Solar Cells With Internal Qunatum Efficiency Approaching 100%. *Nature Photonics*. **3** (2009) 297-302

[3] V. Shrotriya, G. Li, Y. Yao, C. W. Chu & Y. Yang. Transition Metal Oxides as the Buffer Layer for Polymer Photovoltaic Cells. *Applied Physics Letters*. **88** (2006) 073508

[4] Y. Sun, C. J. Takacs, S. R. Cowan, J. H. Seo, X. Gong, A. Roy & A. J. Heeger. Efficient, Air-Stable Bulk Heterojunction Polymer Solar Cells Using MoOx as the Anode Interfacial Layer. *Advanced Materials*. **23** (2011) 2226-2230

[5] T. Kuwabara, T. Nakayama, K. Uozumi, T. Yamaguchi, &. K. Takahashi. Highly durable inverted-type organic solar cell using amorphous titanium oxide as electron collection electrode inserted between ITO and organic layer. *Solar Energy Materials and Solar CellS.* **92**. (2008) 1476-1482

[6] Y. Djaoued , V. H. Phong, S. Badilescu, P. V. Ashrit, F. E. Girouard & V. V. Truong. Sol-gel-prepared films for electrochromic devices. *Thin Solid Films.* **293**. (1997) 108-112

[7] K. Zilberberg, S. Trost, J. Meyer, A. Kahn, A. Behrendt, D. Lützenkirchen-Hecht, R. Frahm & T. Riedl. Inverted Organic Solar Cells with Sol–Gel Processed High Work-Function Vanadium Oxide Hole-Extraction Layers.

Advanced Functional Materials. **21**. (2011) 4776-4783

[8] S. C. Lee, J. H. Lee, T. S. Oh & Y. H. Kim. Fabrication of tin oxide film by sol–gel method for photovoltaic solar cell system. *Solar Energy Materials and Solar Cells*. **75**. (2003) 481-487

[9] L. Yang, T. Zhang, H. Zhou, S. C. Price, B. J. Wiley & W. You. Solution-Processed Flexible Polymer Solar Cells with Silver Nanowire Electrodes. *Applied Materials and Interfaces*. **3**. (2011) 4075-4084

[10] F. C. Krebs. All solution roll-to-roll processed polymer solar cells free from indium-tin-oxide and vacuum coating steps. *Organic Electronics*. **10**. (2009) 761-768

[11] J. Wu, H. A. Becerril, Z. Bao, Z. Liu, Y. Chen & P. Peumans. Organic solar cells with solution-processed graphene transparent electrodes. *Applied Physics Letters*. **92**. (2008) 263302

[12] F. Guo , X. Zhu , K. Forberich , J. Krantz , T. Stubhan , M. Salinas , M. Halik , S. Spallek , B. Butz , E. Spiecker , T. Ameri , N. Li , P. Kubis , D. M. Guldi , G. J. Matt & C. J. Brabec. ITO-Free and Fully Solution-Processed Semitransparent Organic Solar Cells with High Fill Factors. *Advanced Energy Materials*. (2013) DOI: 10.1002/aenm.201300100

[13] J. Y. Kim, K. Lee, N. E. Coates, D. Moses, T. Q. Nguyen, M. Dante & A. J. Heeger. Efficient Tandem Polymer Solar Cells Fabricated by All-Solution Processing. *Science*. **317**. (2007) 222-225

[14] A. Kumar & C. Zhou. The Race To Replace Tin-Doped Indium Oxide: Which Material Will Win? *ACS Nano*. **4**. (2010) 11-14

[15] W. Tang & D. C. Cameron. Aluminum-doped zinc oxide transparent conductors

deposited by the sol-gel process. *Thin Solid Films.* **238**. (1994) 83-87

[16] S.B. Majumder, M. Jain, P.S. Dobal & R.S. Katiyar. Investigations on solution derived aluminium doped zinc oxide thin films. *Materials Science and Engineering: B.* **103**. (2003) 16-25

[17] K. S. Kim, Y. Zhao, H. Jang, S. Y. Lee, J. M. Kim, K. S. Kim, J. H. Ahn, P. Kim, J. Y. Choi & B. H. Hong. Large-scale pattern growth of graphene films for stretchable transparent electrodes. *Nature.* **457**. (2009) 706-710

[18] G. Eda, G. Fanchini &. M. Chhowalla. Large-area ultrathin films of reduced graphene oxide as a transparent and flexible electronic material. *Nature Nanotechnology.* **3**. (2008) 270-274

[19] L. Hu, D. S. Hecht, G. Grüner. Percolation in Transparent and Conducting Carbon Nanotube Networks. *Nano Letters.* **4**. (2004) 2513-2517

[20] Z. Wu, Z. Chen, X. Du, J. M. Logan, J. Sippel, M. Nikolou, K. Kamaras, J. R. Reynolds, D. B. Tanner, A. F. Hebard & A. G. Rinzler. Transparent, Conductive Carbon Nanotube Films. *Science.* **305**. (2004) 1273-1276

[21] J. Y. Lee, S. T. Connor, Y. Cui & P. Peumans. Solution-Processed Metal Nanowire Mesh Transparent Electrodes. *Nano Letters.* **8**. (2008) 689-692

[22] S. De, T. M. Higgins, P. E. Lyons, E. M. Doherty, P. N. Nirmalraj, W. J. Blau, J. J. Boland & J. N. Coleman. Sukanta De, "Silver Nanowire Networks as Flexible, Transparent, Conducting Films: Extremely High DC to Optical Conductivity Ratios," *ACS Nano,* vol. 3, pp. 1767-1774, 2009.

[23] S. I. Na, S. S. Kim, J. Jo & D. Y. Kim. Efficient and Flexible ITO-Free Organic Solar Cells Using Highly Conductive Polymer Anodes. *Advanced Materials.* **20**. (2008) 4061-4067

[24] Y. Galagan, J. E. J. M. Rubingh, R. Andriessen, C. C. Fan, P. W. Blom, S. C. Veenstra & J. M. Kroon. ITO-free flexible organic solar cells with printed current collecting grids. *Solar Energy Materials & Solar Cells*. **95**. (2011) 1339-1343

[25] C. H. Chung, T. B. Song, B. Bob, R. Zhu & Y. Yang. Solution-Processed Flexible Transparent Conductors Composed of Silver Nanowire Networks Embedded in Indium Tin Oxide Nanoparticle Matrices. *Nano Research*. **5**. (2012) 805-814

[26] H. S. Woo, R. Czerw, S. Webster, D. L. Carroll, J. W. Park & J. H. Lee. Organic light emitting diodes fabricated with single wall carbon nanotubes dispersed in a hole conducting buffer: the role of carbon nanotubes in a hole conducting polymer. *Synthetic Materials*. **116**. (2001) 369-372

[27] W. Hong, Y. Xu, G. Lu, C. Li & G. Shi. Transparent graphene/PEDOT–PSS composite films as counter electrodes of dye-sensitized solar cells. *Electrochemistry Communications*. **10**. (2008) 1555-1558